UNIVERSITY OF CALIFORNIA SAN DIEGO

Mesoscale Dynamics of Atmospheric Rivers

A dissertation submitted in partial satisfaction of the requirements for the degree
Doctor of Philosophy

in

Oceanography

by

Reuben Demirdjian

Committee in charge:

F. Martin Ralph, Chair
Joel Norris, Co-Chair
Amato Evan
Jan Kleissl
Richard Rotunno
Shang-Ping Xie

2020

The Dissertation of Reuben Demirdjian is approved, and it is acceptable in quality and form for publication on microfilm and electronically:

_____

_____

_____

_____

_____

Co-chair

_____

Chair

University of California San Diego

2020

DEDICATION

For my family (friends included)

EPIGRAPH

“Look again at that dot. That's here. That's home. That's us. On it everyone you love, everyone you know, everyone you ever heard of, every human being who ever was, lived out their lives. The aggregate of our joy and suffering, thousands of confident religions, ideologies, and economic doctrines, every hunter and forager, every hero and coward, every creator and destroyer of civilization, every king and peasant, every young couple in love, every mother and father, hopeful child, inventor and explorer, every teacher of morals, every corrupt politician, every "superstar," every "supreme leader," every saint and sinner in the history of our species lived there – on a mote of dust suspended in a sunbeam.”

Carl Sagan

“All things must pass.”

George Harrison

“Once there was a tree…”

Shel Silverstein

TABLE OF CONTENTS

LIST OF FIGURES

LIST OF SUPPLEMENTAL FIGURES

LIST OF TABLES

ACKNOWLEGMENTS

I would like to acknowledge Dr. Bruce Cornuelle for his continual dedication with teaching and mentoring students and his passion for precisely applying the proper methodology associated with the experiment at hand.

I would like to acknowledge Dr. Walter Monk for his unequivocal inspiration as a scientific figure and his dedication to teaching and learning. I hope to always remember his devotion to learning and teaching that he displayed during a guest lecture at the age of 99 in Dr. Larry Armi's turbulence course.

I would like to acknowledge Dr. Forrest Cannon for his unwavering support and willingness to discuss atmospheric dynamics at any time. His pursuit to include me in his studies has bolstered my understanding in the field. I would like to enthusiastically acknowledge Dr. Anna Wilson whose positive energy has lifted so many people's spirits throughout the weeks of field work marathons. I would like to acknowledge Dr. Daniel R. Cayan for his compassion and willingness to listen during some tough times while pursuing my graduate studies. I'd like to acknowledge Dr. Sasha Gershunov for his level headedness and awareness to the feelings of others around him.

The present work would not be possible without the support from so many impressive individuals at the Center of Western Weather and Water Extremes (CW3E), in particular Dr. Luca Delle Monache, Dr. Allison Michaelis, Dr. Julie Kalansky, Brian Kawzenuk, Chad Hecht, Douglas Alden, Dr. Jason Cordeira, Dr. Caroline Papadopoulos, Dr. Minghua Zheng, Dr. Andrew Martin, Dr. Scott Sellars, Dr. Rachel Weihs, and Dr. Mike DeFlorio

And finally, I am grateful to have two patient and supportive advisors Dr. Joel Norris who always welcomed long and detailed discussion on any topic I sought consultation on and finally Dr. F. Martin Ralph whose enthusiasm for science was the initial spark which ignited my pursuit in the field of atmospheric dynamics and whose mentorship allowed me to flourish.

Chapter 1, in full, is a reprint of the material as it appears in the Monthly Weather Review. Demirdjian, R., J.R. Norris, A. Martin, and F.M. Ralph, 2020: Dropsonde Observations of the Ageostrophy within the Pre-Cold-Frontal Low-Level Jet Associated with Atmospheric Rivers. *Mon. Wea. Rev.*, 148, 1389–1406, https://doi.org/10.1175/MWR-D-19-0248.1 The dissertation/thesis author was the primary investigator and author of this paper.

Chapter 2, in full, is a reprint of the material as it appears in the Journal for Atmospheric Sciences. Demirdjian, R., J.D. Doyle, C.A. Reynolds, J.R. Norris, A.C. Michaelis, and F.M. Ralph, 2020: A Case Study of the Physical Processes Associated with the Atmospheric River Initial-Condition Sensitivity from an Adjoint Model. *J. Atmos. Sci.*, 77, 691–709, https://doi.org/10.1175/JAS-D-19-0155.1 The dissertation/thesis author was the primary investigator and author of this paper.

Chapter 3, in part, has been submitted for publication of the material as it may appear in the Journal for Atmospheric Science. Demirdjian, R., R. Rotunno, B. Cornuelle, J.D. Doyle, C.A. Reynolds, 2020: The Circulation Response of a Two-Dimensional Frontogenetic Model to Optimized Moisture Perturbations . The dissertation/thesis author was the primary investigator and author of this paper.

VITA

2012	Bachelor of Science, University of California, Santa Barbara, Math and Physics
2012-2013	Bruker Nano, Atomic Force Microscopy Division
2014 - 2020	Research Assistant, University of California San Diego
2020	Doctorate of Philosophy in Oceanography, UCSD

PUBLICATIONS

Martin, A., F.M. Ralph, **R. Demirdjian**, L. DeHaan, R. Weihs, J. Helly, D. Reynolds, and S. Iacobellis, 2018: Evaluation of Atmospheric River Predictions by the WRF Model Using Aircraft and Regional Mesonet Observations of Orographic Precipitation and Its Forcing. *J. Hydrometeor.*, **19**, 1097–1113, https://doi.org/10.1175/JHM-D-17-0098.1

Reynolds, C.A., J.D. Doyle, F.M. Ralph, and **R. Demirdjian**, 2019: Adjoint Sensitivity of North Pacific Atmospheric River Forecasts. *Mon. Wea. Rev.*, **147**, 1871–1897, https://doi.org/10.1175/MWR-D-18-0347.1

Demirdjian, R., J.R. Norris, A. Martin, and F.M. Ralph, 2020: Dropsonde Observations of the Ageostrophy within the Pre-Cold-Frontal Low-Level Jet Associated with Atmospheric Rivers. *Mon. Wea. Rev.*, **148**, 1389–1406, https://doi.org/10.1175/MWR-D-19-0248.1

Demirdjian, R., J.D. Doyle, C.A. Reynolds, J.R. Norris, A.C. Michaelis, and F.M. Ralph, 2020: A Case Study of the Physical Processes Associated with the Atmospheric River Initial-Condition Sensitivity from an Adjoint Model. *J. Atmos. Sci.*, **77**, 691–709, https://doi.org/10.1175/JAS-D-19-0155.1

Cannon, F., J.M. Cordeira, C.W. Hecht, J.R. Norris, A. Michaelis, R. Demirdjian, and F.M. Ralph, 2020: GPM Satellite Radar Observations of Precipitation Mechanisms in Atmospheric Rivers. *Mon. Wea. Rev.*, **148**, 1449–1463, https://doi.org/10.1175/MWR-D-19-0278.1

Demirdjian, R., R., R. Rotunno, B. Cornuelle, C.A. Reynolds, J.D. Doyle: The Circulation Response of a Two-Dimensional Frontogenetic Model to Optimized Moisture Perturbations. *J. Atmos. Sci.*, (*in Review*)

Norris, J.R., F.M. Ralph, **R. Demirdjian**, B. Blomquist, F. Cannon, C.W. Fairall, P.J. Neiman, J.R. Spackman, S. Tanelli, D.E. Waliser: An Airborne and Surface-Based Study of the Complete Water Vapor Budget and Associated Dynamical Processes in an Atmospheric River over the Northeast Pacific. *Journal of Hydrometeorology* (*in Review*)

Cannon, F., N.S. Oakley, C.W. Hecht, A. Michaelis, J.M. Cordeira, B. Kawzenuk, R. **Demirdjian, R.**, Weihs, M.A. Fish, A.M. Wilson, and F. Martin Ralph: Observations and Predictability of a High-Impact Narrow Cold-Frontal Rainband over Southern California on 2 February 2019. *Wea. Forecasting*, (i*n Review*)

ABSTRACT OF THE DISSERTATION

Mesoscale Dynamics of Atmospheric Rivers

by

Reuben Demirdjian

Doctor of Philosophy in Oceanography

University of California, San Diego, 2020

Dr. F. Martin Ralph, Chair

Professor Joel Norris, Co-Chair

Atmospheric rivers (AR) have been found to substantially contribute to the annual precipitation in many mid-latitude regions, but while their synoptic scale dynamics have been studied for a century (through extratropical cyclone research), the mesoscale dynamics are less understood and present forecasting challenges. In this dissertation we focus on i) the pre-cold-frontal low-level jet (LLJ), ii) moisture effects on the orographic and dynamic precipitation components, and iii) physical processes associated with AR initial condition sensitivity.

An analysis using dropsonde observations from 24 cross-AR transects found that the LLJ is strongly supergeostrophic with about 20% of the wind being ageostrophic. The ERA5 reanalysis product is used to investigate the ageostrophic forcing mechanism finding that the pressure

tendency term serves to accelerate the ageostrophic jet, and the Coriolis torque and advective tendency terms serve to propagate the LLJ. Therefore, to accurately simulate an LLJ, a model must adequately resolve the pressure tendencies along the cold front.

Next, an analysis of a strong landfalling AR is presented comparing the evolution of a control simulation with an optimally perturbed simulation using the moist adjoint tool from the Coupled Ocean/Atmosphere Mesoscale Prediction System. The perturbed simulation shows a strengthened role of the orographic and dynamic components of the precipitation both resulting from enhanced latent heating effects by which: i) a stronger diabatically driven low-level potential vorticity anomaly strengthens the water vapor transport and thereby the orographic precipitation, and ii) a greater moist diabatic forcing enhances the transverse circulation thereby increasing ascent and the dynamic precipitation.

An idealized two-dimensional moist frontogenesis model is then used to quantify the transverse circulation response to varying amplitudes of optimal moisture perturbations demonstrating that small changes in moisture leads to comparatively larger changes in the frontal ascent. This non-linear growth is due to a feedback process in the transverse circulation by which small changes in moisture cause greater latent heating which ultimately lead to a strengthened transverse circulation and the cycle repeats.

The research presented in this dissertation improves the understanding of AR mesoscale dynamics through investigation of LLJs, effects of moisture perturbations, and by identifying an important feedback process.

Introduction

The forecast skill of a numerical weather prediction model depends, in part, upon the accuracy of the initialization fields. It has long been understood that small errors in the initial conditions can grow rapidly due to the chaotic nature of the atmosphere (Lorenz 1969). Since the atmosphere is generally under-sampled, one might postulate that the inclusion of any additional observations to the model initialization will lead to a gain in forecast skill (Majumdar 2016). However, not all observations made will provide equal impact to the forecast since the influence of a particular observation will depend upon the degree of activity of the region being sampled (Gray et al. 1991). The inhomogeneity of the observational impacts should thereby be leveraged to improve forecast skill such that the most critical regions of a weather system are always sampled. To accomplish this requires an understanding of the leading physical processes for the particular system under consideration. In this thesis, I investigate some of the major physical processes associated with atmospheric rivers (AR) including the pre-cold frontal low-level jet, the upper level jet/front transverse circulation, and the sensitivity of moisture to the forecast evolution. The contributions of this thesis further the community's dynamical understanding of ARs.

The predictability of ARs is vitally important for the management of water resources in California since it is a densely populated region and highly dependent on the arrival, or lack thereof, of just a handful of precipitation events per year (Dettinger 2013; Ralph et al. 2013; Dettinger and Cayan 2014; Ralph 2017; Lamjiri et al. 2017, 2018). The pre-cold-frontal low-level jet (LLJ) is a key feature associated with ARs found ahead of the cold front in an extratropical cyclone (Ralph et al. 2005, 2017; Neiman et al. 2008; Guan et al. 2015; Dettinger et al. 2011, 2013; Lavers et al. 2011; Moore et al. 2012; Rutz et al. 2014; American Meteorological Society 2017). The LLJ typically exhibits a moist neutral stratification, modest vertical wind shear, and a mean

wind speed maximum of approximately 30 m s^{-1} at 1 km elevation (Browning and Pardoe 1973; Ralph et al. 2005; Kingsmill et al. 2013). A landfalling AR with an embedded LLJ can produce copious precipitation from even modest orographic lift (~250 m), as often seen in the winter season for the West Coast of the U.S, because they are regions of large water vapor content with very little vertical displacement required for saturation (Ralph et al. 2005, 2006; Dettinger et al. 2011; Kingsmill et al. 2013; Valenzuela and Kingsmill 2015). Despite the LLJ's apparent simplicity, even early investigations determined that there was a thermal wind imbalance indicating that there is an ageostrophic component of the along-frontal flow (Orlanski and Ross 1977; Uccellini and Johnson 1979; Brill et al. 1985; Thorpe and Clough 1991; Dudhia 1993; Chen et al. 1994; Wakimoto and Murphey 2008; Winters and Martin 2014). However, there is not a clear consensus among these studies regarding the underlying dynamical cause of this ageostrophic component, which is possibly due to the small sample size investigated in each study. This thesis includes more cases of LLJs than all of the cited works combined and uses the increased sample size to characterize the LLJ ageostrophy, evaluate model representation of the ageostrophy against observations, and investigate the ageostrophic dynamics.

While it is established that model initial condition errors will grow within a forecast, the range of downstream impacts will depend upon how it projects onto the fastest growing perturbations (e.g., Reynolds et al. 2001, 2019; Doyle et al. 2014). Atmospheric instabilities are the vehicles through which small errors in the initial state may grow rapidly, thereby contributing towards forecast errors. Aircraft reconnaissance is often utilized to reduce the initial condition errors during impactful weather phenomena by collecting in-situ observations of critical regions where there may otherwise be gaps in the observing systems (Shoemaker et al. 1990; Gray et al. 1991; Martin and Gray 1993; Majumdar 2016; Ralph et al. 2020). However, the optimal sampling

locations providing the greatest improvement to the forecast are often not obvious. This obstacle is overcome through both forecaster intuition and objective tools like a moist adjoint which produces initial condition sensitivity patterns for a given response function. The latter, however, can be a black box in which distributions of sensitivities are produced without a dynamical explanation for why they were produced. This thesis focuses, in part, on improving the dynamical understanding of how perturbations identified using an adjoint technique grow rapidly and impact AR forecasts.

Chapter 1: Dropsonde Observations of the Ageostrophy within the Pre-Cold-Frontal Low-Level Jet Associated with Atmospheric Rivers

Abstract

The pre-cold-frontal low-level jet (LLJ) is an important contributor for water vapor transport within atmospheric rivers, though its dynamics are not completely understood. The present study investigates the LLJ using dropsonde observations from 24 cross-atmospheric river transects taken during the CalWater-2014, 2015 and the AR-Recon 2016, 2018 field campaigns. It is found that the LLJ, located at ~1 km elevation ahead of the cold front, has an average maximum wind speed of 30 m s^{-1} and is strongly supergeostrophic with an average ageostrophic component of 6 m s^{-1}. The along-front ageostrophy occurs within the atmospheric layer (750 – 1250 m) known to strongly control orographic precipitation associated with atmospheric rivers.

The ERA5 reanalysis product is used to both validate the observed *geostrophic* winds and investigate the supergeostrophic jet dynamics. The comparison demonstrates that there is no systematic bias in the observed geostrophic wind but that the ERA5 LLJ total wind field is generally biased low by an amount consistent with the observed ageostrophy. One of the few cases in which the ERA5 produces an ageostrophic LLJ occurs on 13 February 2016, which is used to investigate the ageostrophic forcing mechanism. This analysis demonstrates that the isallobaric (pressure tendency) term serves to accelerate the ageostrophic jet, and the Coriolis torque and advective tendency terms serve to propagate the jet normal to the LLJ. Therefore, if a model is to accurately represent the LLJ, it must adequately resolve processes contributing towards the pressure tendencies along the cold front.

1.1 Introduction

The pre-cold-frontal low-level jet (LLJ) is a key feature associated with atmospheric rivers (ARs) found ahead of the cold front in an extratropical cyclone (Ralph et al. 2005, 2017; Neiman et al. 2008; Guan et al. 2015; Dettinger et al. 2011, 2013; Lavers et al. 2011; Moore et al. 2012; Rutz et al. 2014; American Meteorological Society 2017). The LLJ typically exhibits a moist neutral stratification, modest vertical wind shear, and a mean wind speed maximum of approximately 30 m s^{-1} at 1 km elevation (Browning and Pardoe 1973; Ralph et al. 2005; Kingsmill et al. 2013). A landfalling AR with an embedded LLJ can produce copious precipitation from even modest orographic lift (~250 m), as often seen in the winter season for the West Coast of the U.S, because they are regions of large water vapor content with very little vertical displacement required for saturation (Ralph et al. 2005, 2006; Dettinger et al. 2011; Kingsmill et al. 2013; Valenzuela and Kingsmill 2015). The LLJ substantially contributes to the total moisture transport at an elevation of 750 m to 1250 m, dubbed the controlling layer (Neiman et al. 2002, 2009), which is found to be highly correlated with U.S West Coast orographic precipitation. Despite its clear relevance, Martin et al. (2018) found a low bias in the LLJs water vapor transport for both the WRF and GEFS reforecasts models compared with flight dropsondes.

The earliest investigations which recognized the ageostrophy associated with the LLJ came from analyses of the thermal wind imbalance, the difference between the thermal wind shear and the actual wind shear, across cold fronts. Orlanski and Ross (1977) performed a 2-dimensional dry idealized numerical study to investigate the degree of geostrophic balance in the cold frontal region and found an imbalance within a narrow region ahead of the cold front. They attributed the thermal wind imbalance to the circulation arising from the symmetric instability which "advects [along front] momentum and potential temperature at different rates, thereby producing a geostrophic

imbalance." Thorpe and Clough (1991) verified this in observations by performing the same calculation on dropsonde transects across several LLJs. Moreover, they found that a strong mesoscale thermal wind imbalance occurred ahead of the cold front while outside of that region conditions were largely in a state of thermal wind balance. The dynamical interpretations were limited in these two studies, however, because the former was a dry idealized 2D simulation and the latter was based on observations that are instantaneous snapshots of the circulations.

Diagnostic studies of the evolving transverse circulation associated with the upper level jet streak were later performed by Uccellini and Johnson (1979) and Brill et al. (1985). Both performed case study simulations to diagnose the low-level wind field resulting from the propagating upper level jet streak using a framework based on mass and momentum adjustment. They each found linkages between the upper level and lower level flow with the isallobaric wind driving the ageostrophy within the LLJ. Winters and Martin (2014) performed a similar but more quantitative analysis by calculating the ageostrophic transverse winds using the Sawyer-Eliassen equation and found that the contribution of the LLJ to the moisture flux had a substantial impact on the 2010 Nashville flooding event.

A similar but different framework to determine the contributing mechanisms driving the ageostrophic LLJ can be made by rearranging the expression for horizontal momentum and then solving for the ageostrophic wind tendency. The resulting three forcing terms are associated with momentum advection, Coriolis torque of the ageostrophic wind, and isallobaric component. Dudhia (1993) simulated a real event that resolved the ageostrophy of the LLJ and speculated that it resulted from the Coriolis torque on the thermally direct cross frontal flow. Chen et al. (1994) performed a diagnostic case study analysis of an LLJ using a combination of soundings and analysis data. They found that the isallobaric term dominated the momentum advection term,

though their formulation of the momentum equations did not include the Coriolis torque of the ageostrophic winds. Notably, however, they ruled out the vertical mixing of momentum as a mechanism within their LLJ. Wakimoto and Murphey (2008) utilized flight dropsonde transect observations across an LLJ combined with a scaling argument to assert that the along-frontal ageostrophy is a result of the isallobaric wind component associated with the propagation of a cyclone. The differing dynamical mechanisms accounted for in these studies indicate that there are either several different processes leading to the production of the ageostrophy in an LLJ or that some of the analyses are insufficient in some regard.

While the studies mentioned above discuss the ageostrophy of the LLJ, they all do so only for a small number of very intense cases. Consequently, the general characteristics of this feature are not well documented in the literature, such as its average contribution to the total wind strength. Moreover, it is not known whether ageostrophy is present among a variety of LLJs or only in the most intense ones. From a predictability perspective, it is important to understand the dynamical origins of the ageostrophy because it contributes a substantial fraction of the water vapor transport that is the forcing mechanism for orographic precipitation. Therefore, the accuracy of a precipitation forecast depends at least partially upon the model resolving the ageostrophic component of the transport. Furthermore, none of the existing studies evaluate a model representation of the LLJ ageostrophy against direct observations.

To address these issues, this study i) introduces a comprehensive observational approach to many more cases than have been examined in previous studies, ii) includes cases of varying LLJ intensity, iii) compares the observations to the new ERA5 reanalysis to check for systematic biases, and iv) investigates the ageostrophic dynamics in a case study. The model validation of the ageostrophy is an important step forward because it can identify any systematic biases in LLJ

wind that may be present in the reanalysis. This study is partitioned in the following way. Section 1.2 describes the data and methods, Section 1.3 discusses the observed ageostrophic component of the LLJ and its validation with the ERA5 reanalysis product, Section 1.4 presents a case study of the forcing dynamics associated with the ageostrophic component, and Section 1.5 contains the conclusions and discussion.

1.2 Data and Methods

a. Dropsondes

The primary dataset used in this study is a collection of 1239 aircraft dropsonde profiles of which 325 met our criteria from 24 flight transects through 15 different ARs obtained during intensive observing periods (IOPs) conducted in the Northeastern Pacific over a five-year period (Table 1). These IOPs and their aircraft include the NOAA G-IV for CalWater 2014-2015 and two C-130s from the U.S. Air Force 53rd Weather Reconnaissance Squadron for AR-Recon 2016 (Ralph et al. 2016, 2017; Cordeira et al. 2017), and two Air Force C-130s and the NOAA G-IV for AR-Recon 2018. The dropsondes measured wind, relative humidity, temperature, and pressure with uncertainties of 1.5 m s^{-1}, 2%, 0.2°K, and 0.4 hPa respectively (Vaisala RD94 data sheet and personal communications with Vaisala Engineer Frank DaFina). The dropsondes were released from an elevation between 8 – 10 km and each transect took about one hour, depending on the length of the transect, with an average of 7 minutes between dropsondes.

The case list of the LLJs was selected based on the following criteria: i) a low-level wind speed maximum must be present at or below 1500 m, the maximum observed height of an LLJ, ii) a cold front (identified through examination of the potential temperature transects) must be present in the transect to ensure a pre-cold frontal type LLJ, iii) each transect must have at least two

dropsondes on both sides of the LLJ center, defined by the maximum in wind speed, so that centered finite differencing can be used, iv) the latitude of the LLJ must be greater than 20°N to exclude tropical events, and v) transects occurring on the same flight day must meet a case independence criterion to prevent unequal weighting of similar transects. Criterion (v) was enforced by comparing the RMSE of wind speed from the relevant transect with respect to all other transects which met criteria (i) – (iv), and transects from the same day were determined to be independent if the RMSE of same-day transects was greater than the minimum RMSE with respect to all other transects. Informally speaking, this means that two transects taken on the same day are objectively determined to have greater differences in comparison to transects taken across completely different ARs.

Once the case list was compiled, processing of the dropsondes was done in four stages. In the first stage, NCAR's Atmospheric Sounding Processing Environment (ASPEN) software was used to quality control the data (https://www.eol.ucar.edu/content/aspen), which was done by the aircraft crew members prior to sending them out to be used by researchers. In the second stage, each dropsonde profile was regridded from its native vertical resolution (~ 20 m) to a fixed 100 m vertical grid between 0 and 8 km above mean sea level (approximately the lowest height of any of the aircraft) according to the arithmetic mean of all observations occurring within 50 m of each point in the grid. All state variables of every dropsonde profile were plotted (not shown) and visually inspected and compared to the original raw profiles to ensure that no relevant information was lost (i.e. temperature inversions, wind maxima etc.).

In the third stage, the profile within each transect containing the strongest LLJ assessed by maximum wind speed was identified and defined as the transect center, hereafter referred to as the LLJ profile. For any case with double LLJs, the stronger among the two was selected to be the LLJ

profile. The remaining dropsondes of the transects were time-to-space (T-S) adjusted following Neiman et al. (2014) with the assumption of a steady translation velocity during the measurement period. This T-S adjustment shifted the dropsonde locations to their positions at the time of the LLJ profile and caused a slight rotation in the sonde transect depending on the direction of flight (clockwise for an equatorward flight and counterclockwise for a poleward flight track).

Finally, in the fourth stage, the transects were regridded using linear interpolation along an 800 km transect centered at the LLJ profile with a spacing of 60 km (the average spacing between the dropsondes). The coordinates were then rotated to the transect normal axis (y', approximately the along-jet axis, as discussed later) and the along transect axis (x', across-jet axis). Note that the transect normal axis is very nearly along the direction of water vapor transport (Ralph et al. 2005) and approximately parallel to the cold front, which is typically oriented from the southwest to the northeast. Similarly, the transect parallel direction is approximately perpendicular to the direction of water vapor transport and is usually oriented from the northwest to the southeast.

The transect-normal geostrophic wind $\left(v_g'\right)$ was calculated using centered finite differencing and is given by,

$$v_g' = \frac{1}{f\rho}\frac{\Delta p}{\Delta x} \tag{1.1}$$

where f is the Coriolis parameter at the dropsonde latitude, ρ is the density as a function of height, Δp is the along-transect difference in pressure, Δx is the dropsonde spacing and the prime superscript indicates a coordinate rotation. The transect-normal ageostrophic wind $\left(v_{ag}'\right)$ was calculated from the residual between the transect-normal total wind and the transect-normal geostrophic wind. The measurement error of the geostrophic and ageostrophic winds was calculated by using formal error propagation techniques according to the dropsonde measurement

uncertainties given previously, and it was found to be ±1.5 m s^{-1}. The transect-parallel geostrophic wind cannot be calculated due to insufficient data in the transect-normal direction.

b. Reanalysis

The newest reanalysis product (ERA5) from the European Center for Medium Range Weather Forecasts (ECMWF) provided four uses in the present study. These were i) a synoptic scale context for the 24 cases, ii) a comparison with the observed total, geostrophic, and ageostrophic wind fields, iii) an assessment of whether the pressure tendencies over the sampling period were small enough to make the stationarity assumption, and iv) a diagnostic analysis of the ageostrophic component of the LLJ. The ERA5 product used in the present study is available at a 1-hour intervals with a resolution of 0.25 degree × 0.25 degree globally and 37 levels irregularly spaced from 1000 to 1 hPa at 25 hPa spacing or finer.

c. Gradient Wind

An estimate of the gradient wind was calculated from a combination of the observations and the ERA5 reanalysis. The gradient wind was found by first assuming no wind speed acceleration and then by solving the equation (Brill 2014),

$$\frac{V_{grad}^2}{R} + fV_{grad} + \frac{1}{\rho}\frac{\partial p}{\partial n} = 0 \tag{1.2}$$

where V_{grad} is the gradient wind, R is the radius of curvature of a parcel trajectory, ρ is the air density, and $\frac{\partial p}{\partial n}$ is the pressure gradient normal to the trajectory. Since the observations are not exactly normal to the trajectory (see Fig. 1.1 transect compared with blue lines) we cannot calculate the total gradient wind; however, we can calculate the gradient wind in the transect normal-direction by using $\frac{\partial p}{\partial x} = \frac{\partial p}{\partial n}\cos(\theta_{diff})$ and $V_{grad}^N = V_{grad}\cos(\theta_{diff})$ where $\frac{\partial p}{\partial x}$ is the along

transect pressure gradient, V_{grad}^{N} is the transect normal (N) gradient wind, and θ_{diff} is the angle difference between the transect and the trajectory. Using these relationships, the gradient wind normal to the transect is given by the equation,

$$\frac{(V_{grad}^{N})^2}{Rcos(\theta_{diff})} + fV_{grad}^{N} + \frac{1}{\rho}\frac{\partial p}{\partial x} = 0 \quad (1.3)$$

Following Brill (2014), the radius of curvature for parcel trajectories may be calculated using,

$$R = -\frac{\Delta s}{\Delta \Theta} \quad (1.4)$$

Where Δs is the parcel displacement (straight-line distance between start and end points) and $\Delta\Theta$ is the change in wind direction from initial to final time. Using ERA5, a 15 minute forward and backward trajectory centered at the LLJ dropsonde time was used to calculate R. The other quantities ($\frac{\partial p}{\partial x}$, f, and ρ) were all calculated from the dropsonde observations, and (3) was solved for the transect-normal gradient wind speed.

d. Stationarity

The stationarity assumption requires that the change in relevant quantities be sufficiently small during the sampling period such that the observations can be assumed to be taken at a single time. Since the focus of the paper is on the ageostrophic wind component, which was calculated by subtracting the geostrophic wind component, it is imperative that the pressure tendencies be sufficiently small such that the geostrophic wind calculations were nearly unchanged during the observing period. The geostrophic wind centered finite difference method required three dropsonde profiles to be used, which took a total of 14 minutes on average for collection. The change in geostrophic wind was calculated at the LLJ profile by first calculating the pressure tendency in ERA5, then dividing by the model grid spacing to obtain the geostrophic wind

tendency, and finally by multiplying it by the particular time it takes to release 3 dropsondes in each of the 24 transects. The result was an average change in the geostrophic wind of Δv_g = 0.4 m s^{-1}. Note that this is equivalent to taking the time tendency of (1) and multiplying by Δt. Since the result is much smaller than the observed ageostrophic winds (as will be shown), it follows that pressure-tendency corrections are not required since potential non-stationarity will not substantially bias the results presented here.

1.3 Observations of the Ageostrophic Component of the LLJ

a. Characterization

The 24 flight transects studied are overlaid onto their associated ARs in the thumbnail images in Fig. 1.1. Clearly, the set has substantial variety in terms of the AR strength, curvature, size, and latitude. The cases also have substantial variability in the strength of the LLJ (ranging from 21 to 41 m s^{-1}) as well as the height (ranging from 400 m to 1500 m, Table 1). Despite this variety, the cases have in common that the transects are across regions of strong water vapor transport.

The composite of the 24 transect-normal (v') and transect-parallel (u') wind fields, shown in Fig. 1.2, illustrates the characteristic environment within the AR. The vertical coordinate was normalized, prior to compositing, by dividing the true height by the LLJ height in each transect, thus creating unitless y-axes in both Figures 1.2 and 1.3. This procedure preserves the LLJ maximum, which would otherwise be smoothed out when LLJs of different heights were averaged together. However, the vertical coordinate can be approximately returned to dimensional units by multiplying the y-axes by the average LLJ height (about 1000 m). A comparison of figures with normalized height (Figs. 1.2 and 1.3) and those without (not shown) indicates that important

features such as the sharpness of the cold front are not drastically altered by the normalization process. For the purpose of display, a 5-point local smoother was applied after all calculations were performed; comparison of smoothed and unsmoothed composites indicates that smoothing does not substantially alter the composites.

There are five apparent features worth noting in Fig. 1.2: i) the intense LLJ of about 30 m s^{-1} centered at Distance = 0 km and Height = 1 and located on the warm side of the cold front, ii) the zone of a sharp equivalent potential temperature gradient seen on the cyclonic or northwest side of the LLJ marking both the cold front and moisture gradient, iii) the region of low-level cross-frontal wind convergence on the cyclonic side of the LLJ at the cold frontal boundary (Fig. 1.2b), iv) the much stronger horizontal wind shear on the cyclonic side of the LLJ relative to that on the anti-cyclonic side, and v) the bottom of the upper level jet streak above the cold front. It is important to note that features become smoothed in the composite such that they may become broader in scale and smaller in magnitude. However, the relative position of these features remains intact and the LLJ is observed immediately ahead of the cold front (Fig. 1.2a), as expected.

The composite ageostrophic wind shown in Fig. 1.3a was calculated by subtracting the transect normal wind (Fig. 1.2a) from the transect normal geostrophic wind (Fig. 1.3b) for each of the 24 transects individually, normalizing by height, and compositing using the same procedures described previously. One can readily draw four conclusions from Fig. 1.3: i) the LLJ is supergeostrophic immediately ahead of the cold front, ii) both the frontal zone and upper level jet (not shown) are subgeostrophic, the latter being expected from gradient wind balance for flow around a trough, iii) the near-surface wind is subgeostrophic, likely a result of frictional drag, though this is not substantiated in the present work, and iv) the transect-normal flow is nearly in geostrophic balance outside of the regions mentioned in (i), (ii) and (iii). The composite transect

indicates that the ageostrophic component of the LLJ (termed the AgLLJ) has a smaller transect-parallel width scale (≈100 km) than that of the AR (≈500 km). It is likely that the transect-normal length scale of the AgLLJ is similar to the length scale of the AR (on order of 1000 km) since, when combined, the transects collectively sample all areas along the AR (see Fig. 1.1). However, it cannot be ruled out that the ageostrophy occurs in most of the cases merely because each flight strategically targeted meteorologically similar regions of strong water vapor transport.

Two different statistical significance tests are applied to the AgLLJ feature. The first is a two tailed binomial distribution test using a 50% probability of success (either positive or negative ageostrophy) to determine the likelihood that the 21 of 24 cases of positive ageostrophy could have occurred by chance. The hatching in Fig. 1.3 shows the regions of statistical significance to the 99.5^{th} percentile for this test, highlighting the extreme degree of confidence that the AgLLJ does not merely result from sampling variability (more information is provided in Supplemental 1.1). The second test is a two-tail standard student-T test at the 95%-tile level which, unlike the previous test, accounts for the magnitude of the ageostrophy. It results in a pattern of statistical significance (not shown) very similar to that of the Boolean test in that both the AgLLJ and the surface subgeostrophy are found to be statistically significant regions. We do not report on field significance since the field in question (transect-normal wind speed) exhibits only two spatial degrees of freedom (Livezey and Chen 1983). This is because the wind speed at the LLJ center grid cell is highly correlated (> 0.7) to the wind speed at all other grid cells among the transects.

Figure 1.4 shows distributions of the transect-normal ageostrophic wind speed, ageostrophic percentage of the total transect-normal wind, and height above sea level of the ageostrophic wind calculated from the LLJ profiles. Since the study is focused on the positive ageostrophy of the LLJ, the averages of each distribution in the upper left corner of each plot in

Fig. 1.4 do not account for the three cases of negative ageostrophy. For the 21 positively ageostrophic cases, the average transect normal ageostrophy is 6 m s^{-1}, the percentage of ageostrophy in the total transect normal wind speed is 20%, and the height above sea level of the ageostrophy is 1 km. The distributions provide a sense of variance not incorporated in Fig. 1.3 and also demonstrate that the composite transects are characteristic of the majority of the samples.

Although the role of the LLJ in transporting water vapor within ARs has been well studied (Neiman et al. 2002, 2009; Ralph et al. 2005; Kingsmill et al. 2013; Cordeira et al. 2013; Valenzuela and Kingsmill 2015), the specific contribution of the ageostrophic wind has not. The average vertical profile of the water vapor transport in the LLJ is shown in the Fig. 1.5 (normalized in height as in Figs. 1.2, 1.3) for both the transect-normal total and geostrophic components. Above a normalized height of 2, the total and geostrophic profiles are nearly identical; but below this height they are entirely different. The discrepancies result from frictional drag, which reduces the wind near the surface, and the AgLLJ, which increases the wind centered at a normalized height of 1. The substantial difference in the two profiles demonstrates the important role of the ageostrophy in the water vapor transport.

b. Gradient Wind Imbalance

The geostrophic wind approximation is accurate for only nearly straight flow. Air parcels with highly curved trajectories will have an additional component of acceleration acting upon them known as the centrifugal force, which leads to wind directional accelerations but not wind speed accelerations. When examining wind speed accelerations, it is more appropriate to examine the gradient wind rather than the geostrophic wind because the former accounts for curvature effects. While the wind speed accelerations are of ultimate interest here, the present study focuses on the

observed ageostrophy rather than the gradient wind imbalance because the latter cannot be calculated from the dropsondes alone due to the lack of air parcel trajectory information.

Figure 1.6 shows the transect-normal gradient wind speed plotted against total wind speed for the LLJ maxima in each transect. For nearly all cases, the transect-normal total wind speed is greater than the gradient wind speed, indicating that the LLJ is not only supergeostrophic but is also supergradient. The latter is a more powerful statement than the former because it guarantees that the LLJ is undergoing wind speed accelerations while the former may not. This motivates an analysis to understand the driving mechanism behind the observed ageostrophy which is addressed in Section 1.4.

c. Comparison of Observations with ERA5 Reanalysis

Since the accuracy of the AgLLJ feature depends on the reliability of the geostrophic wind calculation, we now compare the geostrophic winds calculated from dropsondes with those calculated from the ERA5 reanalysis product to determine whether any biases exist which could create a spurious AgLLJ. The following methods were applied to the ERA5 product to ensure a fair comparison with the observational fields. First, the geostrophic and ageostrophic winds were calculated from the full ERA5 output fields using centered finite differencing. Then, for each transect, the ERA5 fields were temporally interpolated to the hour and minute of the LLJ profile dropsonde and horizontally interpolated to the T-S adjusted location of every dropsonde to form an ERA5 “dropsonde” transect. Since it is possible that the ERA5 may not place the LLJ in the same location as in the observations, we applied to the ERA5 “dropsonde” transect the same method for finding the LLJ that was applied to the observed dropsonde transect. Finally, a rotation of coordinates was performed in the same manner as for the dropsondes to yield the transect-normal geostrophic, ageostrophic, and total wind fields.

Figure 1.7a shows a scatter plot of the observed and ERA5 transect-normal geostrophic and total winds at the LLJ for each of the 24 transects. This analysis illustrates a clear low bias in the ERA5 transect normal total wind relative to the observed wind (blue squares) with a mean difference of 5.4 m s^{-1} that is statistically significant at the 95th percentile confidence level ($p < 0.05$) using a Welch's t-test. Interestingly, no bias is observed in the transect-normal geostrophic wind (red filled circles Fig. 1.7a), suggesting that the method for calculating the transect-normal geostrophic wind for the dropsondes is reliable. A low bias is also found in the ERA5 ageostrophic winds (not shown) with a mean difference of 5.0 m s^{-1} that is statistically significant at the 95th percentile confidence level also using a Welch's t-test. The fact that the total wind field is biased low by the same amount as the ageostrophic winds (5.4 versus 5.0 m s^{-1}) suggests that the ERA5 product generally does not resolve the observed AgLLJ feature.

To increase the confidence of these results, a possible methodological flaw is explored and refuted. Since the transect-normal winds were used in the previous analysis, any substantial deviation in the ERA5 wind direction from that of the observed wind will result in an incommensurate comparison. To investigate this possible bias further, the unrotated observed total wind speed is plotted against the unrotated ERA5 total wind speed at the LLJ location (Supplemental 1.2). This compares the strongest possible ERA5 winds with that of the observed winds and eliminates any possibility of a low bias due to orientation. The results (Supplemental 1.2) are similar to that of Fig. 1.7a such that the ERA5 total wind speeds are biased low by 3.1 m s^{-1} an amount less than in the rotated case suggesting that the wind direction may account for some of the significant differences observed in Fig. 1.7. This lends further support to the reliability of the methods to determine observed wind.

The preceding evidence suggests that the ERA5 total wind field is biased low because it generally does not resolve the AgLLJ. We now provide further evidence by applying the same methods used to create Fig. 1.7a to a different region that contains zero ageostrophy to determine if the ERA5 total winds are biased low in that region as they are in the LLJ region. The region selected is dubbed the "Warm" region and is located at Distance = +200 km and Height = 1 in the space of Figure 1.3a where the ageostrophic winds are zero in the observed composite. The results, shown in Fig. 1.7b, plainly illustrate that ERA5 has no statistically significant bias (having p-values > 0.1) in either the transect-normal total wind nor geostrophic wind. This supports the hypothesis that the ERA5 LLJ total wind is biased low due to the inability of ERA5 to resolve the AgLLJ feature. This conclusion is consistent with Martin et al. (2018), who found that the WRF and GEFS reforecast models tended to be "too geostrophic" as compared with dropsonde observations in exactly the same region investigated here, which resulted in a low bias in the total wind and water vapor transport. While the ERA5 almost always has a low bias in the transect-normal ageostrophic wind, there is one case that did adequately produce the AgLLJ feature, which will be explored in detail in the next section.

1.4 Diagnostic Analysis for an AgLLJ Case study

a. Evolution of the AgLLJ

The 13 February 2016 AR was a very strong event reaching a peak IVT of about 1000 kg m^{-1} s^{-1}, making it an AR CAT4 upon landfall in the Pacific Northwest, with 4 on a scale of 5 corresponding to "mostly hazardous, also beneficial" (Ralph et al. 2019). The evolution of the along-front ageostrophy is shown in Fig. 1.8 where an elongated very narrow band of ageostrophic wind is observed to intensify and decay while propagating southeastward in the span of about 15

hours. The ageostrophic wind is rotated to the transect-normal direction, approximately the along front direction (see Fig. 1.8), such that all of the red and orange colors indicate that the ageostrophic wind has at least some southerly or westerly component. At 1200 UTC 13 February, the ageostrophy is primarily cross-frontal, likely driven by the larger scale transverse circulation, with only a narrow strip of along-front ageostrophy located immediately ahead of the cold front. Over the next 6 hours the strength of the ageostrophy along this strip intensifies over an area having a length on the order of 10^3 km, a width of 10^2 km, and an ageostrophic wind magnitude ranging from 5 – 10 m s^{-1}. These characteristics are consistent with the observed ageostrophy discussed in section 1.3a . After peak intensity, the strip begins to shrink in size until all that is left is a small region on 0300 UTC 14 February.

Figure 1.9 shows an ERA5 transect taken across the region of maximum ageostrophy occurring at 1800 13 February and shown in each panel of Fig. 1.8. The transect exhibits an LLJ and its accompanying along-front ageostrophic component (i.e. the AgLLJ). This figure is plotted on height levels for consistency with the previous cross sections, which results in some missing values at the surface since ERA5 output is not available on pressure levels below the 1000 hPa level and the surface pressure for this transect is greater than 1000 hPa. From Fig. 1.9a, the along-front total wind speed maximum is observed to be about 28 m s^{-1}, centered at 1000 m, found ahead of the cold front, and above the boundary layer. The AgLLJ is found at the same location having a core width of nearly 200 km and magnitude of about 8 m s^{-1}, which agree qualitatively with the observations shown in Fig. 1.3. Although not shown, both the LLJ and AgLLJ are located within the column of maximum moisture content along the transect above a region of surface convergence and found on the warm side of a low-level potential vorticity anomaly, consistent with the hypothesis that condensational heating leads to an enhancement of the LLJ (Lackmann 2002).

These observations are all consistent with the composite analysis seen in section 1.3, although this case study provides an example of more typical gradients in the wind, temperature, and moisture content without the smoothing effect that is inherent in the composites.

b. Diagnostics of the Ageostrophic Jet's Forcing Mechanism

The frictionless horizontal momentum equations in pressure coordinates are rearranged to diagnose the forcing mechanisms of the AgLLJ in the form

$$\frac{\partial \vec{v}_{ag}}{\partial t} = -\left(f^{-1}\hat{k} \times \nabla \frac{\partial \phi}{\partial t}\right) - (\vec{v} \cdot \nabla)\vec{v} - f\hat{k} \times \vec{v}_{ag} \quad (5)$$

where $\vec{v}_{ag}$ is the ageostrophic wind vector, $\vec{v}$ is the total wind vector, ϕ is the geopotential height, and f is Coriolis parameter. Five terms from (5) are calculated and defined here. The first term on the LHS of (5) is dubbed the "Time Differenced Tendency" because it is calculated by taking finite differences in time of the ageostrophic wind field. Terms 2 – 4 are the "isallobaric tendency", "advective tendency", and "ageostrophic Coriolis torque tendency" corresponding to the three RHS terms respectively. Finally, the fifth term is the sum of the RHS of (5) and is dubbed the "Instantaneous Tendency" because it is calculated using data at one instant in time. Each of the five terms are rotated to obtain the along-front (i.e., transect-normal) components in the same manner as applied in section 1.4a. The purpose of calculating two estimates of the total tendency (time differenced and instantaneous) is for validation purposes since these two fields are expected to be identical with one another given perfect data. In practice, however, the correlation is imperfect because the time differenced tendency is an average tendency over three hours while the instantaneous tendency is at a single moment in time. The purpose of calculating the individual forcing terms is to quantify each of their contributions in the AgLLJ.

Each of the five terms calculated from ERA5 for the 950 hPa level are plotted in Fig. 1.10 for 1500 UTC 13 February while the AgLLJ wind speeds are intensifying. Comparison of the time differenced tendency pattern with the instantaneous tendency pattern shows a qualitatively similar picture with both patterns exhibiting a dipole of positive/negative accelerations on at the dropsonde transect location (Fig. 1.10a, b). The differences in the magnitude between the time difference and instantaneous tendencies exist primarily because they are incommensurate in time but also because friction is neglected in the latter term. Despite the difference in magnitudes, the qualitative agreement between the two terms agree provides confidence in the forcing components.

Next, the forcing components are examined individually in Figure 1.10c-e. The isallobaric term (Fig. 1.10c) is concentrated along the front and dominated by the strong positive acceleration greater than 1.0 10^{-3} m s^{-2}. If sustained over only one hour, the positive acceleration would produce an ageostrophic wind speed of 3.6 m s^{-1}, which is consistent with the observed ageostrophic wind speeds from section 1.3a. The advection tendency term (Fig. 1.10d) exhibits a strong negative tendency along the front on the order of -1.0 10^{-3} m s^{-2} with a positive tendency strip to the southwest of the transect. It additionally has a much weaker but broader region of negative acceleration extending far out into the warm region. Lastly, the ageostrophic Coriolis torque tendency term (Fig. 1.10e) has a very broad positive acceleration extending over the warm region up to the cold front, with some weaker negative acceleration in the cold region.

A qualitatively similar picture is seen in the cross sections (dotted line in Figs. 1.8, 1.10) of the forcing terms shown in Fig. 1.11. For context, the along front ageostrophic winds are overlaid on the cross sections (black contours) and are located immediately ahead of the cold front with a magnitude above 8 m s^{-1} that decays rapidly with height. As in the plan-view, there is good agreement between the patterns of time differenced and instantaneous tendencies despite the

difference in magnitude. Additionally, the isallobaric and the AgLLJ maxima are collocated with one another indicating that the AgLLJ is being accelerated by the isallobaric term at this time. In contrast, both the minimum advective tendency and the maximum ageostrophic Coriolis torque terms are offset from the AgLLJ maximum indicating that both these terms are propagating the AgLLJ at this time.

The evolution of both the AgLLJ and the momentum budget are shown in Fig. 1.12 starting from 0600 13 February and ending on 0600 14 February across the transect shown in the Fig. 1.8. Initially, at 0600 13 February (Figs. 1.12a-d) there is a clear tri-pole in the instantaneous tendency dominated by the isallobaric and Coriolis terms with only small ageostrophic wind values. By 1200 13 February (Figs. 1.12e-h), the positive isallobaric generates the clear AgLLJ in the center of the domain with some contribution from the Coriolis torque. At 1800 13 February (Figs. 1.12i-l), the continued overlap of the isallobaric tendency with the AgLLJ maximum serves to further intensity the AgLLJ locally reaching a maximum of about 8 m s^{-1}. During this same time, the negative advective tendency on the northwest (left) side and the positive Coriolis torque on the southeast (right) side of the AgLLJ maximum propagate the jet towards the southeast. By 0000 14 February (Figs. 1.12m-p) the isallobaric tendency continues to intensify and large values of ageostrophy are generated with a substantial contribution from the advective term. Finally, by 0600 14 February (Figs. 1.12q-t) negative tendencies in the advection tendency deteriorate the remaining ageostrophy.

The momentum budget analysis demonstrates that the isallobaric term is the most concentrated and has the best overlap with the AgLLJ maximum, though there are certainly some contributions from the advective and Coriolis terms. At low levels ahead of the cold front, the ageostrophic Coriolis torque is broad, weak, and located ahead of the AgLLJ maximum which

serves to propagate rather than intensify the jet. Similarly, the advective term is generally negative behind the AgLLJ maximum also serving to propagate the jet. For this case, the observed AgLLJ is found to be driven primarily by the isallobaric tendency and is propagated by the Coriolis torque and advection tendencies.

1.5 Conclusions and Discussion

This study employed a large number of aircraft dropsonde observations sampled across Atmospheric Rivers (AR) to investigate the ageostrophic component of the wind in the transect-normal (i.e., along frontal) direction. It was found that 21 of 24 cases have a positive component of ageostrophic wind with an average magnitude of 6 m s^{-1} ± 1.5 m s^{-1}, which contributes about 20% of the total wind at the LLJ maximum located at approximately 1 km elevation. The ageostrophic component of the LLJ, referred to as the AgLLJ, is found immediately ahead of the cold front and above a region of low-level convergence. The question of whether the AgLLJ is an artifact resulting from the neglect of curvature effects in the geostrophic approximation was investigated by calculating the gradient wind, and it was demonstrated that the total wind is greater than the gradient wind in the majority of cases. This indicates that the AgLLJ is also a region of supergradient wind, thus implying that the ageostrophy results from acceleration of wind speed rather than merely directional acceleration associated with gradient wind balance.

The ERA5 reanalysis product was employed to diagnose the forcing dynamics of the AgLLJ. For the majority of the cases investigated here, the ERA5 does not adequately resolve the AgLLJ, likely due to the jet's narrow width being on the order of 10^2 km. A one-to-one comparison of the ERA5 and observed geostrophic and total winds demonstrated that the ERA5 has a low bias for the total wind but not the geostrophic wind. One case in which the ERA5 qualitatively

reproduces the observed AgLLJ occurs on 13 February 2016. An idealization of the dynamical processes for this case is shown in the Fig. 1.13 schematic on a 900 hPa plan-view surface during the time of maximum AgLLJ intensity. In this schematic, the isallobaric term is co-located with the AgLLJ maximum serving to accelerate the jet. The Coriolis torque term, however, is positive ahead of the jet serving more to propagate the jet along rather than to accelerate it. Lastly, the advection tendency term is found to be negative behind the jet also serving to propagate it toward the southeast.

The positive contribution from the isallobaric tendency term implies that the frontal dynamical processes generating pressure tendencies at low levels lead to a positive along-frontal ageostrophic wind. This validates the scaling argument from Wakimoto and Murphey (2008) and is consistent with the diagnostic analyses of Uccellini and Johnson (1979), Brill (1985), and Chen et al. (1994). An example of one such process is latent heating above the AgLLJ that may contribute towards pressure falls thereby accelerating the ageostrophic winds. Lackmann (2002) described a related process by which the low-level latent heating generates a diabatically driven PV anomaly to which the horizontal circulation responds by developing a southerly/northerly component on the anti-cyclonic/cyclonic side of the PV. By performing a PV inversion analysis, Lackmann was able to quantify the height (pressure) falls associated with the diabatic PV anomaly. Both the isallobaric mechanism from this study and the response to the diabatic PV anomaly from Lackmann (2002) describe a response of the wind due to pressure (height) falls. It thereby seems plausible that they both describe the same response viewed from different frameworks.

The ageostrophic enhancement of the vertical profile of water vapor transport within the LLJ is furthermore illustrated in the Fig. 1.13 schematic that is based on observed differences between total and geostrophic water vapor transport. Much of the ageostrophic enhancement

occurs between 750 – 1250 m, the layer which is known to correlate highly with orographic precipitation (Neiman et al. 2002, 2009). This means that the ageostrophic component adds vapor transport where it is most able to enhance orographic precipitation for the U.S West Coast during the wet season (Fall – Spring). Furthermore, without this enhancement the geostrophic component lacks the sharp maximum in the vapor transport profile located at 750 m. Contrastingly, the ageostrophic component actually serves to reduce the vapor transport at the surface, likely due to friction. Outside of the LLJ region, the wind is expected to be either mostly geostrophic or governed by transverse circulation dynamics. However, inside this region the ageostrophy provides a substantial contribution towards the water vapor transport consistent with Winters and Martin (2014), who found that a large contribution of the vapor transport was associated with the ageostrophy.

Acknowledgements

This project was supported by California's Department of Water Resources.

Chapter 1, in full, is a reprint of the material as it appears in the Monthly Weather Review. Demirdjian, R., J.R. Norris, A. Martin, and F.M. Ralph, 2020: Dropsonde Observations of the Ageostrophy within the Pre-Cold-Frontal Low-Level Jet Associated with Atmospheric Rivers. *Mon. Wea. Rev.*, 148, 1389–1406, https://doi.org/10.1175/MWR-D-19-0248.1 The dissertation/thesis author was the primary investigator and author of this paper.

Tables and Figures

Table 1.1: The aircrafts used, dates, times and locations of 24 dropsonde cases as well as some results unique to this study. The full names of the G-IV and C-130 aircrafts are the Gulfstream G-IV SP, N49RF and the ARFC C-130J.

Transect [yyyymmddT#]	Aircraft	First Sonde [hh:mm]	Last Sonde [hh:mm]	No. Of Sondes	Height of LLJ [m]	LLJ Wind Speed [m s^{-1}]	Max AgLLJ [m s^{-1}]	MAX IVT [kg m^{-1} s^{-1}]	Vag/Wspd
20140208T1	G-IV	20:50	21:46	9	400	23	8	638	0.35
20140208T2	G-IV	22:43	23:38	9	800	27	5	946	0.19
20140211T1	G-IV	19:03	21:03	14	1200	44	9	1171	0.2
20140211T2	G-IV	20:33	21:24	12	1500	42	4	1041	0.1
20140213T1	G-IV	18:51	20:22	16	1500	30	2	733	0.07
20150115T1	G-IV	21:14	22:46	12	700	31	8	656	0.26
20150117T1	G-IV	22:45	0:30	10	500	32	12	749	0.38
20150206T3	G-IV	21:59	22:59	8	1000	31	9	886	0.29
20150208T2	G-IV	13:12	14:48	13	1000	27	-2	871	-0.07
20150214T1	G-IV	18:03	19:28	13	1000	30	1	1048	0.03
20160213T1	C-130	20:41	23:41	20	400	29	6	662	0.21
20160213T2	C-130	23:41	1:58	23	1500	37	4	848	0.11
20160213T3	C-130	20:33	23:21	25	500	33	9	655	0.27
20160215T1	C-130	20:47	23:01	16	900	29	5	516	0.17
20160215T2	C-130	23:01	2:02	20	1200	32	6	229	0.19
20160221T2	C-130	20:33	0:00	23	1500	41	-5	714	-0.12
20180126T2	C-130	0:15	1:46	8	700	27	2	580	0.07
20180126T3	C-130	20:44	22:22	10	400	24	12	439	0.5
20180128T1	C-130	20:31	21:34	6	600	33	6	870	0.18
20180128T2	C-130	21:34	23:04	7	1100	33	7	731	0.21
20180128T4	C-130	0:36	1:36	6	600	21	5	547	0.24
20180131T3	C-130	20:31	23:02	16	1400	33	-11	696	-0.33
20180202T3	C-130	20:34	23:57	17	400	28	7	675	0.25
20180202T5	G-IV	20:58	22:18	12	800	40	8	888	0.2

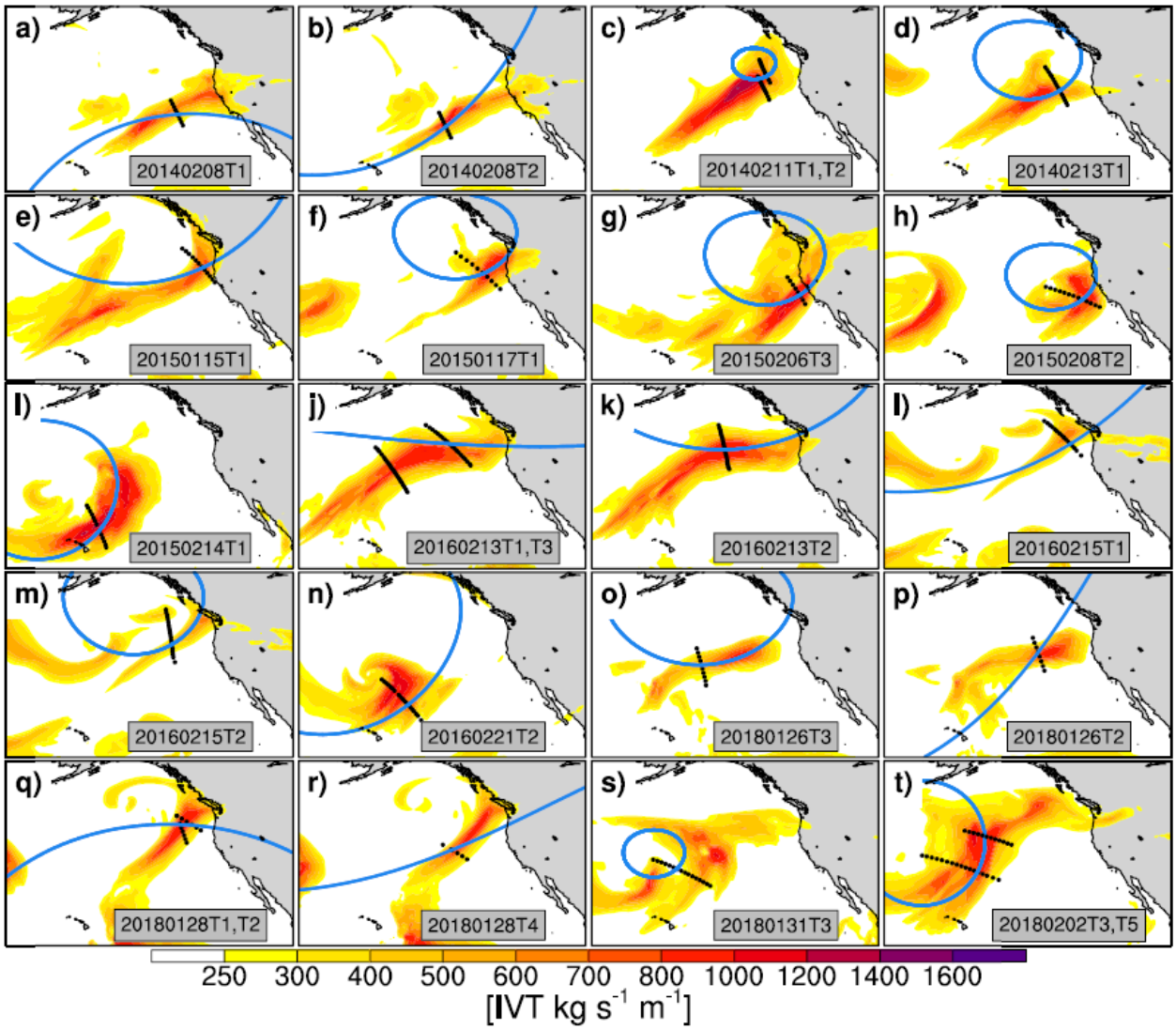

Figure 1.1: Northeast Pacific plan-view images of IVT (color fill; kg s^{-1} m^{-1}) from the ERA5 reanalysis product for each of the individual LLJ/AR cases. Black dots represent dropsonde locations and the blue curves show the radii of curvature for each LLJ trajectory. The flight transects are matched to the ERA5 plan-view at the nearest 3 hour interval. The bottom right text is the case identifier in the form yyyymmddT# where T# represents the transect number; cases with multiple transects on the same day have "T#" separated by commas.

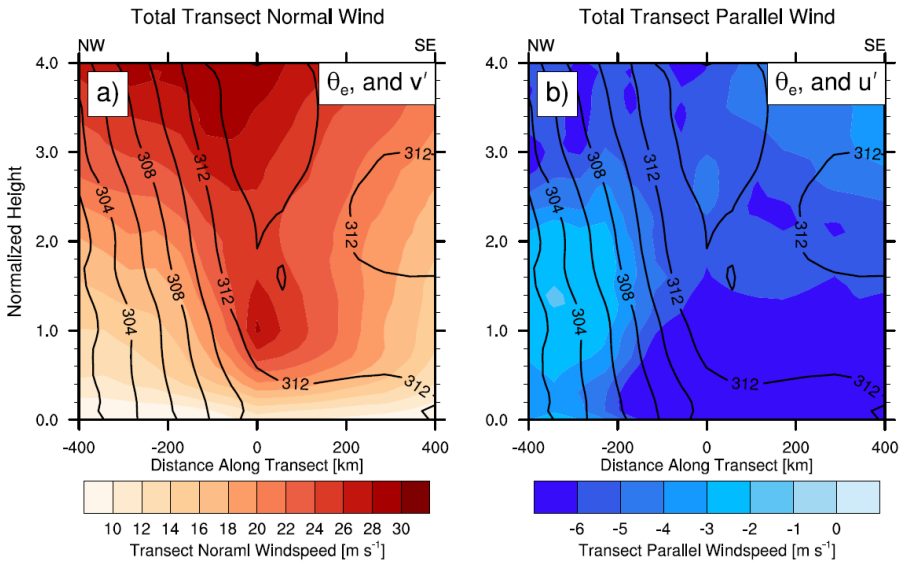

Figure 1.2: Transect composites, normalized vertically by LLJ height, for a) transect-normal (into the page) wind speed (color fill; m s^{-1}) and b) transect-parallel (across the page) wind speed (color fill; m s^{-1}), with both plots having equivalent potential temperature (solid black; K).

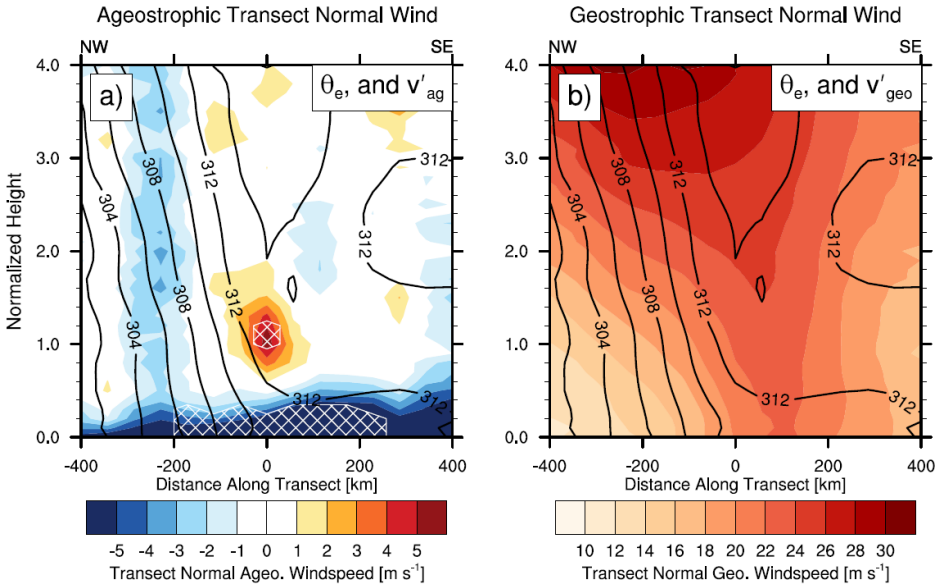

Figure 1.3: Transect composites, normalized vertically by LLJ height, for the transect-normal a) ageostrophic wind (color fill; m s^{-1}) and b) geostrophic wind (color fill; m s^{-1}), with both plots having equivalent potential temperature (solid black; K). Hatching in (a) represents the 99.5th percentile of significance according to a binomial test (see text for details).

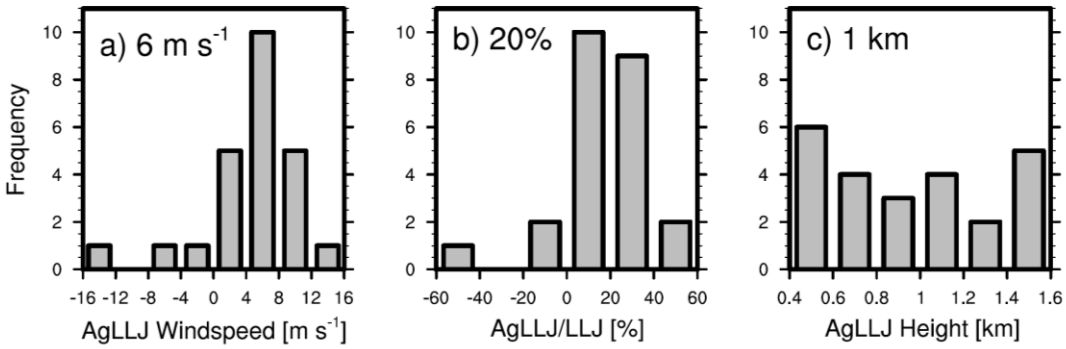

Figure 1.4: Histograms of the a) maximum AgLLJ wind speed (m s^{-1}), b) fractional contribution of AgLLJ wind to the total wind (unitless), and c) height of the AgLLJ (km). The numbers at the top left of each plot are the averages of each quantity for the 21 of 24 positively ageostrophic cases.

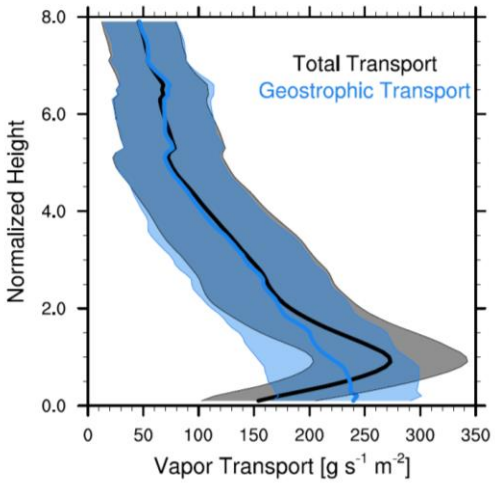

Figure 1.5: Transect-normal water vapor transport as a function of height for the total (black; g s^{-1} m^{-2}) and the geostrophic (blue; g s^{-1} m^{-2}) with the averages in bold and one standard deviation shown in color fill. The vertical profiles are taken at the LLJ location. A running vertical mean of 3 points is applied to both curves with only superficial differences compared to the original profiles.

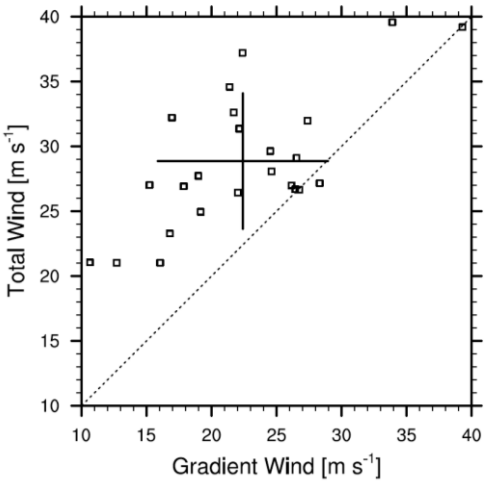

Figure 1.6: The observed transect-normal total winds (m s^{-1}) versus the transect-normal gradient wind for each of the 24 transects. The cross shows the mean at the center and the 1-sigma standard deviations given by the lengths of each of its axes.

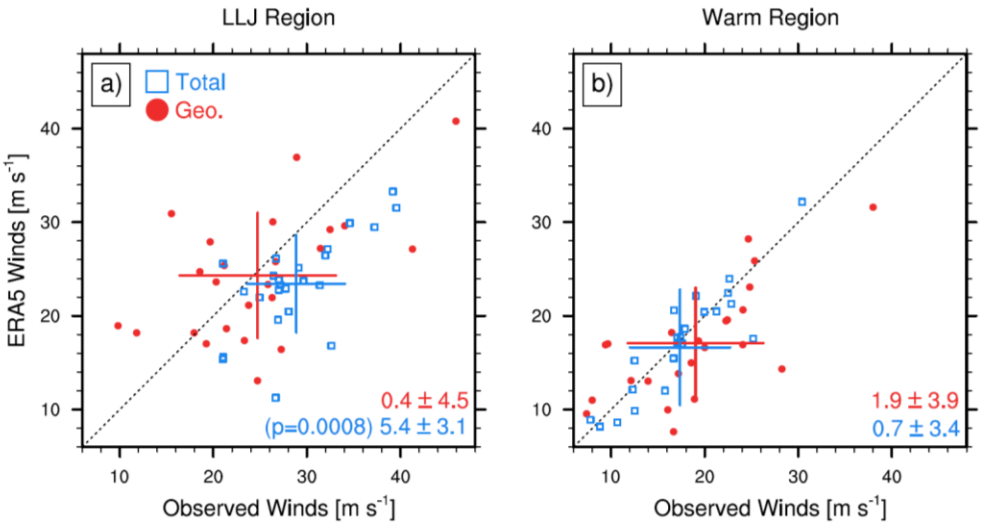

Figure 1.7: a) ERA5 versus the observed transect-normal total wind speed (blue empty squares; m s^{-1}) and transect-normal geostrophic wind speed (red filled circles; m s^{-1}) at the LLJ location, b) same as (a) except for the Warm region as mentioned in the text. The crosses are centered at the mean values with lengths of one standard deviation. The numbers on bottom right are the difference in the means with a confidence interval at the 95%-tile using a two-tail t-test distribution, and the p-values for a Welch's t-test in the parentheses.

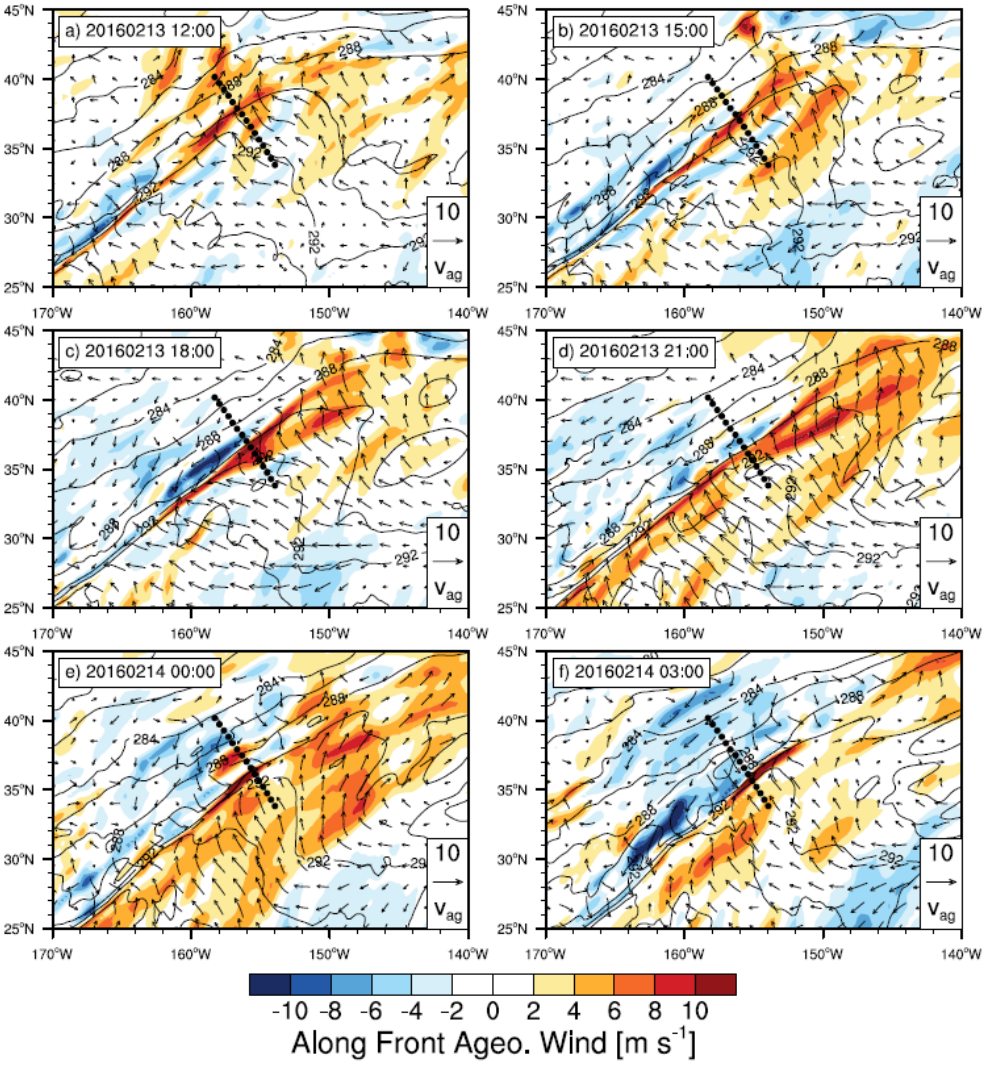

Figure 1.8: A 950 hPa time sequence from 18:00 UTC on the 13th to 09:00 UTC on 14 February 2016 of the potential temperature (solid black; K), along-front ageostrophic winds (color fill; m s^{-1}), and ageostrophic wind vectors (m s^{-1}).

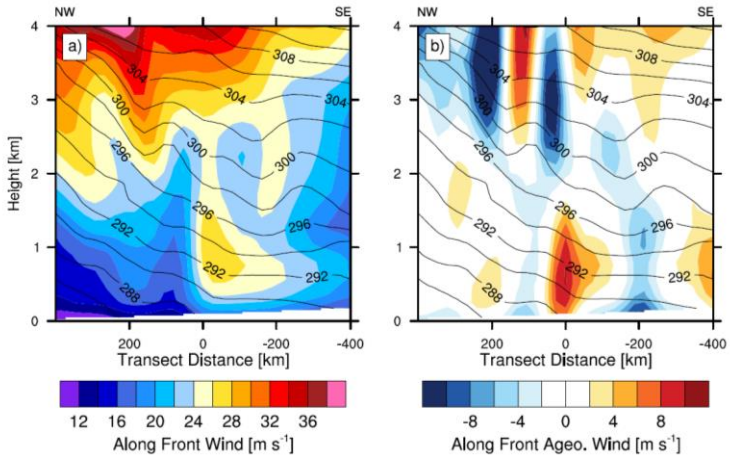

Figure 1.9: ERA5 for the transect shown in Fig. 1.8 of the potential temperature (solid black; K) and a) transect-normal total wind speed (color fill; m s^{-1}), and b) transect-normal ageostrophic wind speed (color fill; m s^{-1}). The NW and SE labels at the top represent the Northwest and Southeast ends of the transect (as shown in Fig. 1.8).

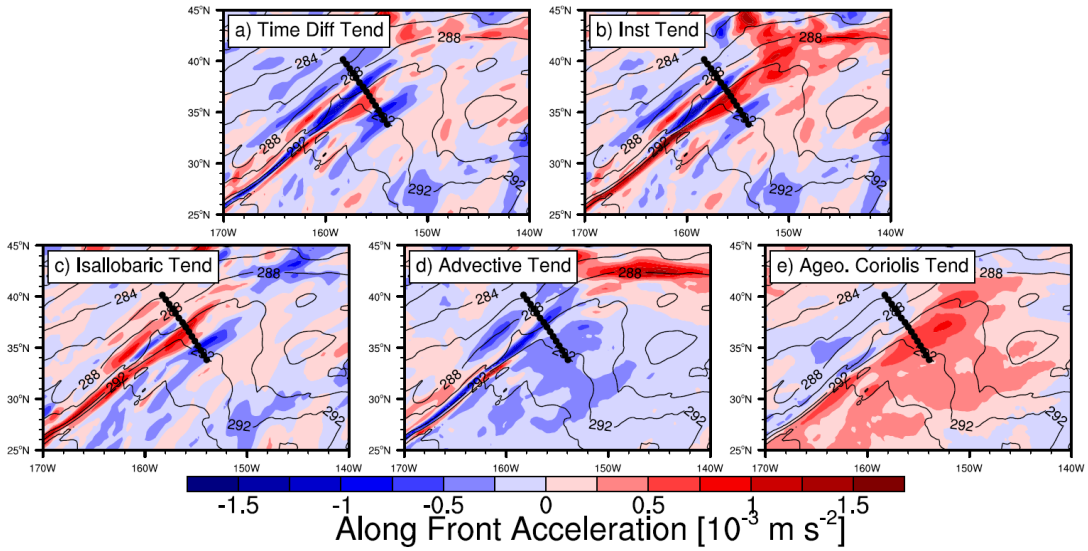

Figure 1.10: 950 hPa plan-view maps at 13 February 1500 of the transect-normal ageostrophic accelerations contributing to a) the finite-differenced ageostrophic wind tendency, b) the instantaneous ageostrophic wind tendency, c) the isallobaric tendency, d) advection tendency, and e) ageostrophic Coriolis tendency (color fill; m s^{-2}). The potential temperature is shown in solid black every 2 K.

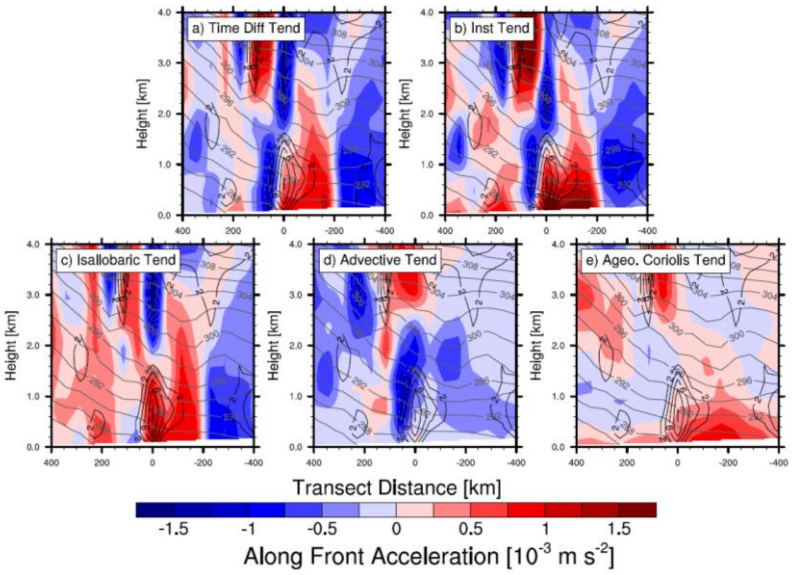

Figure 1.11: As in Fig. 1.10 expect with terms calculated along the transects shown in Figs. 1.8 and 1.10. The solid black contours are the transect normal ageostrophic winds every 2 m s^{-1} and the solid gray contours are the potential temperatures every 2 K. The left side of each plot is on the Northwest side of the transect.

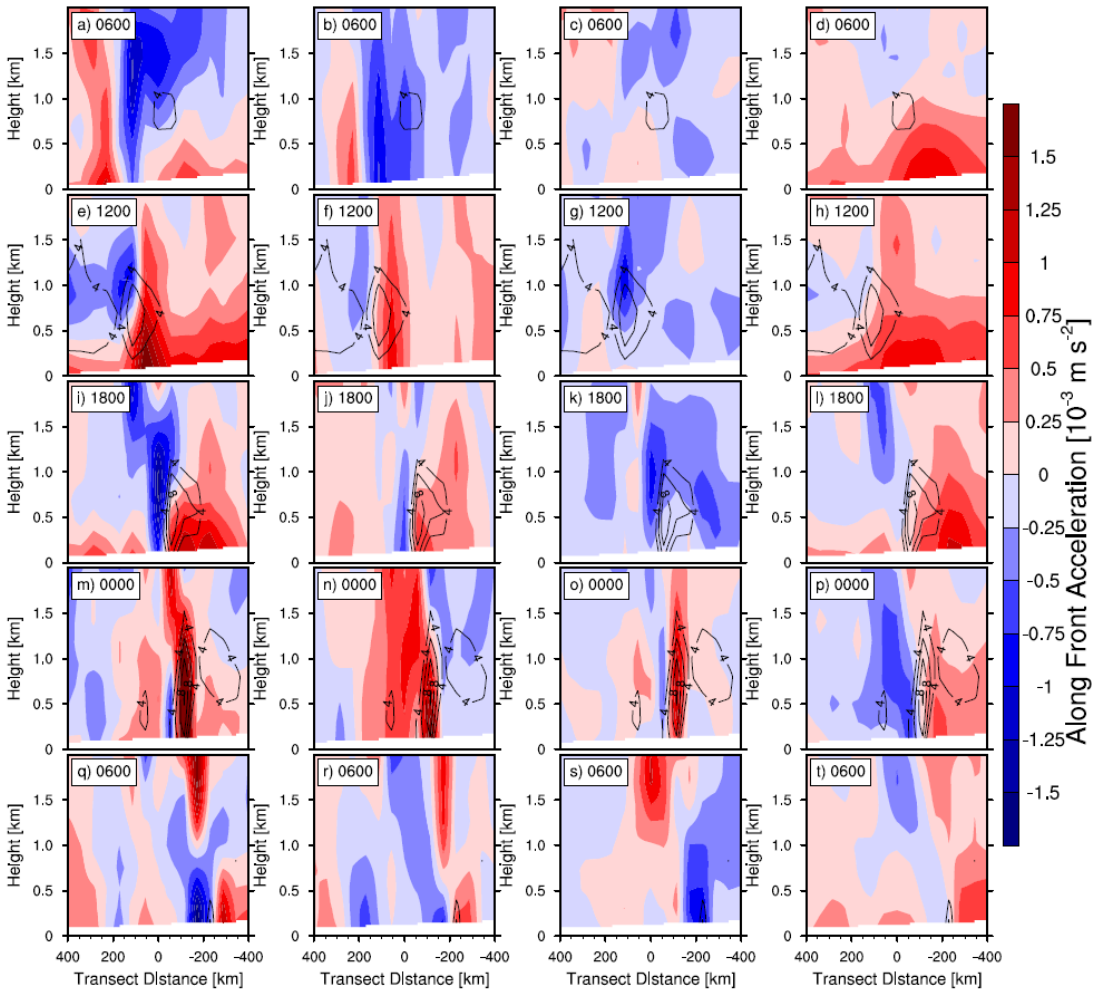

Figure 1.12: A time sequence of the momentum budget from 06:00 UTC 13 February to 06:00 UTC 14 February for the transect shown in Fig. 1.8. Each column contains a different term in the momentum budget with column 1 being the instantaneous tendency (Inst Tend), column 2 the Isallobaric tendency (Isallobaric), column 3 the Advective tendency (Advective), and column 4 the Coriolis torque on the ageostrophic wind (Ageo. Coriolis). The ageostrophic wind normal to the transect is plotted in each plot with a contour interval of 1 m s^{-1} beginning from 4 m s^{-1}.

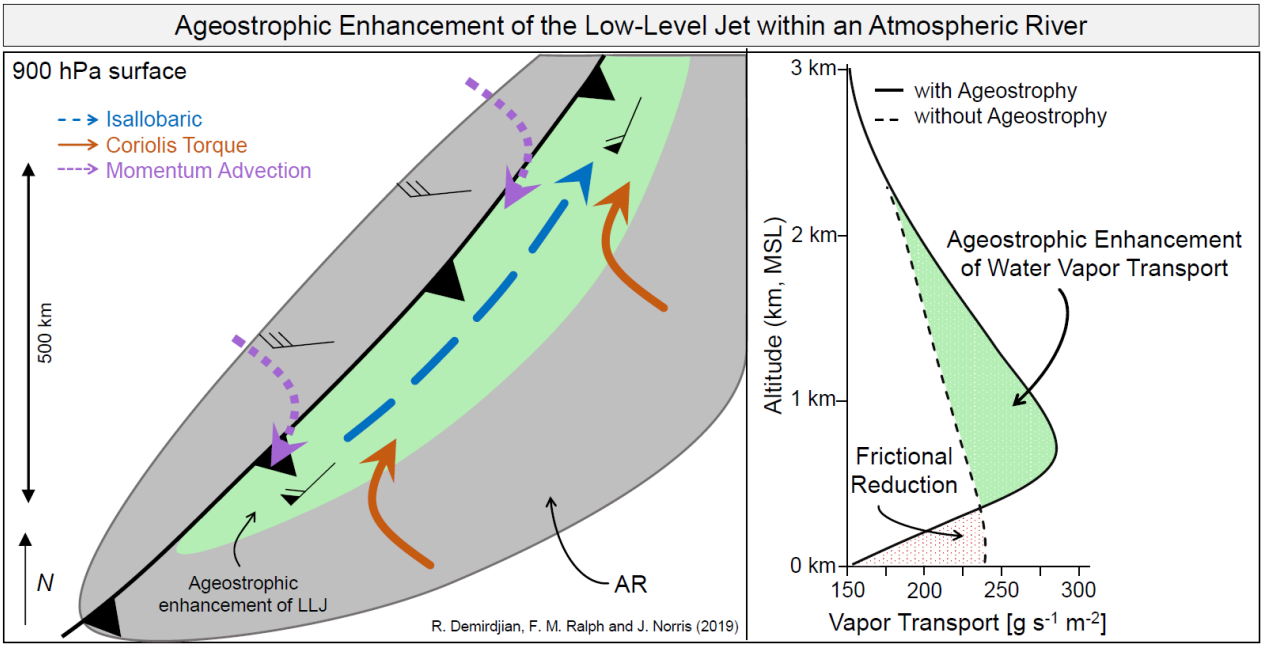

Figure 1.13: A conceptual representation of the enhancement (green) of water vapor transport within the low-level jet due to the ageostrophic winds and the dynamical processes serving to accelerate/decelerate the ageostrophy. A 900 hPa plan-view representation of the forcing mechanisms is shown on the left with the cold front in bold black with triangles, IVT exceeding 250 kg m^{-1} s^{-1} in grey indicating the AR boundaries, and the ageostrophic enhancement of the LLJ in green. The total wind vectors are shown as wind barbs in knots. The acceleration/deceleration vectors are shown with the isallobaric term in long dash blue, Coriolis torque in solid orange, and momentum advection in short dash lavender. A vertical profile of the moisture transport is shown on the right and is representative of any position within the green on the plan-view.

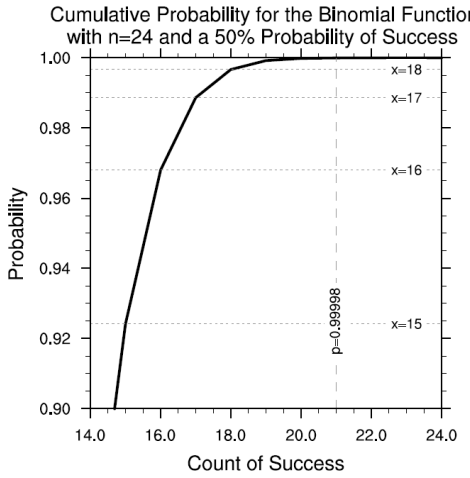

Supplemental 1.1: A cumulative binomial distribution for a sample size of n=24 and a 50% probability of success. The vertical dashed line represents the number of positively ageostrophic cases and the horizontal dotted lines are reference lines to indicate the cumulative probabilities at different counts of success. The number on the vertical line is the two-tail cumulative probability for 21 counts of success and the numbers on the horizontal lines are the counts of success for each line.

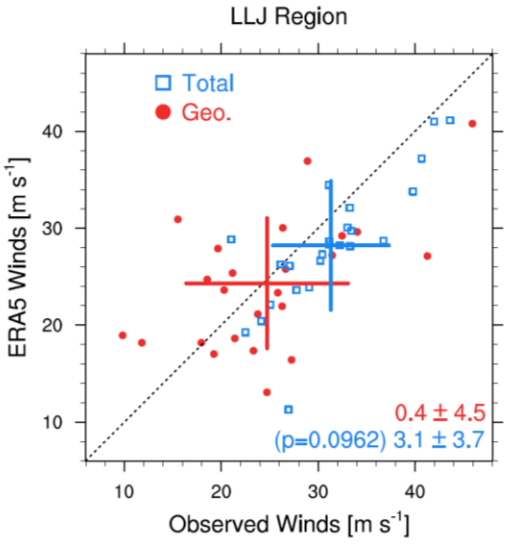

Supplemental 1.2: The same as Fig. 1.7a except that the "Total" winds are not rotated here and are the true total wind speeds.

Chapter 2: A Case Study of the Physical Processes Associated with the Atmospheric River Initial Condition Sensitivity from an Adjoint Model

Abstract

Analysis of a strong landfalling atmospheric river is presented that compares the evolution of a control simulation with that of an adjoint-derived perturbed simulation using the Coupled Ocean/Atmosphere Mesoscale Prediction System. The initial condition sensitivities are optimized for all state variables to maximize the accumulated precipitation within the majority of California. The water vapor transport is found to be substantially enhanced at the California coast in the perturbed simulation during the time of peak precipitation, demonstrating a strengthened role of the orographic precipitation forcing. Similarly, moisture convergence and vertical velocities derived from the transverse circulation are found to be substantially enhanced during the time of peak precipitation, also demonstrating a strengthened role of the dynamic component of the precipitation.

Importantly, both components of precipitation are associated with enhanced latent heating by which: i) a stronger diabatically driven low-level potential vorticity anomaly strengthens the low-level wind (and thereby the orographic precipitation forcing), and ii) greater moist diabatic forcing enhances the Sawyer-Eliassen transverse circulation and thereby increases ascent and dynamic precipitation. A Lagrangian parcel trajectory analysis demonstrates that a positive moisture perturbation within the atmospheric river increases the moisture transport into the warm conveyor belt offshore which enhances latent heating in the perturbed simulation. These results suggest that the precipitation forecast in this case is particularly sensitive to the initial moisture

content within the atmospheric river due to its role in enhancing both the orographic precipitation forcing and the dynamic component of precipitation.

2.1 Introduction

The predictability of atmospheric rivers (ARs) is vitally important for the management of water resources in California (CA) since it is a densely populated region and highly dependent on the arrival, or lack thereof, of just a handful of precipitation events per year (Dettinger 2013; Ralph et al. 2013; Dettinger and Cayan 2014; Ralph 2017; Lamjiri et al. 2017, 2018). DeFlorio et al. (2018) performed an assessment of global ARs and found that at a 2-day lead time, fewer than 75% of the European Centre for Medium-Range Weather Forecasts (ECMWF) ensemble members predicted ARs within 250 km of the actual landfall location, thus motivating the need for forecast improvements in not only the magnitude of the water vapor content in the AR, but also its position. The demand from California water managers for more accurate predictions of both AR strength and landfall position has focused attention on improving numerical prediction systems, as well as aspects of the initial conditions that impact AR characteristics. A version of the Weather Research and Forecasting (WRF) model tailored for the needs of the U.S. West Coast and employed for real time weather forecasts by Martin et al. (2019) demonstrated improved forecast skill over the Global Forecast System (GFS) for 15 landfalling events in CA. Improvements in the initial conditions are being made in part through the AR Reconnaissance (AR-Recon) program which targets ARs using airborne instruments, having an emphasis on the in situ dropsondes (Ralph 2018). The optimal aircraft tracks and dropsondes locations, however, are typically a matter for debate because it is not always clear where additional observations are most likely to improve the analyses and subsequent forecasts. This study focuses on improving the dynamical understanding of how perturbations identified using an adjoint technique grow rapidly and impact AR forecasts.

It has long been understood that small errors in the initial conditions can grow rapidly due to the chaotic nature of the atmosphere (Lorenz 1969). However, an initial condition error of a state variable can have a range of downstream impacts depending on how it projects onto fast growing perturbations (e.g., Reynolds et al. 2001, 2019; Doyle et al. 2014). Atmospheric instabilities are the vehicles through which small errors in the initial state may grow rapidly, thereby contributing towards forecast errors. Aircraft reconnaissance is often utilized to reduce the initial condition errors during impactful weather phenomena by collecting in-situ observations of critical regions where there may otherwise be gaps in the observing systems (Shoemaker et al. 1990; Gray et al. 1991; Martin and Gray 1993; Majumdar 2016). However, the optimal sampling locations providing the greatest improvement to the forecast are often not obvious.

The Naval Research Laboratory (NRL) Coupled Ocean-Atmosphere Mesoscale Prediction system (COAMPS®) including its moist adjoint model (Amerault et al. 2008; Doyle et al. 2012, 2014) was run in real time during AR-Recon in 2018 and 2019 to provide an objective method for determining where short-term forecasts of precipitation over the west coast of North America are most sensitive to changes in the initial state. Although not always the case, the regions highlighted by the moist adjoint tool are often broadly consistent with the forecaster's dynamical understanding of phenomena that would impact the forecast evolution. By comparing dropsondes with short-range forecasts, Lavers et al. (2018) found relative errors of about 20% in the water vapor transport within ARs present in the ECMWF forecast prediction system. Since water vapor transport is highly correlated with orographic precipitation (Alpert 1986; Neiman et al. 2002, 2009a; Lu et al. 2010; Ralph et al. 2013), this suggests that aircraft reconnaissance sampling should be focused in regions of strongest water vapor transport. However, there is evidence that multiple dynamical features on a variety scales may have comparable impact on precipitation forecasts. For

example, Zhang et al. (2019) found that ARs are linked to a parent extratropical cyclone (EC) 80% of the time, suggesting that increased observations, and more accurate analyses, of the dynamically-active regions associated with the development of the EC are also important (Zheng et al. 2013). A dynamical investigation of the sensitivity results and subsequent perturbation growth will both increase understanding of the physical mechanisms that modify AR evolution, and provide context for the use of sensitivity tools for AR-Reconnaissance observing strategies.

The present study is motivated by, and complimentary to, Reynolds et al. (2019), which used the NRL moist adjoint modeling system to evaluate the sensitivity of AR forecasts for January and February 2017. They found that both the accumulated precipitation and the low-level kinetic energy forecast were most sensitive to errors in and around the AR. Furthermore, they showed that the largest forecast sensitivities are from the AR moisture content, followed by temperature and winds, consistent with the results of Doyle et al. (2014) and Doyle et al. (2019) for Atlantic ECs. Finally, they demonstrated that the strength of the initial condition sensitivities correlates well with forecast errors, leading the authors to conclude that the moist adjoint is relevant for predictability and targeted observation applications.

The goal of the present study is to investigate the physical processes responsible for the rapid growth of perturbations derived from a moist adjoint model for an extreme landfalling AR. Out of many different landfalling AR candidates, the 7–9 January 2017 event is investigated because it occurred during the record-breaking precipitation year for Northern California and contained several interesting dynamical features, including a mesoscale frontal wave (Bjerkness and Solberg (1922); Renfrew et al. 1996, Parker 1997, Rivals et al. 1997, and Hewson 2009; Neiman et al. 2016; Martin et al. 2019), which is notoriously difficult to accurately forecast.

2.2 Methods

a) Control and Adjoint Run Descriptions

The January 7–9, 2017 landfalling AR is simulated using the COAMPS modeling system (Hodur 1997; Doyle et al. 2014). The COAMPS model is a nonlinear, nonhydrostatic, compressible, terrain-following numerical model. Our simulation is run on a 221x161 grid with a horizontal grid spacing of 40 km on a Lambert-Conformal grid having 70 vertical levels; output is interpolated onto a pressure grid from 1000 to 200 hPa every 25 hPa and from 200 to 50 hPa every 50 hPa. For a full description of the parameterizations and physics packages, see Doyle et al. (2012; 2019). The relatively coarse resolution of 40 km is chosen because the tangent linear approximation tends to be valid for shorter time periods as resolution becomes finer. Future work will consider higher-resolution experiments for shorter forecast intervals.

The following paragraphs describing the adjoint model closely follows the summaries given in Reynolds et al. (2016, 2019) and Doyle et al. (2014), and is fully described in Doyle et al. (2012). The COAMPS adjoint and Tangent Linear Models (TLM) are described in detail in Amerault et al. (2008) and Doyle et al. (2012). The same physical parameterizations are used in the nonlinear, tangent linear, and adjoint models, including ice-phase microphysics as in (Doyle et al. 2012, 2014, 2019; Reynolds et al. 2019). The longwave and short-wave radiative processes are included in the nonlinear forecasts but are ignored in the TLM and adjoint in order to avoid highly nonlinear components of the physics. The COAMPS forecast and adjoint systems have been used extensively in studies ranging from tropical cyclone (TC) predictability studies (Doyle et al. 2011, 2012; Reynolds et al. 2016), to the 2018 and 2019 AR-Recon field projects (Ralph et al. 2018; Reynolds et al. 2019).

The moist adjoint system represents the sensitivity of a forecast metric J (for model state $\boldsymbol{x}_t$ at time t) to each component of an earlier model state ($\boldsymbol{x}_{t0}$) as

$$J(\boldsymbol{x}_t) = J[\boldsymbol{M}_{\boldsymbol{nl}}(\boldsymbol{x}_{t0})] \ , \qquad (2.1)$$

where J is the response function and $\boldsymbol{M}_{\boldsymbol{nl}}$ is the nonlinear model (see Errico, 1997 for a description of an adjoint model). The response function selected in this study is the 18-h accumulated precipitation averaged over the majority of California (black box in Fig. 2.2). The gradient of J with respect to the initial model state is given by,

$$\frac{\partial J}{\partial \boldsymbol{x}_{t0}} = \boldsymbol{M}_{\boldsymbol{tlm}}^{T} \frac{\partial J}{\partial \boldsymbol{x}_t} \ , \qquad (2.2)$$

where $\boldsymbol{M}_{\boldsymbol{tlm}}$ is the tangent linear model of $\boldsymbol{M}_{\boldsymbol{nl}}$ and superscript T denotes the transpose. The term $\frac{\partial J}{\partial \boldsymbol{x}_t}$ is computed through differentiation of J with respect to the model state at time t. A requirement of J is that it must be a differentiable and continuous function.

This study is focused on the comparison of the nonlinear control forecast (CTL) with that of an adjoint-derived optimally perturbed TLM following the methods of Oortwijn and Barkmeijer (1995), Rabier et al. (1996), and Errico and Raeder (1999). These initial-time perturbations based on the adjoint sensitivity are designed to grow rapidly and result in large changes to the forecast response function. The production of these optimal perturbations follows directly from that used in Doyle et al. (2012, 2014). Perturbations to the response function J are expressed as

$$J' = \sum_j \frac{\partial J}{\partial x_j} x_j' \ , \qquad (2.3)$$

where $\frac{\partial J}{\partial x_j}$ is the gradient of the response function with respect to the jth initial state component. The jth component of the perturbation vector x' is optimal when defined such that

$$x_j' = \frac{s}{w_j}\frac{\partial J}{\partial x_j}, \tag{2.4}$$

for weights w_j. The method for calculating the weights (w_j) and scaling parameter s is detailed in Doyle et al. (2014). The scaling parameter, s (units of J^{-1}), is selected such that the largest perturbation of the water vapor, potential temperature, or zonal wind speed at the initial time does not exceed 1 g kg^{-1}, 1 K, or 1 m s^{-1}, respectively. These perturbation magnitudes are chosen such that they are comparable to, or smaller than, errors assigned to radiosonde and dropsonde observations in the data assimilation system [1 K, 1.8 m s^{-1} and 10% relative humidity at 925 hPa (~1-1.5 g kg^{-1})]. The optimal perturbations are calculated for potential temperature, the Exner pressure perturbation, mixing ratio, all wind speed components, and microphysical species.

b) The Sawyer-Eliassen Transverse Circulation Model

The Sawyer-Eliassen framework is a well-known method for calculating the 2D ageostrophic circulation within a jet-front cross section. Following the methods of (Sawyer 1956; Eliassen 1962; Keyser and Shapiro 1986; Winters and Martin 2014), the Sawyer-Eliassen equation is given by,

$$\left(-\gamma\frac{\partial\theta}{\partial p}\right)\frac{\partial^2\Psi}{\partial y^2} + \left(2\frac{\partial M}{\partial p}\right)\frac{\partial^2\Psi}{\partial p\partial y} + \left(-\frac{\partial M}{\partial y}\right)\frac{\partial^2\Psi}{\partial^2 p} = Q_g - \gamma\frac{\partial}{\partial y}\left(\frac{d\theta}{dt}\right), \tag{2.5}$$

where y is in the across-jet direction, x is in the along-jet direction, Ψ is the ageostrophic streamfunction, θ is potential temperature, $M = U_g - fy$ is the absolute momentum, $Q_g = 2\gamma\left(\frac{\partial U_g}{\partial y}\right)\left(\frac{\partial\theta}{\partial x}\right) + 2\gamma\left(\frac{\partial V_g}{\partial y}\right)\left(\frac{\partial\theta}{\partial y}\right)$ is the quasi-geostrophic forcing term (stretching and shearing deformations respectively), U_g is the along-jet geostrophic wind, V_g is the across-jet geostrophic wind, $\gamma = \frac{R}{fp_0}\left(\frac{p_0}{p}\right)^{\frac{c_v}{c_p}}$, $p_0 = 1000$ hPa, $c_v = 718$ J kg^{-1} K^{-1}, $c_p = 1004$ J kg^{-1} K^{-1}, $R = 287$ J kg^{-1} K^{-1}, f is the Coriolis parameter, and $\frac{d\theta}{dt}$ is the diabatic heating rate. The coefficients on the LHS of

equation (5) represent the static stability, baroclinicity, and inertial stability, respectively. The diabatic heating term is calculated following Emanuel et al. (1987) and Winters and Martin (2014), and is given by,

$$\frac{d\theta}{dt} = \omega\left(\frac{\partial\theta}{\partial p} - \frac{\Gamma_m}{\Gamma_d}\frac{\theta}{\theta_e}\frac{\partial\theta_e}{\partial p}\right) \tag{2.6}$$

where θ_e is the equivalent potential temperature calculated following Bryan (2008), Γ_m is the moist adiabatic lapse rate, and Γ_d is the dry adiabatic lapse rate. Equation (6) was found to be in very good agreement with the direct model output of the latent heating, indicating that the diabatic heating is dominated by latent heating. We use a parametrized form for the diabatic heating because only the instantaneous latent heating rate is available from the model output, which can have some very large heating/cooling gradients and small-scale structure, thereby making it difficult for the numerical routine of equation (5) to converge.

Equation (5) is a second-order elliptic partial differential equation (PDE) which is solved numerically on a grid from 1000 to 100 hPa every 25 hPa in the vertical, and interpolated along a transect of length 2,250 km with a 45-km spacing. It is solved using the method of successive over-relaxation (SOR) in a piecewise manner for the dry $\left(Q_g\right)$ and moist $\left(\frac{d\theta}{dt}\right)$ forcing terms separately. The boundary conditions used are $\Psi = 0$ at all boundaries following Shapiro (1981) and Winters and Martin (2014). All cross sections were manually inspected prior to application of the SOR method to ensure that i) the full jet-front structure is captured, and ii) the boundary conditions were appropriate and did not neglect any important features.

c) Air Parcel Trajectories

Both forward and backward trajectories are utilized in this study, each calculated from 15-minute output, with 25-hPa vertical spacing, on a latitude-longitude grid interpolated to 0.375° x

0.275°. The method applied to calculate both the forward and backward trajectories is a three-step process which 1) determines the 3-dimensional wind components of each air parcel, 2) advances the air parcels forward by a timestep, and 3) linearly interpolates to the new locations at which point (1) – (2) are repeated following Wernli and Davies (1997) and Wernli (1997). This method allows for an adaptable and computationally inexpensive method of estimating the parcel trajectories.

2.3 Case Study Background

a) Synoptic-Scale Overview

The heavy precipitation that fell in California during 7–9 January 2017 was due to a landfalling AR event reaching AR Category 4 (CAT4) out of a scale of 5 (Ralph et al. 2019) having two distinct pulses or waves. At the forecast initialization time (Fig. 2.1a,f), AR Wave 1 (W1) is located ahead of the synoptic scale cyclone's (145W, 36N) cold front and is thereby already associated with a mature EC having a moderate sea-level pressure (SLP) minimum of about 990 hPa and large integrated vapor transport (IVT) values exceeding 800 kg s^{-1} m^{-1}. Following the eastward propagation of a shortwave seen in the SLP field, the AR makes landfall in Central California beginning around 12 UTC on 7 January with an IVT plume containing maximum values located offshore upwards of 750 kg s^{-1} m^{-1} (Fig. 2.1b,g).

A resurgence in the IVT (W2) is apparent in Fig. 2.1c, and is associated with a developing secondary cyclone (C; Fig. 2.1h), also termed a mesoscale frontal wave (Bjerkness and Solberg (1922); Renfrew et al. 1996, Parker 1997, Rivals et al. 1997, and Hewson 2009; Neiman et al. 2016; Martin et al. 2019). This rapid succession of events is consistent with the idea of AR families

(Fish et al. 2019). The mesoscale frontal wave is found to be located not only in the left exit region of the upper level jet (Fig. 2.1h), which is a region favorable for cyclone development, but also along the cold front where strong latent heating is expected. It is thought that the synergy between the forcings at upper and lower levels may be responsible for the development of the mesoscale frontal wave and its intensification into a secondary cyclone. Twelve hours later (Fig. 2.1d,i), after substantial development in both the SLP and IVT, W2 makes landfall as an AR CAT4 with maximum IVT values reaching 1000 kg s^{-1} m^{-1}. By the end of the forecast (Fig. 2.1e,j), the AR has decayed, and the mesoscale frontal wave has propagated poleward to 130W, 47N towards Vancouver.

The Stage-IV (Lin 2011) gridded observational 48-h accumulated precipitation for this case is shown in Fig. 2.2a and exhibits the greatest impacts in three regions: i) the Northern Sierra Nevada Mountains, with values upwards of 200 mm (~8”), ii) along the Northern California coast, with values also upwards of 200 mm, and iii) the Shasta region, with values slightly under 200 mm. While the CTL run simulates the distribution and magnitude of the Stage-IV precipitation pattern reasonably well in the Sierra Nevada range (120W, 37N) and central coast there are some clear biases in the Shasta (124W, 42N) and north coastal regions which results in only a modestly skillful precipitation forecast (Fig. 2.2a,b). The COAMPS forecast likely does not capture the detailed structure of the observed precipitation at this resolution in part because fine-scale orographic features, such as the coastal ranges, are not well resolved. Despite these biases, the analysis undertaken here are still valid as they are focused on understanding the physical mechanisms that lead to changes in the forecast. Modest values of precipitation are evident in Central California around Morro Bay and San Luis Obispo in both the Stage-IV and the CTL run

(Fig. 2.2a,b). As will be discussed in the next section, this is the region where the most substantial precipitation enhancements occur in the perturbed run.

b) Initial Condition Perturbations

The COAMPS moist adjoint model provides an objective method for determining sensitivities of the response function (18-h accumulated precipitation averaged within the box shown in Fig. 2.2) to the initial condition state variables. Informally speaking, this means that the output of the adjoint model produces the amount by which the 18-h accumulated precipitation will change for a given perturbation in a state variable made at the initial time. As described in Section 2.2a, the perturbations that are employed provide the largest change to the 18-h accumulated precipitation possible within the limit of observational uncertainty and are thereby referred to as the optimal perturbations. These optimal perturbations may be conceptualized as patterns highlighting the regions where the forecast is most sensitive to changes in the initial state. For clarity, the various simulations' acronyms used within this study are shown in Table 1. The nonlinear control simulation is simply *CTL*, the perturbed tangent linear model's forecast is *LPF* with difference from the control termed *LPF – CTL*, and lastly the perturbed nonlinear simulation's forecast is *NPF* with difference from the CTL termed *NPF – CTL*.

The initial condition (0h) LPF – CTL are shown in Fig. 2.3 with the CTL run in color fill and the LPF – CTL in the black contours such that solid contours overlaid on positive CTL values indicate an enhancement of the LPF values relative to the CTL. As seen in Fig. 2.3a,b, the 850-hPa optimal perturbations of wind speed and moisture content are situated within and surrounding the tropical moisture plume, or AR, between 130ºW and 140ºW. The 850-hPa moisture is enhanced by up to 0.4 g kg^{-1} within a large fraction of the AR core, around 23ºN, 140ºW, and decreased on the south east edge, around 20ºN, 130ºW (Fig. 2.3b). The 850-hPa wind speed optimal

perturbations are seen to increase the wind speed on the tail of the AR (~23ºN, 140ºW) and near the south eastern edge (~20ºN, 130ºW); maximum values of these perturbations are up to about 0.15 m s^{-1}. The optimal perturbations at the 500-hPa level are situated much farther upstream of the AR compared to the lower levels, and are located near a jet entrance region (Fig. 2.3c,d). The fact that the perturbations occur farther upstream with increasing altitude is consistent with the advective speed being much greater at upper levels; if these perturbations are to impact the forecast during the same time period as the lower levels, they must be situated farther away. This is also consistent with the structure of the sensitivities being tilted against the shear (Doyle et al. 2014, 2019; Reynolds et al. 2019) and can be interpreted as growing through potential vorticity (PV) unshielding, which is the result of a superposition of PV maxima, as in the Orr mechanism (Orr 1907; Badger and Hoskins, 2001; Reynolds et al. 2001).

2.4 Results

a) Evolved Perturbations

The remainder of the manuscript will be focused on the evolution of the optimal perturbations and the dynamical differences between the CTL and the LPF. The difference in 48-h accumulated precipitation between CTL and LPF is shown in Fig. 2.2c and exhibits a long narrow band of enhanced precipitation centered at the latitude of Central California (~35ºN) and a modest reduction in precipitation poleward of 36º N. The dipole structure of the precipitation band suggests a shift in the LPF's AR position, however, as will be demonstrated later in this section, the first order change is in the AR's strength. The fact that the band of enhanced precipitation extends far offshore, away from any topographic features, indicates that it is driven in part by a dynamical mechanism. Similarly, the enhancement over land may be suggestive of orographic

effects on precipitation seen at both the coastal mountain ranges of San Luis Obispo (121W, 35N) and the southern Sierra Nevada mountains (119W, 35.5N). The optimal perturbations are formulated to increase precipitation in the LPF compared to the CTL during the last 18 h of the 48-h forecast. The LPF minus CTL domain-averaged 18-h accumulated precipitation is about 3 mm, which is evident when comparing the deeper blue colors to the lighter brown in Fig. 2.2c. Though this may seem small, it is important to emphasize that this is the overall regional average which is offset by some areas of reduced precipitation.

While the perturbations have been tailored to optimize the precipitation in a linear context, the nonlinear growth of the perturbations may also be examined by making a nonlinear forecast from the optimally perturbed initial state. It is important to compare the forecast of the LPF with the NPF because substantial differences between the two runs may indicate the dominance of non-linearities, which are not represented within the LPF. The 48-h accumulated precipitation of the NPF minus CTL, is shown in Fig. 2.2d. A comparison of the difference fields (Fig. 2.2c,d) shows that they are qualitatively similar, indicating that within the 48-h forecast, the non-linearities are sufficiently small such that the linear and nonlinear precipitation perturbations are similar. Therefore, we are confident in moving forward with analyzing the LPF in more detail.

In order to perform a diagnostic analysis on the differences between the CTL and LPF runs, it is necessary to clarify when in time the evolved perturbations may be leading to the precipitation enhancement. A time series is shown in Fig. 2.4 of the average accumulated precipitation at 15-minute intervals in a region that isolates the precipitation enhancement between the bottom of the response function box up to 36ºN indicated by the bold, black dotted line in Fig. 2.2c. The LPF's enhanced precipitation period begins at 26h, four hours prior to the response function accumulation period. This is followed by strong growth in the precipitation enhancement that occurs for about

10 h from 26h to 36h, after which time both the CTL and LPF continue to accumulate precipitation at about the same rate.

The same method of averaging is applied to the IVT field to quantify the role of the orographic precipitation forcing (i.e. moisture transport; Neiman et al. 2016; Martin et al. 2019) within the LPF's enhanced precipitation field (Fig. 2.4). As can be seen here, elevated values of the LPF's IVT begin at about 24h, just prior to the start of the period of enhanced precipitation, and end at the same time (36h). Furthermore, it should be noted that while the percentage increase in IVT in Fig. 2.4 may seem modest, a map of the difference in IVT between the LPF and CTL (not shown) has a complex pattern of positive and negative values, suggesting that IVT can be more locally enhanced than what is reflected in the regional average. Since moisture transport has been shown to correlate well with orographic precipitation (Neiman et al. 2002, 2009a; Ralph et al. 2013), this increase in IVT supports the hypothesis that the observed precipitation enhancement is partially due to the increased orographic precipitation forcing.

To further investigate the forcing for orographic precipitation, we examine the components of low-level water vapor transport within the 10-h time period of precipitation enhancement in more detail. From 24h through 36h, a warm front propagates ahead of the AR (Fig. 2.5e–h). In this same area as the moisture plume, strong low-level wind speeds directed from the SSW are evident in the CTL run (Fig. 2.5a–d), indicating a region of very large moisture transport. At 24h (Fig. 2.5a,e), 2 h before the enhanced precipitation time period, a strengthening is observed in both the 850-hPa LPF – CTL wind and moisture content behind the warm front. Over the course of the next 8 h, through 32h, the LPF – CTL wind speed enhancement intensifies substantially while simultaneously propagating north-eastward and making landfall (Figs. 2.5b,c). At 28h, the moisture enhancement intensifies while remaining coincident with the region of enhanced wind

speed (Fig. 2.5f). By 32h (Fig. 2.5g), the moisture is no longer enhanced behind the warm front, likely a result of the greater precipitation taking place. Finally, at 36h (Fig. 2.5d,h) both the LPF – CTL wind and moisture content are reduced behind the warm front. As mentioned previously, the increase in vapor transport supports the hypothesis that the precipitation enhancement is partially due to a greater orographic precipitation forcing.

During this same time period, from 24h through 36h, an intensifying narrow band of moisture convergence ($-q_m \nabla \cdot \vec{u}$) and low-level PV is situated behind the warm front in the CTL (Fig. 2.6). At 24h (Fig. 2.6a,e), there is already substantially enhanced moisture convergence behind the warm front in the LPF – CTL, which results in diabatic generation of PV. Over the next 8 h, both the moisture convergence and PV are enhanced in LPF – CTL while the system is making landfall (Fig. 2.6b–c,f–g). Since the CTL fields are also intensifying during this time period, the fact that the LPF – CTL field is enhanced at these times shows that the rate of intensification for these quantities is greater in the LPF than the CTL. By 36h, the coherent moisture convergence dipole structure off the CA coast in the LPF – CTL is less apparent while the PV dipole appears relatively unchanged (Fig. 2.6d,h). Just as Fig. 2.5 indicates that the forcing for orographic precipitation is enhanced within the LPF, Fig. 2.6 shows that dynamically driven precipitation is enhanced through moisture convergence.

To provide analysis of the vertical structure, Fig. 2.7 shows a cross section taken across the warm front (location shown in Fig. 2.5c) at the start of the response function integration time (forecast hour 30) in which the precipitation enhancement is occurring. At this time, the CTL exhibits strong wind speeds of up to 25 m s^{-1} at 900 hPa situated on the southeast side of the low-level PV anomaly centered on the front (Fig. 2.7a,b). A dipole structure is observed in the LPF – CTL low-level wind speed (Fig. 2.7a), where enhancements of up to 6 m s^{-1} indicate the clear

development of a low-level jet at 900 hPa which was not present in the CTL simulation. At first glance, this may seem to be a shift in the wind speed locations, but examination of the total LPF wind fields (not shown) compared with that of the CTL clearly shows the winds are enhanced up to 20% rather than shifted. In fact, the location of this dipole is centered on the PV enhancement (Fig. 2.7b), which matches the expected horizontal circulation change due to low-level latent heating as investigated by Lackmann (2002). Importantly, the mixing ratio enhancements (Fig. 2.7d) are found to overlap the region of strengthened wind speed, consistent with the observed enhancement of IVT. The reason that the region of enhanced vapor transport is not directly coincident with the enhanced precipitation in this cross section is because the section location is well offshore where orographic influences are not present.

Strong vertical motion that is vertically sloped and oriented along equivalent potential surfaces occurs in the CTL (not shown) and also approximately along the region of moisture convergence (Fig. 2.7c,e). Examination of equivalent potential temperature and absolute momentum (not shown) clearly indicate that this sloped region is symmetrically unstable, demonstrating that perturbations are expected to grow rapidly there. Contrastingly, the LPF – CTL vertical motion clearly has two distinct regions, one with a slantwise orientation, similar to that of the CTL, and the other with a distinct vertical orientation (Fig. 2.7c,e) consistent with deep convection as in Cordeira et al. (2013). Cross sections of convective available potential energy (CAPE; not shown) indicate that the LPF has an environment that is more conducive to convection. A greater degree of convection is likely also a component of the precipitation enhancement, although this is not investigated further here, and thus remains an open question for future work. As demonstrated by the clear increase in both the vertical ascent and vapor transport, the cross

sections further support the hypothesis that the observed precipitation enhancement is a result of contributions from the dynamic precipitation component and orographic precipitation forcing.

b) The Transverse Circulation

The Sawyer-Eliassen transverse circulation model, which produces the vertical and cross-frontal ageostrophic circulation perpendicular to the upper level jet structure in an approximately straight flow, is used to further investigate the dynamical component of the precipitation enhancement by separating the vertical velocity and moisture convergence into moist and dry components. Here, the moist processes are due to the latent heating effects while the dry forcing components arise from quasi-geostrophic shearing and stretching deformation contributions (see Keyser and Shapiro 1986 and Winters and Martin 2014 for a more in-depth description). The dry and moist components are obtained by solving the equation in a piecewise manner by using the dry and moist forcings individually within the PDE solver. Note that Figs. 2.8–2.9 show only a subset of the full PDE solver's domain to match the previous cross sections in Fig. 2.7.

While the Sawyer-Eliassen model directly yields the components of the transverse circulation (v_{ag}, ω), we investigate the moisture convergence rather than v_{ag} because it is more relevant for explaining the precipitation enhancement. The Sawyer-Eliassen derived moisture convergence is calculated in three steps: 1) solve the Sawyer-Eliassen equation for the ageostrophic stream function (Ψ), 2) calculate the cross-jet ageostrophic wind using the equation $v_{ag} = -\frac{\partial \psi}{\partial p}$, and 3) assume 2D convergence in the plane of the cross section such that $MConv = -q_m \frac{\partial \mathrm{v_{ag}}}{\partial y}$ where y is the cross-jet streak direction. The Sawyer-Eliassen derived total moisture convergence (Fig. 2.8a) is calculated along the same transect as Fig. 2.7, and compares very well with the full 3D model calculated moisture convergence in regard to strength, slope, and vertical

extent (Fig. 2.7e). Similarly, the Sawyer-Eliassen model reproduces the LPF – CTL moisture convergence very closely in terms of strength, slope, and vertical extent (solid black contours), though it has a maximum at the surface (Fig. 2.8a), while the real case (Fig. 2.7e) is slightly elevated from the surface. Therefore, despite the assumptions included in the Sawyer-Eliassen equation, it still provides a very accurate depiction of the transverse circulation in this case.

The main utility of the Sawyer-Eliassen model for this analysis is the ability to separate the transverse circulation into the dry and moist components. The geostrophic (dry) and the diabatic (moist) components of moisture convergence shown in Fig. 2.8b and Fig. 2.8c, respectively, clearly illustrate that the moist component is dominant. The dry component is constrained to the very lowest levels (Fig. 2.8b) with peak values being much smaller than those observed (Fig. 2.7e). Conversely, the moist component has peak values, slope, and vertical extent that are much closer to that of the CTL (Fig. 2.8c). With that said, the dry component is not negligible. Furthermore, it is important to be cognizant that this analysis is only at a single time, which raises the question of what role the dry component had at an earlier time. Did the dry component have much greater strength earlier on? Did the LPF – CTL dry component at an earlier time initiate the LPF – CTL moist component? These questions will be addressed in Section 2.4c.

Vertical velocity can also be calculated from the Sawyer-Eliassen analysis by using $\omega = \frac{\partial \psi}{\partial y}$ (Fig. 2.9). Comparison of the total Sawyer-Eliassen derived vertical velocity (Fig. 2.9a) to that of the 3D model output (Fig. 2.7c) indicates it is also accurate, though not to the degree of the moisture convergence comparisons. The CTL vertical velocity derived by the Sawyer-Eliassen method retains the sloped orientation and vertical extent but is biased low in magnitude. This is attributed to the fact that it is a modestly convective region as indicated by the CAPE values (~300 J kg^{-1}; not shown), which is not accounted for by the Sawyer-Eliassen analysis. Similarly, while

the slope and vertical extent of LPF perturbation vertical velocities are reproduced well, there is a low bias in magnitude. It is important to note that the vertically upright orientation of LPF perturbations (Fig. 2.9a) is reproduced very well in the Sawyer-Eliassen model implying that it is not only due to convection but also a result of the forced ascent. As in the results for moisture convergence, the vertical velocity is dominated by the moist component term at this time.

c) Pseudo-Lagrangian Evolution of the Transverse Circulation

The transverse circulation analysis above applies only to one cross section at a single time, so a complimentary analysis is undertaken by initializing backward trajectories from the central point along the cross section of Figs. 2.7–2.9 to investigate a system-relative evolution of the transverse circulation. At each point along each trajectory in Fig. 2.10a, a cross section is drawn to be nearly perpendicular to the upper-level jet streak (not shown). This establishes a pseudo-Lagrangian cross section time series for each trajectory. It is important to note that it is called "pseudo-Lagrangian" because it assumes that the entire cross section moves together, which, of course, is not the case. Despite this caveat, animations of the cross sections along the pseudo-Lagrangian trajectory produce what seem to be an accurate depiction of how the system-relative cross-section evolves (not shown).

While the pseudo-Lagrangian cross section time series can address whether the results in Section 2.4b are applicable for other times, it does not address the spatial issue. A simple way to investigate how the results from Section 2.4b may vary spatially is to initiate the backward trajectory at the same point as in Fig. 2.10a, but at different times. Since the system is moving, this will ensure that different portions of the AR are sampled. This was done for backward trajectories initiated at 24h through 36h with each air parcel moving all the way backwards to the initial time

at 0h (Fig. 2.10a). This method produces 13 pseudo-Lagrangian cross section time series each for CTL and LPF from which the following analysis is comprised.

The strength of the Sawyer-Eliassen transverse circulation for each component is measured from the maximum value of -ω for each time step along the pseudo-Lagrangian cross section. This is repeated for each of the 13 pseudo-Lagrangian trajectories, and then averaged by aligning them on the respective final trajectory times (Fig. 2.10b). Consistent with previous results, the strength of the LPF – CTL vertical velocity is found to be substantially greater than that of the CTL. Furthermore, the moist component is dominant from about 10h onwards in both the CTL and LPF; the dry component remains very steady from beginning to end. This analysis shows that dominance of the moist component of the transverse circulation applies not only to a single transect at a single time, but consistently influences the dynamics of the transverse circulation for the system as a whole.

A major benefit of creating a time series of the transverse circulation strength is that it allows us to form conclusions about its evolution. It reveals that the LPF's vertical velocity enhancement is initiated from the moist component starting at about 12h (Fig. 2.10b), at which time the slope of the LPF curve becomes greater than the CTL. Sustained LPF vertical velocity growth continues up until about 26h at which point the CTL remains steady, and the LPF begins to decline in strength. The CTL and LPF total vertical velocities are clearly controlled by their respective moist components with the dry components providing a small, but steady contribution. Both the CTL and LPF have very similar dry component strengths, indicating that the quasi-geostrophic shearing and stretching environments are approximately the same between the different runs.

The decomposition of the moist and dry forcings in the Sawyer-Eliassen transverse circulation analysis suggests the possibility of a positive feedback mechanism. Latent heating at the developing frontal boundary provides a positive forcing to the Sawyer-Eliassen circulation. This positive forcing in turn leads to moisture convergence, which may then drive further latent heat release. While it is outside of the scope of this study to prove that this is indeed a feedback mechanism, it is still clear that the dynamical component of the vertical velocity is highly dependent on the nature of the moist processes and, thereby, on the moisture content.

d) Lagrangian Evolution of the Optimal Perturbations

Until this point, this study has been focused on the evolved perturbations with only some minimal connections to the initial optimal perturbations. To address this gap, forward trajectories are utilized to investigate how the optimally perturbed regions may connect to the downstream processes described previously. Forward trajectories are initialized on the 700-hPa level, where the largest moisture perturbations were made, at 0h in a 11x11 square block with a 40-km spacing and centered on the maximum positive initial condition moisture perturbation (Fig. 2.11a). This will enable the initial perturbations to be connected to the moist transverse circulation analysis already discussed. It is clear from Fig. 2.11a that the LPF trajectories are more tightly clustered than the CTL trajectories, consistent with stronger convergence from the enhanced transverse circulation.

The average Lagrangian (along air parcel trajectory) moisture content, PV, and pressure are shown in Figure 2.11b for the CTL and LPF. To ensure that the shape of the averaged curves is representative of the individuals, each trajectory is shifted in time to match a clear rise in moisture content (Fig. 2.11b, at 23h) immediately followed by a sharp decline, which is a feature found to be present among all trajectories. The average time axis among all of the trajectories is

used in order to provide a sense of the time scale. The three subplots in Fig. 2.11b illustrate a three-phase sequence, which is not only very consistent with the previous results pertaining to the transverse circulation, but also ties the sequence of events back to the initial perturbations. At the start of phase I (6h to 20h), it is clear that the LPF air parcels have enhanced moisture content, a direct result of the perturbation. As phase I progresses, both the CTL and the LPF moisture content have a very small, but steady increase, with the LPF maintaining greater moisture throughout. No substantial changes occur for PV or pressure during this phase for these trajectories.

Phase II (20h to 24h) is short but distinctly indicates that the growth rate of the moisture content in both the LPF and the CTL increases noticeably. During this time, a rise in PV indicates that diabatic generation has begun, with the perturbed LPF exhibiting a substantially greater increase than CTL. Both observations are consistent with the moisture convergence processes previously described, which can cause an increase in moisture content and serve to diabatically generate PV. Throughout phase II, the air parcel pressure remains mostly steady with only a modest decrease in height (increase in pressure).

Lastly, in phase III (24h to 30h), the air parcels begin their rapid ascent in the warm conveyor belt (Wernli and Davies 1997; Wernli 1997; Schemm et al 2013) which is also confirmed from the plan-view sequence shown in supplemental 2.1. The PV reaches a maximum, and the moisture content rapidly decreases, likely due to precipitation. During the first few hours of phase III, the LPF ascent rate is initially much greater than that of the CTL and, in turn, it reaches a higher overall elevation by 30h. The LPF's enhanced ascent rate and PV is consistent with the analysis of the transverse circulation in Sections 2.4b–c in that stronger moist processes lead to greater ascent. This coherence suggests that the physical process leading to the observed Lagrangian evolution in Fig. 2.11b are actually those described by the transverse circulation.

A similar analysis is performed by initializing another 11x11 box of air parcels centered on the negative moisture perturbation at approximately 26.5º5N, 135.5º5W. The parcel trajectories (not shown) terminate in Southern CA and Northern Baja, Mexico (117W, 32N), which is outside of the response function domain. Therefore, the Lagrangian approach to understanding the mechanism for increasing precipitation is not applicable to this region, and the impact on precipitation from these perturbations must be coming from changes to the evolving dynamics not captured in a Lagrangian framework. For example, it may be that the negative perturbations are associated with changes to the initial cyclone (AR wave 1) and not the frontal wave (AR wave 2).

The consistency between the Lagrangian evolution of the optimal moisture perturbation with the enhancements observed in the transverse circulation provides a connection between the initial perturbations and their downstream modifications of important physical processes. The forward trajectory analysis supports the hypothesis that the positive moist optimal perturbations are positioned, at least in part, to provide more moisture available for enhanced latent heat release. Enhanced latent heating leads to an increase in the dynamical component of the precipitation through the enhanced transverse circulation. This analysis demonstrates the utility of the Lagrangian air parcel trajectory method in tracking the evolution of the optimal perturbations. While outside the scope of this work, a future study could initialize air parcels in this way for different areas within all the largest initial condition perturbation areas and track their evolution.

2.5 Conclusions and Discussion

This study is focused on understanding the nature of rapid perturbation growth in a tangent linear model for an extreme landfalling AR. The perturbed tangent linear forecast (LPF) has been

optimized following Doyle et al. (2019) to enhance the final 18h of the accumulated precipitation in an area of California and within the constraints of analysis uncertainty. In agreement with Cannon et al. (2018), the analysis presented here demonstrates that the precipitation enhancement in the perturbed run is a result of both the enhanced orographic precipitation forcing and the dynamic precipitation component. Importantly, evidence suggests that the enhancement of both components originate from the same latent heating process, thereby making the precipitation forecast particularly sensitive to errors in initial condition moisture content.

The sequence of events in which the moisture perturbations enhance precipitation is illustrated schematically in Fig. 2.12. At T+00, the positive moisture perturbation is initiated on the periphery of the AR where it is gradually fed into the developing frontal zone. Starting at T+12, PV is diabatically generated at the frontal zone through moisture convergence and the subsequent release of latent heat. The wind field responds to the PV anomaly by increasing/decreasing on the warm/cool side of the front following Lackmann (2002), thereby leading to a local enhancement of moisture transport. The transverse circulation responds to the latent heat release by strengthening the moisture convergence and ascent at the frontal zone. During this development, the moisture perturbation remains mostly unchanged and continues its way toward the front. Finally, at T+24, the moisture perturbation reaches the frontal zone leading to substantial latent heat enhancements. This additional heating enhancement, along with the sustained latent heating independent of the perturbation, drives an even greater moisture transport through the generation of a stronger PV anomaly, and an amplification in the transverse circulation as described by the Sawyer-Eliassen model.

The observation that the initial moisture perturbation is fed into the region of moisture convergence aligns well with the results of Reynolds et al. (2019) and Doyle et al. (2014, 2019).

They found that the optimal perturbations within ARs exhibit upshear tilts which can extract energy from the mean flow through the PV unshielding mechanism. The results presented here are consistent with the hypothesis that the physical "reason" why the moist adjoint sensitivity adds moisture within the AR for this case is so that it may serve to enhance latent heating processes and thereby enhance both the orographic and dynamic components of the precipitation.

Clearly, moist processes are critically important in the development of the strong transverse circulation, which is itself responsible for the strong moisture convergence and latent heating. Since the Sawyer-Eliassen model is also forced by a latent heating term, these results suggest a feedback mechanism whereby the latent heating is both a source and a consequence of the transverse circulation. This may be important from a predictability standpoint because it demonstrates a mechanism by which small changes in the initial moisture content can lead to large changes in the forecast downstream. For example, targeted observational campaigns should closely consider sampling in the moist regions which feed into the transverse circulation since any error in those regions can grow substantially. Furthermore, since the transverse circulation is frequent component of ECs, and ECs are often accompanied by ARs (Zhang et al. 2018), the results of this case study are likely to be representative of a large number of ARs.

Acknowledgements

This work was supported by the US Army Corp of Engineers from the Award USACE W912HZ-15-2-0019. The authors would like to thank the support of the entire CW3E team for their useful thoughts and comments on this work. In particular we thank Luca Delle Monache, Forest Cannon, Anna Wilson, Julie Kalansky, Caroline Papadopoulos, and Brian Kawzenuk. The

lead author acknowledges C. A. R. and J. D. D. gratefully acknowledge the support of the Chief of Naval Research through the NRL Base Program, precipitation enhancement 0601153N. Computational resources were provided by the Navy DSRC in Stennis, Mississippi.

Chapter 2, in full, is a reprint of the material as it appears in the Journal for Atmospheric Sciences. Demirdjian, R., J.D. Doyle, C.A. Reynolds, J.R. Norris, A.C. Michaelis, and F.M. Ralph, 2020: A Case Study of the Physical Processes Associated with the Atmospheric River Initial-Condition Sensitivity from an Adjoint Model. *J. Atmos. Sci.,* 77, 691–709, https://doi.org/10.1175/JAS-D-19-0155.1 The dissertation/thesis author was the primary investigator and author of this paper.

Tables and Figures

Table 1: The descriptions of acronyms used in this study.

Acronym	Description
CTL	Control nonlinear forecast
LPF	Linear Perturbed Forecast: The sum of the control nonlinear forecast and the optimal perturbation evolved using the Tangent Linear Model.
NPF	Nonlinear Perturbed Forecast: The nonlinear forecast run from an analysis which is the control analysis plus the initial optimal perturbation.
LPF – CTL	Linear Perturbation: The optimal perturbation evolved using the Tangent Linear Model, equivalent to the difference between CTL and LPF.
NPF – CTL	Nonlinear Perturbation: The difference between CTL and NPF.

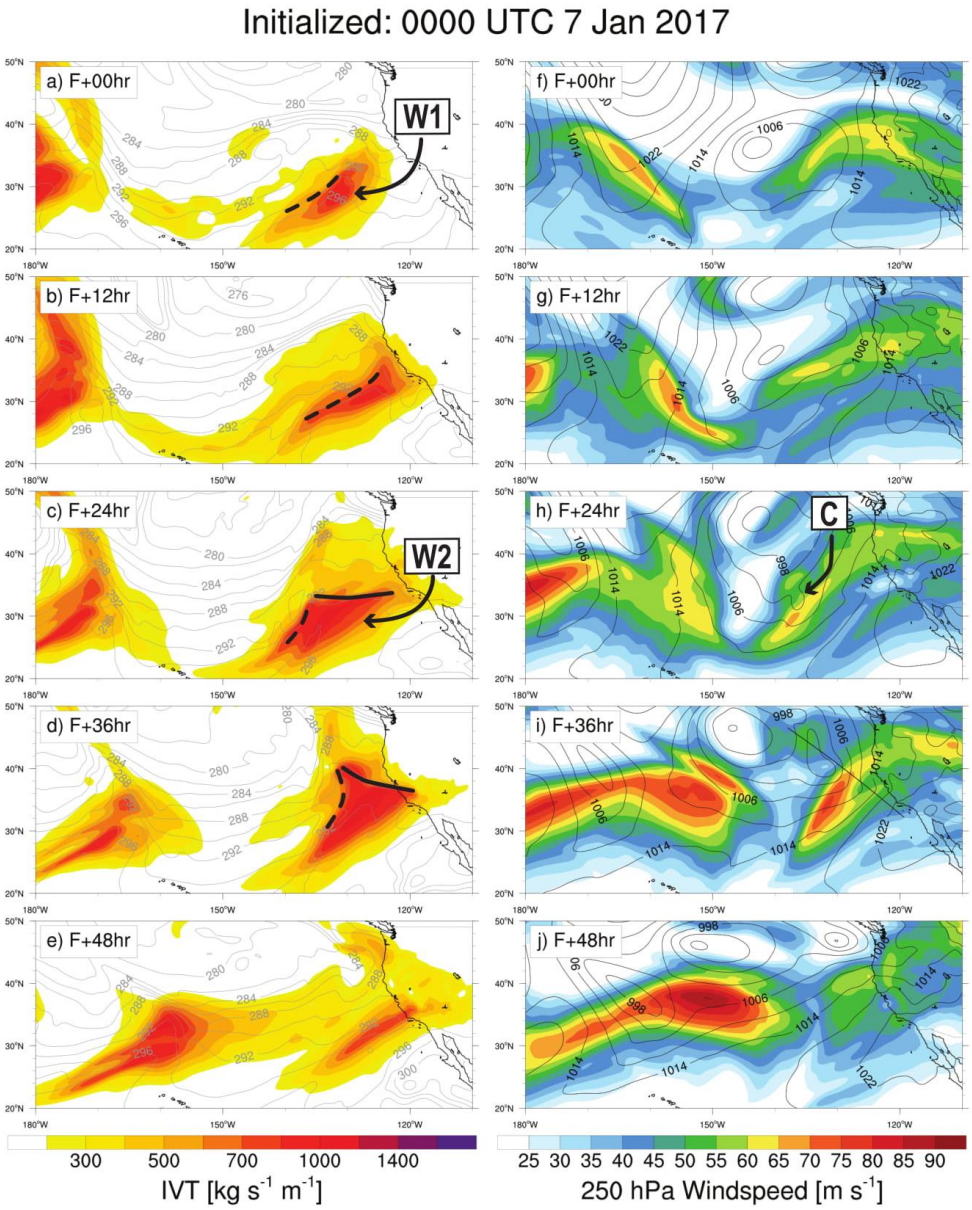

Figure 2.1: Plan-view maps every 12 hours of the a)–e) control run IVT (kg s-1 m-1; shaded) and 925-hPa potential temperature (contour interval of 2 K; solid gray), and f)–j) 250-hPa wind speed (m s-1) and SLP (contour interval of 4 hPa; solid black). The surface fronts are shown in (a – d) with the cold front in black dashed and the warm front in solid black. The location of a transect for Figures 2.7–2.9 is shown in (i) as a solid black line. The "W1" and "W2" labels refers to different AR waves, and the "C" label refers to a developing secondary cyclone (see text for discussion).

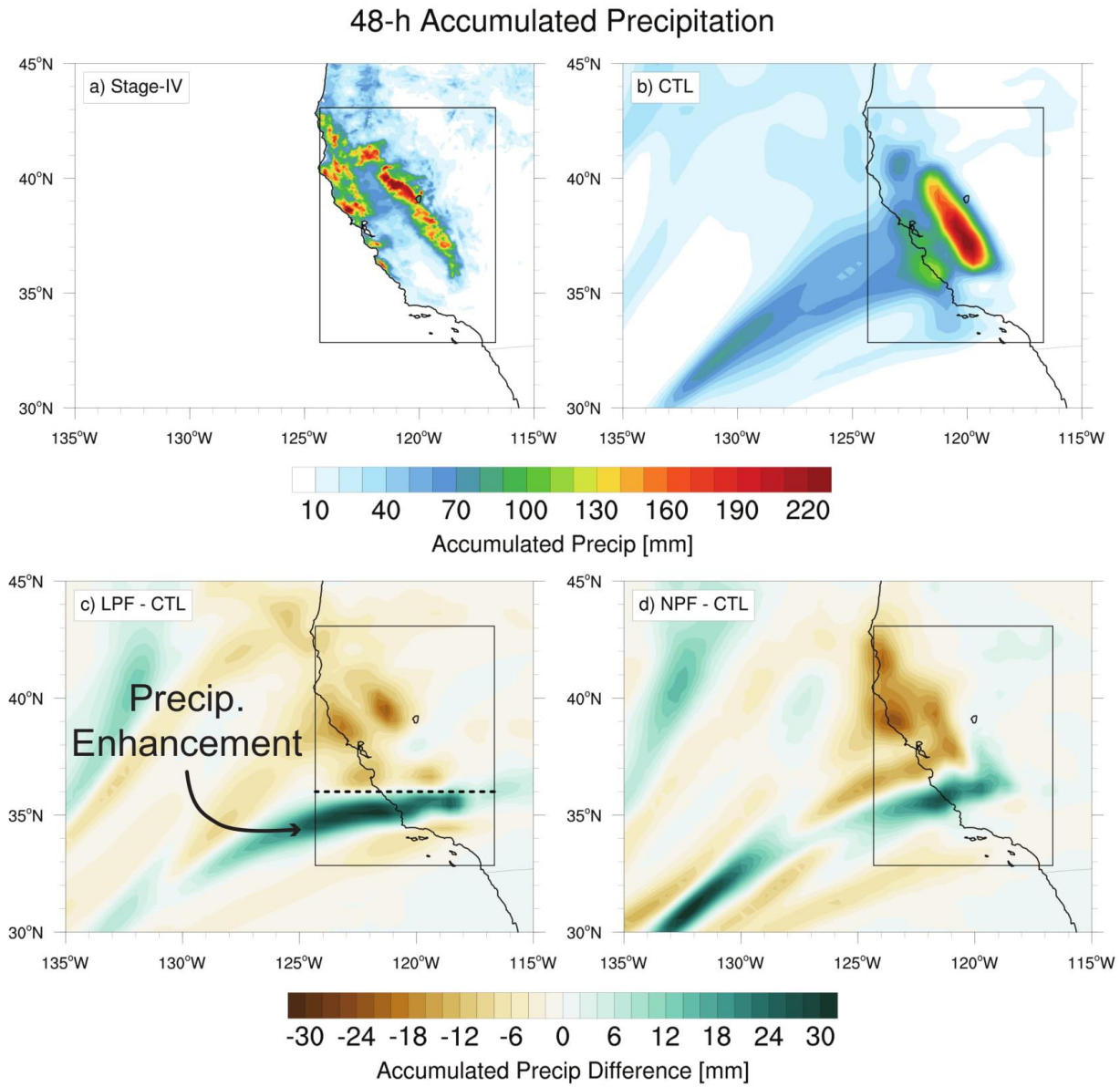

Figure 2.2: Plot of the a) Stage-IV and b) CTL 48-h accumulated precipitation (mm), and c) linear perturbations (LPF minus CTL) and d) nonlinear perturbations (NPF minus CTL) 48-h accumulated precipitation difference fields. The response function box is shown in the solid black box. The thick horizontal dotted black line across the response function box in c) separates the precipitation enhancement and reduction regions used in Figure 2.4 within the box. The precipitation enhancement is identified in c).

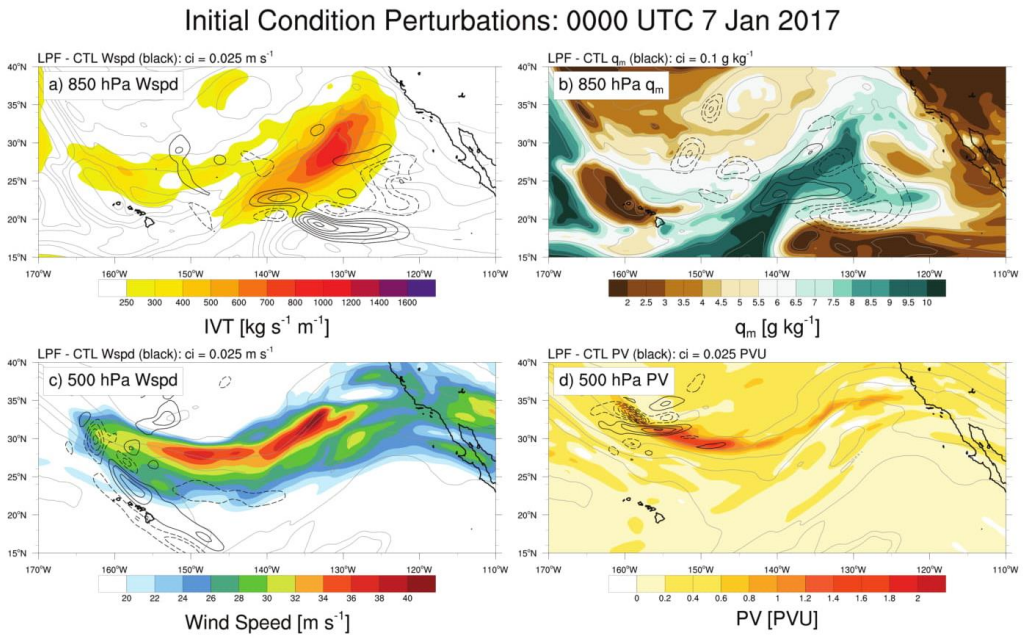

Figure 2.3: The initial condition perturbations for the a) 850-hPa wind speed with IVT contours (kg s-1 m-1; shaded), b) 850-hPa mixing ratio, (g kg-1; shaded), c) 500-hPa wind speed (m s-1; shaded), and d) 500-PV with the LPF-CTL in solid black (positive) and dashed black (negative) contours for each respective field. The solid gray contours in each plot are the equivalent potential temperatures on the respective levels with contour interval (ci) = 4 K and five passes of a 5-point local smoother applied.

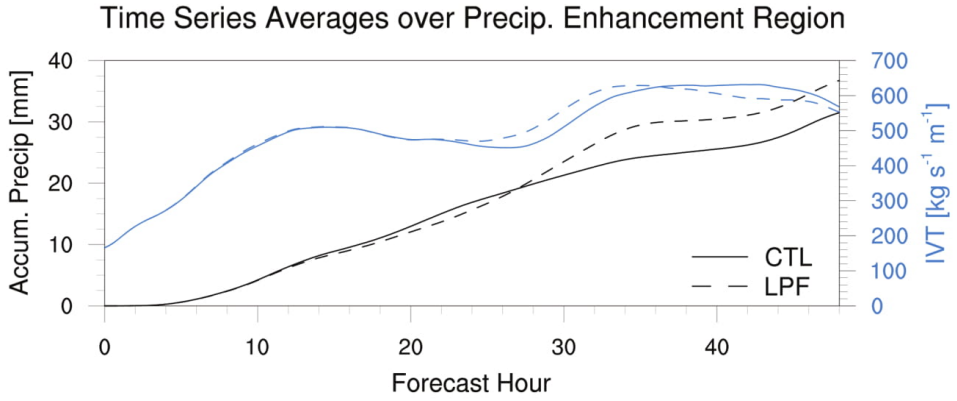

Figure 2.4: Time series of average accumulated precipitation (black) and the IVT (blue) within the sub-region of Figure 2.2c (see text). The control (CTL) run is shown in the solid lines and the linearly perturbed (LPF) run in dashed.

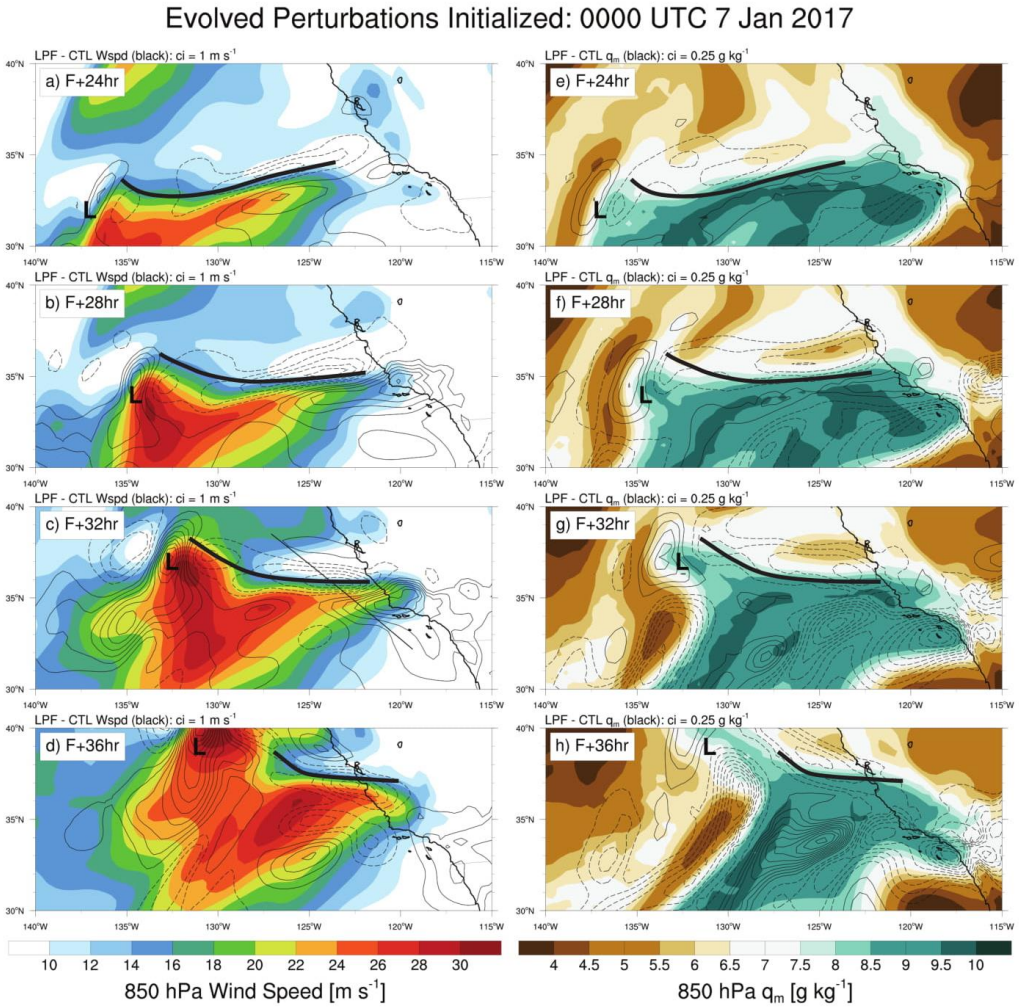

Figure 2.5: Plan view every 4 hours beginning from 24 h of the 850-hPa a)–d) wind speed (m s-1; shaded) , and e)–h) water vapor mixing ratio (g kg-1; shaded). The LPF-CTL fields are shown in black with solid being positive and dashed being negative values. The approximate position of the low-pressure center of the developing secondary cyclone is labelled "L" and the warm front indicated by the thick black curved line. The position of a transect used in Figs. 2.7–2.9 is shown in c) in the thin black straight line.

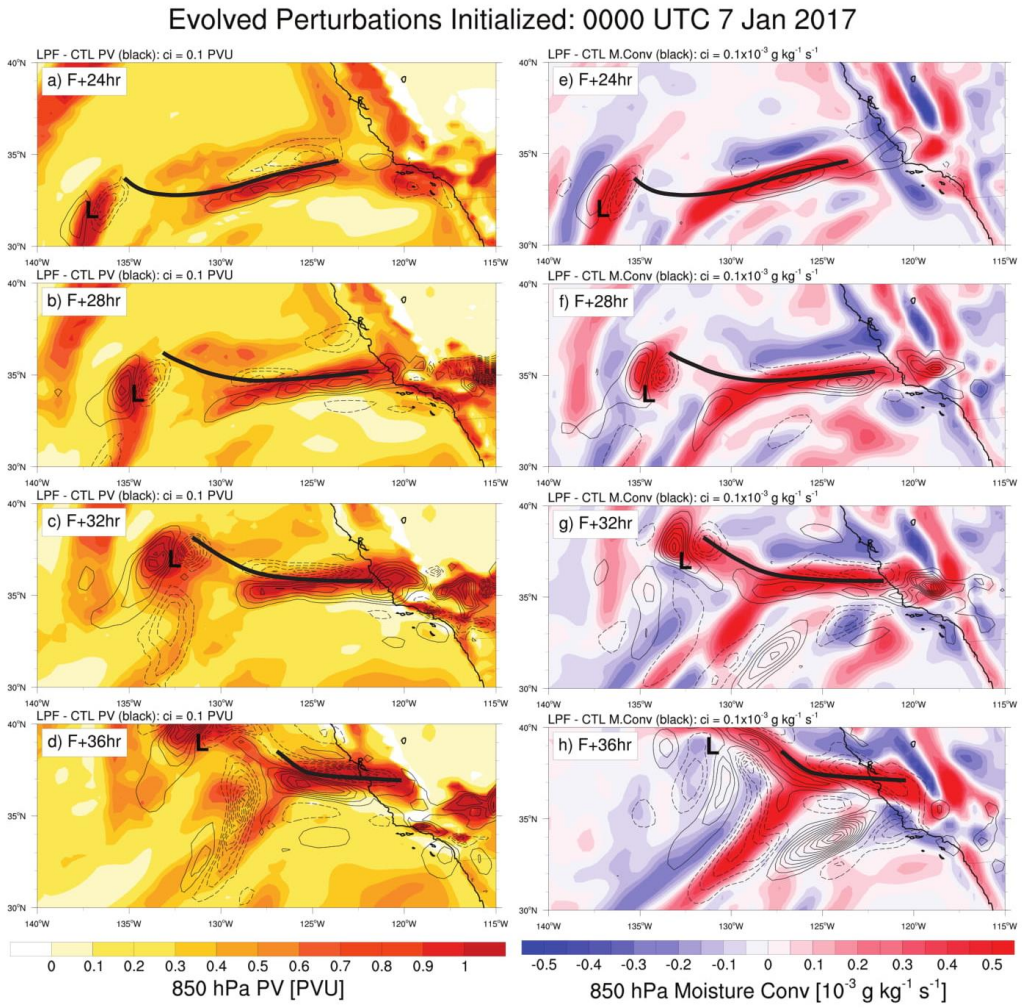

Figure 2.6: Plan view every 4 hours beginning from 24 h of the 850-hPa a)–d) PV (PVU; shaded) , and e)–h) moisture convergence (10-3 g kg-1 s-1; shaded; positive is converging). The LPF-CTL fields are shown in black with solid being positive and dashed being negative values. The approximate position of the low-pressure center of the developing secondary cyclone is labelled "L" and the warm front indicated by the thick black curved line. The position of a transect used in Figs. 2.7–2.9 is shown in c) in the thin black straight line.

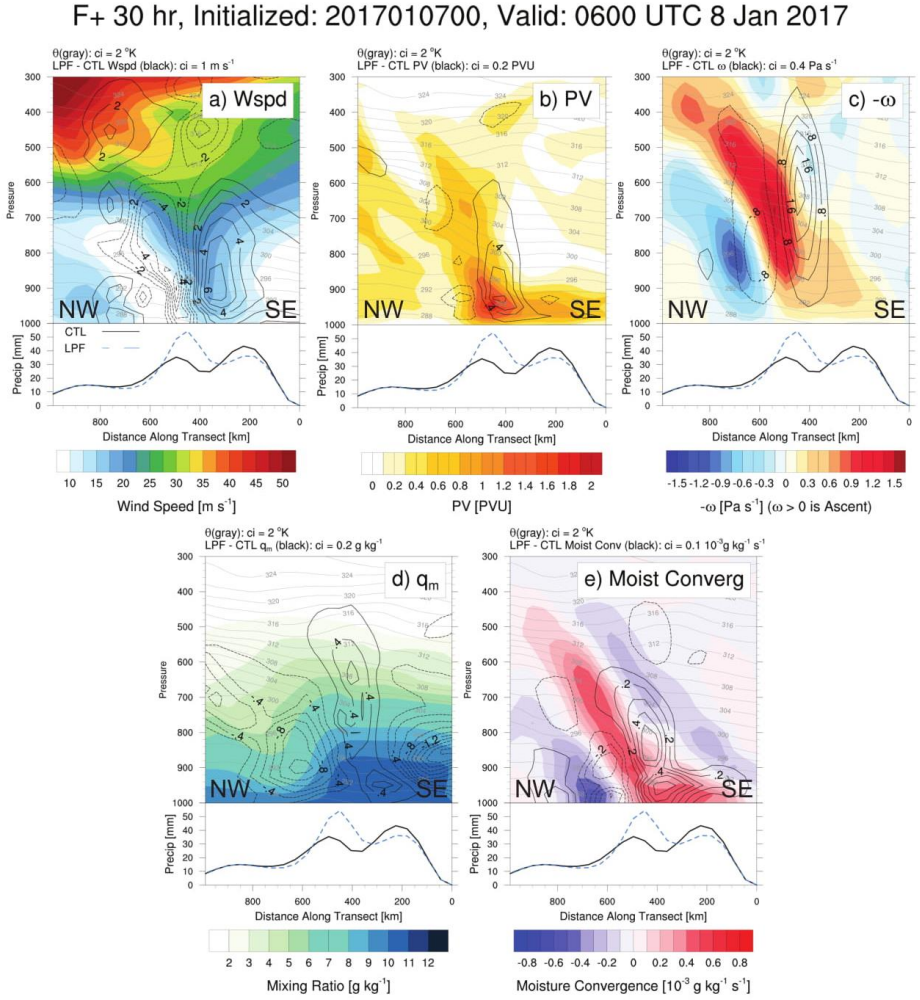

Figure 2.7: Cross sections at 30 h along the transect shown in Fig. 2.5c with "NW" being the northwest side and "SE" being the southeast side of a) wind speed (m s-1; shaded), b) PV (PVU; shaded), c) negative omega (Pa s-1; shaded), d) mixing ratio (g kg-1; shaded), and e) moisture convergence (10-3 g kg-1 s-1; shaded). The LPF-CTL fields are shown in black with solid being positive and dashed being negative values. The sub plot below each transect shows the accumulated precipitation for the CTL (solid black) and the LPF (dashed blue).

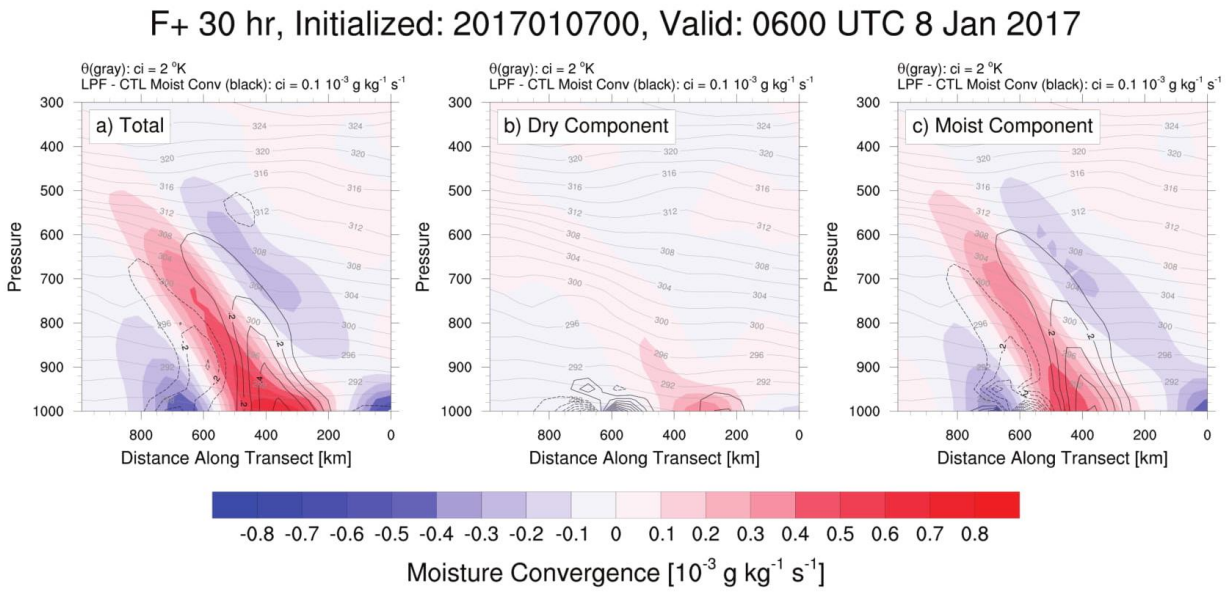

Figure 2.8: Cross sections at 30 h along the transect shown in Fig. 2.1i of the Sawyer-Eliassen derived moisture convergence (10-3 g kg-1 s-1; shaded) for the a) total, b) quasi-geostrophic (dry) component, and c) diabatic (moist) component. The LPF-CTL fields are shown in black with solid being positive and dashed being negative values.

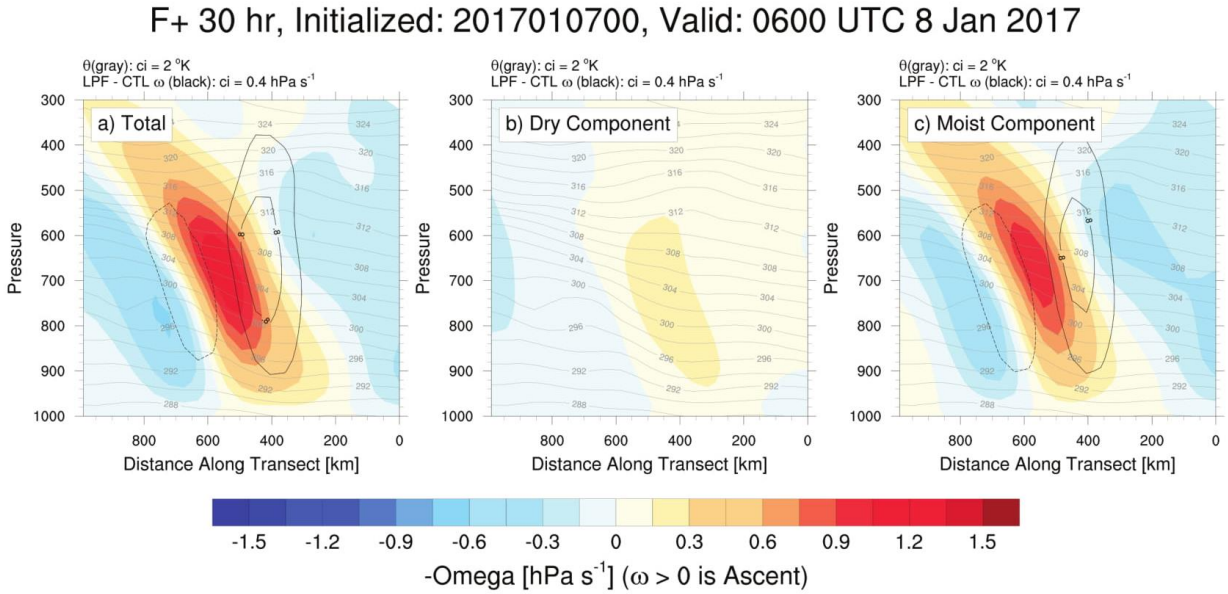

Figure 2.9: Cross sections at 30 h along the transect shown in Fig. 2.1i of the Sawyer-Eliassen derived vertical velocity (10-3 g kg-1 s-1; shaded) for the a) total, b) quasi-geostrophic (dry)

component, and c) diabatic (moist) component. The LPF-CTL fields are shown in black with solid being positive and dashed being negative values.

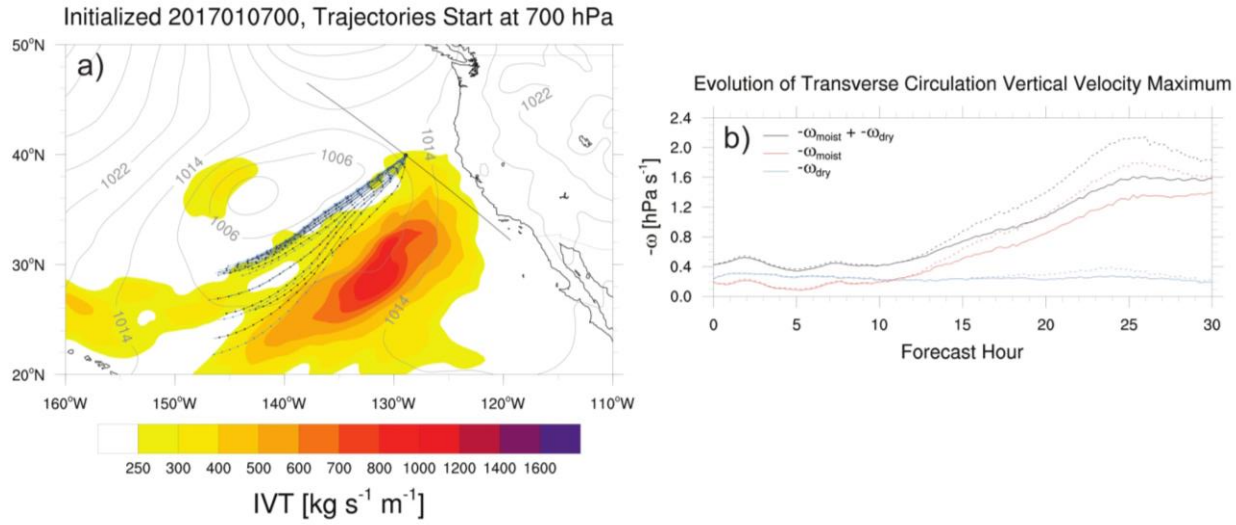

Figure 2.10: a) Plan-view of the initial time IVT (kg s-1 m-1; color fill) and SLP (contoured every 4 hPa; solid gray) with the backward trajectories of the CTL (black) and LPF (blue). The hourly locations of the air parcels are shown in the filled circle along each trajectory. The final time transect is shown as a reference in the solid black line. The trajectories are initialized at 700 hPa and are separated in time at one hour intervals starting from 24 h to 36 h. b) The average Sawyer-Eliassen -ω (hPa s-1) along the trajectories shown in a). The total value of -ω is in black with the moist component in red and the dry component in blue. The CTL is shown in the solid lines with the LPF in the dashed.

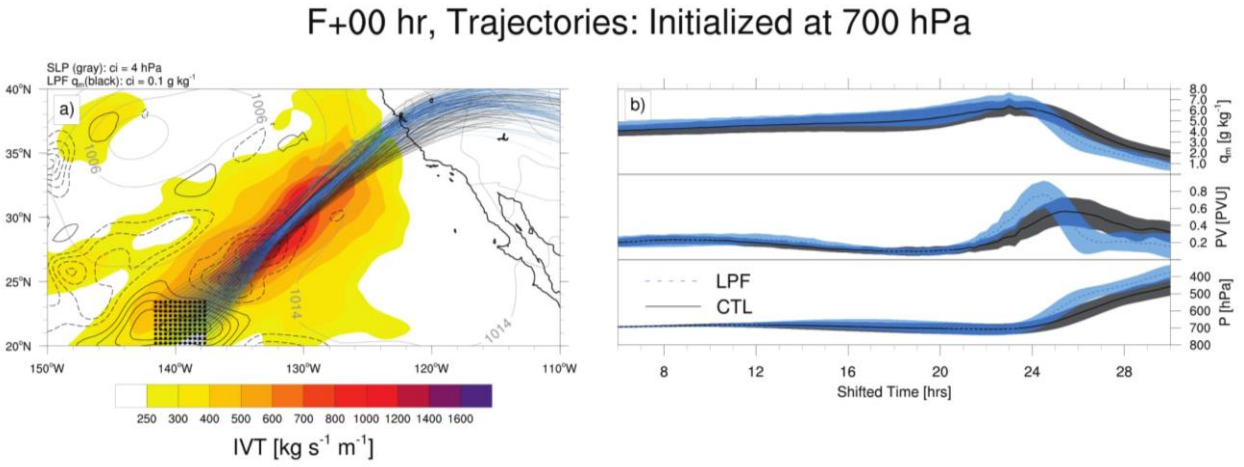

Figure 2.11: a) A plan-view of the initial time IVT (kg s-1 m-1; color fill), SLP (contoured every 4 hPa; solid gray), and initial condition LPF-CTL (black contours with solid being positive and dashed being negative values). Forward trajectories are shown for CTL (black) and LPF (blue) with the initialization points shown in black filled circles. b) From top to bottom: the mixing ratio (g kg-1), PV (PVU), and pressure (hPa) following the air parcel trajectories shown in a) for the

CTL (solid, black) and LPF (dashed, blue). The average of all trajectories is shown in bold with one standard deviation from the mean shown in the transparent color fill. The trajectories in b) are shifted in time to center each trajectory on the same feature (described in text).

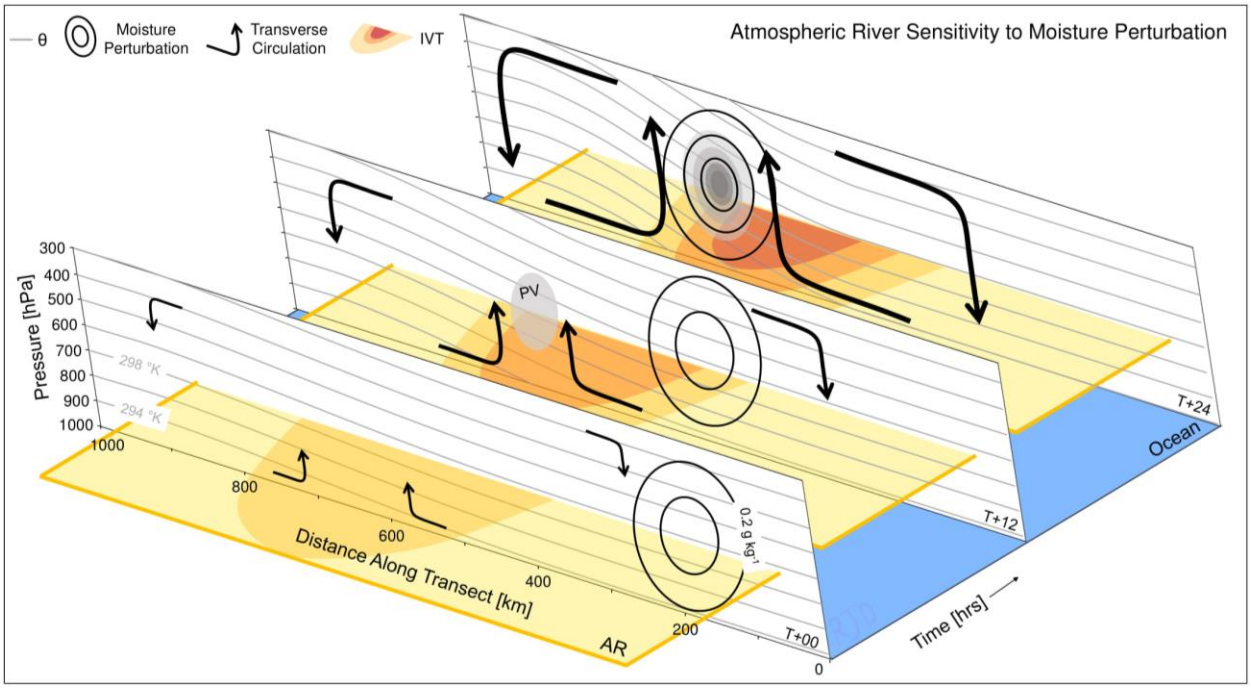

Figure 2.12: A pseudo-4D schematic illustrating the evolution of cross sections in an AR relative reference frame. The IVT values of the AR are shown in the yellow to red shading (small to large values respectively). The cross sections show potential temperature (gray contours), the LPF moisture perturbation (black contours), and the transverse circulation in plane of the cross section in the black arrows with the strength indicated by the length and arrow thickness.

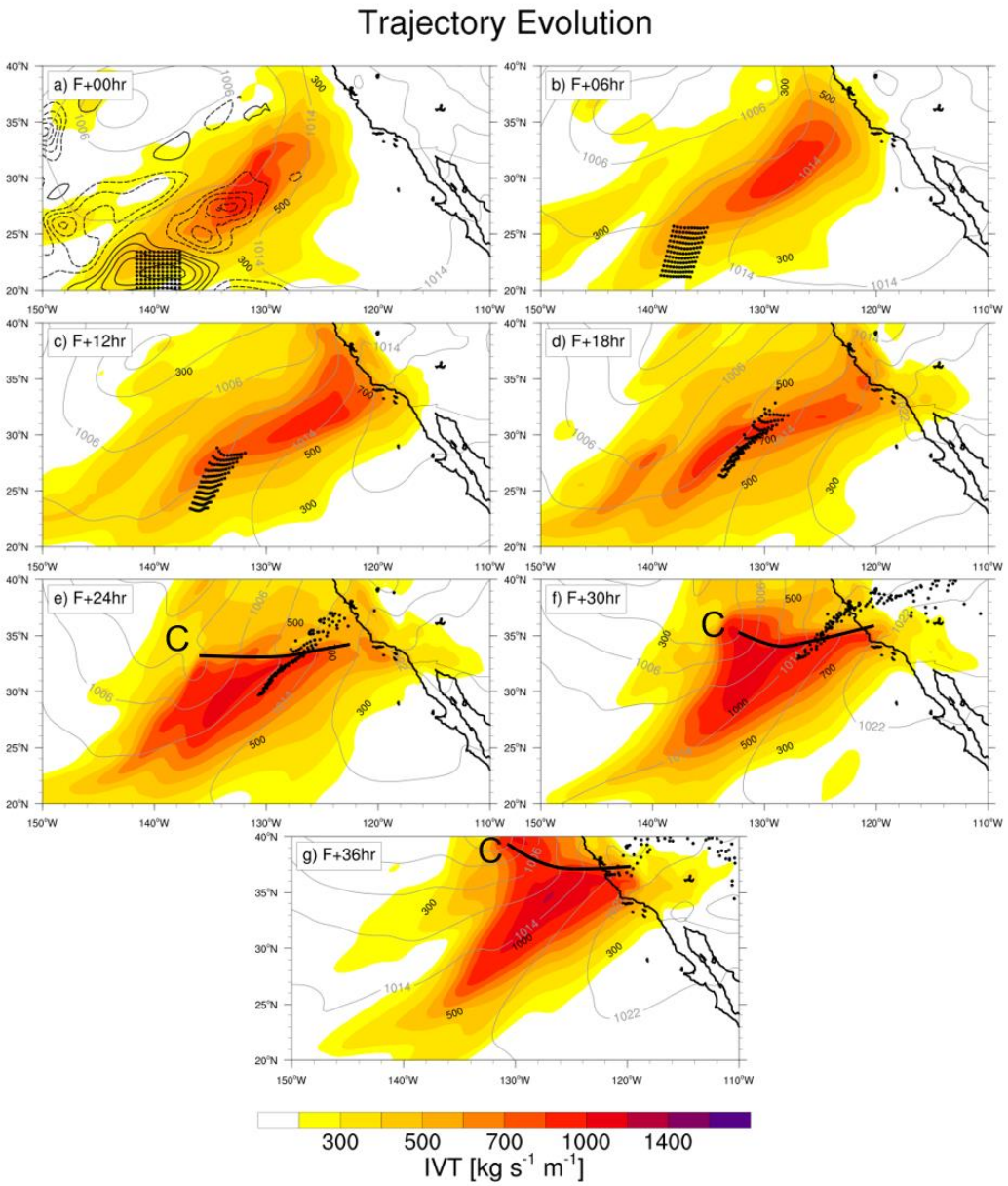

Supplemental 2.1: Plan-view maps every 6 hours of the LPF IVT (kg s^{-1} m^{-1}; shaded), the SLP (contour interval of 4 hPa; solid gray), and the air parcel positions at each time step. Panel (a) also has the initial condition LPF-CTL mixing ratio (black contours with solid being positive and dashed being negative values). Panels (e-f) show the position of the secondary cyclone with "C" and the position of the warm front with the thick solid black line.

Chapter 3: The Circulation Response of a Two-Dimensional Frontogenetic Model to Optimized Moisture Perturbations

Abstract

An analysis of the influence and sensitivity of moisture in an idealized two-dimensional moist semigeostrophic frontogenesis model is presented. A comparison between a dry (relative humidity, RH=0%) and moist (RH=80%) version of the model demonstrates that the impact of moisture is to increase frontogenesis, strengthen the transverse circulation (u_{ag}, w), generate a low-level potential-vorticity anomaly and develop a low-level jet. The idealized model is compared to a realistic case simulated with the full-physics three-dimensional Coupled Ocean-Atmospheric Mesoscale Prediction System (COAMPS) model establishing good agreement and thereby confirming that the idealized model retains the essential physical processes relevant for improving understanding of atmospheric rivers. Optimal perturbations of mixing ratio are calculated to quantify the circulation response of the model through the computation of singular vectors, which determines the fastest-growing modes of a linearized version of the idealized model. The vertical velocity is found to respond strongly to initial-condition mixing-ratio perturbations such that small changes in moisture lead to large changes in the ascent. The progression of physical processes responsible for this nonlinear growth is (in order): jet/front transverse circulation → moisture convergence ahead of the front → latent heating at mid-to-low elevations → reduction in static stability ahead of the front → strengthening of the transverse circulation, and the feedback cycle repeats. Together, these physical processes represent a pathway

by which small perturbations of moisture can strongly impact a forecast involving midlatitude frontogenesis.

3.1 Introduction

Improvement in Atmospheric River (AR) prediction is important to water-resource managers in many locations, perhaps most prominently California (CA) due to the state's large population and its dependence on the arrival, or lack thereof, of just a handful of precipitation events per year (Dettinger 2013; Ralph et al. 2013; Dettinger and Cayan 2014; Ralph 2017; Lamjiri et al. 2017, 2018). DeFlorio et al. (2018) performed an assessment of global landfalling ARs at a 2-day lead time finding that fewer than 75% of the European Centre for Medium-Range Weather Forecasts (ECMWF) ensemble members predicted AR landfall within 250 km of the actual location. This error provides motivation to work towards improving not only the magnitude of the water-vapor content in the AR, but also its position. Improvements in AR prediction can be subdivided into two broad categories, improving i) numerical-prediction systems, and ii) the data used to initialize the prediction systems; this study is concerned with category (ii).

Advances in research on initial conditions are being made through the AR Reconnaissance (AR-Recon) program which targets ARs using airborne instruments with emphasis on in situ dropsondes (Ralph et al. 2020). Choosing optimal aircraft tracks and dropsonde locations, however, is difficult because it is not always clear where additional observations are most likely to improve the analyses and subsequent forecasts. Initial-condition sensitivity analyses provide guidance towards designing the flight tracks by objectively determining where small errors can grow the largest for each storm individually.

Reynolds et al. (2019) used the Naval Research Laboratories (NRL) moist adjoint modeling system to evaluate the sensitivity of AR forecasts from January to February 2017. They found that

the accumulated precipitation forecasts were most sensitive to errors in and around the AR with the largest sensitivities being associated with the moisture field followed by temperature and winds. These results are consistent with the results of Doyle et al. (2014) and Doyle et al. (2019) for Atlantic extratropical cyclones (ECs) which, also using the NRL moist-adjoint tool, demonstrated that perturbations in regions having high moisture sensitivity lead to a coupling of the upper- and lower-level potential vorticity (PV) through a process known as PV unshielding. These studies were followed by Demirdjian et al. (2020a) which investigated other dynamical mechanisms leading to the growth of moisture perturbations using the NRL moist-adjoint system for a strong landfalling Pacific AR. The optimal perturbations in this case lead to a substantial growth in the low-level latent heating which i) amplified the diabatically driven low-level PV anomaly leading to the formation of a low-level jet (LLJ), and ii) intensified the jet/front transverse circulation leading to substantially stronger updrafts. These dynamical interpretations of the sensitivity fields are consistent with Cannon et al. (2020), who investigated the "importance of frontally forced precipitation on atmospheric heating tendencies." The adjoint tool provides a reliable methodology to quantitatively determine the forecast sensitivities, but it is left to the forecaster and researcher to interpret the dynamical origins and impacts of these sensitivity fields, especially if they are to be used to inform observing strategies and design flight-planning operations.

While sensitivity tools do provide guidance towards observing strategies, the impacts of the observations can only be quantified after the event. Stone et al. (2020) examined the impact of assimilating dropsonde observations into the Navy Global Environmental Model (NAVGEM) finding that the dropsondes had an overall relatively large beneficial impact with the per dropsonde impact being more than double that of the North American radiosonde network. Zheng et al. (2020)

documented the existing observational data gaps within ARs finding that, due to cloud cover, much of the satellite data measured for ARs is not used, which may increase the impacts of dropsondes consistent with the findings of Stone et al. (2020). The present work compliments these studies by focusing on the basic understanding of dynamical mechanisms that govern the growth of initial-state perturbations, which has an important influence on later-stage error growth.

The goals of the present study are to: i) investigate the dynamics responsible for moist-perturbation growth, and ii) quantify the relation between the moisture-perturbation amplitude and the strength of the circulation response. While other studies have looked at the dynamical mechanisms for perturbation growth associated with ARs, this study is unique because it uses an idealized two-dimensional model that simplifies the physical processes and makes the interpretation of the moisture-perturbation impacts to the system dynamics much more transparent. Furthermore, the method of optimal perturbations explored here makes it possible to isolate the impacts of the moisture perturbations. An increased understanding the dynamics associated with the growth of moist perturbations in a simplified system will lead to a more complete understanding of AR dynamics and forecast challenges.

3.2 Methods

a. Frontal Model

This study explores a variant of the idealized semi-geostrophic two-dimensional frontogenetic confluence model developed by Hoskins and Bretherton (1972) and used later in Hoskins (1975), Hoskins and West (1979), Hoskins (1982), Thorpe and Emanuel (1985), and Snyder et al. (1991). The model is based on the geostrophic coordinate transformation described by,

$$X = x + \frac{V}{f}, \;\; Z = z, \;\; T = t \tag{3.1}$$

where V is the geostrophic along-frontal wind component, and (x, z, t) are the Cartesian coordinates in physical space. The model was evolved forward in time by solving prognostic equations for the potential vorticity and mixing ratio given by,

$$\frac{Dq}{DT} = \frac{\zeta}{\rho}\frac{\partial S}{\partial Z}, \qquad \frac{Dr}{DT} = \frac{c_p}{L_v}\, S \tag{3.2}$$

where q is the potential vorticity, ζ is the relative vorticity, ρ is the density, r is the mixing ratio, c_p is the dry specific heat capacity, L_v is the latent heat of water vaporization, S is the latent heating rate, and $D/DT = \partial/\partial t \; + U_g \, \partial/\partial X \; + w \, \partial/\partial Z$. After the evolution of these fields, diagnostic quantities were calculated using the geopotential-height and Sawyer-Eliassen equations given respectively by,

$$\frac{\partial^2 \Phi}{\partial X^2} + \frac{\theta_0 f^3}{g\rho q}\frac{\partial^2 \Phi}{\partial Z^2} = f^2 \tag{3.3}$$

$$\rho \frac{\partial}{\partial Z}\left(\frac{1}{\rho}\frac{\partial \psi}{\partial Z}\right) + \frac{\partial}{\partial X}\left(\frac{\rho q g}{f^3 \theta_0}\frac{\partial \psi}{\partial X}\right) = -2Q - \frac{g\rho}{f^2 \theta_0}\frac{\partial S}{\partial X} \tag{3.4}$$

where ψ is the ageostrophic streamfunction, g is the gravitational acceleration, f is the Coriolis parameter, θ_0 is the base-state potential temperature, Q is the Q-vector, and Φ is the geopotential height. Finally, the remaining diagnostic quantities were calculated using the following relations,

$$(u_{ag}, w) = \left(\frac{1}{\rho}\frac{\partial \psi}{\partial Z}, -\frac{1}{\rho}\frac{\zeta}{f}\frac{\partial \psi}{\partial X}\right) \tag{3.5}$$

$$\zeta = f\left(1 - \frac{1}{f}\frac{\partial V}{\partial X}\right)^{-1} \tag{3.6}$$

$$V = \frac{1}{f}\frac{\partial \Phi}{\partial X} \tag{3.7}$$

$$S = \frac{1}{2}(q - q_e)\left(\frac{\rho}{\zeta}w + \left|\frac{\rho}{\zeta}w\right|\right) \tag{3.8}$$

$$q_e = q + \frac{L_v \zeta}{c_p \rho}\frac{\partial r}{\partial Z} \tag{3.9}$$

$$Q = \frac{\rho \alpha}{f}\frac{\partial V}{\partial Z} \tag{3.10}$$

where u_{ag} is the ageostrophic across-front wind component, w is the vertical wind component, and q_e is the equivalent potential vorticity. Thorpe and Emanuel (1985) observed that the latent heating (S) is dependent on the solution of ψ and accounted for this by rearranging the Sawyer-Eliassen (3.4) as follows,

$$\rho\frac{\partial}{\partial Z}\left(\frac{1}{\rho}\frac{\partial \psi}{\partial Z}\right) + \frac{\partial}{\partial X}\left(\frac{\rho \tilde{q} g}{f^3 \theta_0}\frac{\partial \psi}{\partial X}\right) = -2Q \tag{3.11}$$

where,

$$\tilde{q} = q_e, \quad \text{if} \quad w > 0,$$

$$\tilde{q} = q, \quad \text{if} \quad w \leq 0.$$

b. Numerical Setup

The model is on an A-grid extending from $-\pi L_R l^{-1}$ to $\pi L_R l^{-1}$ (approximately -2500 km to 2500 km) with 60 grid points (~80-km grid interval) in X and 0 to 10000 m with 45 grid points (~200-m grid interval) in Z. The prognostic equations were solved using a leapfrog integration

with a 15-minute time step and the Robert-Asselin filter (Robert 1966; Asselin 1972) applied to reduce numerical instabilities. The initialization parameters used are $\theta_0 = 292\,K$, $N^2 = 10^{-4}$ (Brunt-Vaisala Frequency), $\rho = 1.23\ kg\ m^{-3}$, $f = 10^{-4}$, $\alpha = 10^{-5}$, a prescribed pressure field of $p = 1000e^{-0.75\frac{Z}{H}}$, and constant initial potential vorticity with $q_0 = \frac{fN^2\theta_0}{g\rho} \cong 2.42\ x\ 10^{-1} PVU$.

The boundary conditions for the Sawyer-Eliassen partial differential (3.4) are simply $\psi = 0$ on all boundaries physically meaning that $w = 0$ on the top and bottom boundaries and $u_{ag} = 0$ on the left and right boundaries. The boundary conditions for the geopotential-height partial differential are,

$$\frac{d\phi}{dZ} = \frac{g}{\theta_0}\left(\Delta\theta_{bot}\sin(X_t l) + \frac{1}{2}X_t\Delta\theta_{bot}\right) \tag{3.12}$$

on the bottom,

$$\frac{d\phi}{dZ} = \frac{g}{\theta_0}\left(\Delta\theta_{top}\sin(X_t l) + \frac{1}{2}X_t\Delta\theta_{top}\right) + N^2\frac{Z}{H} \tag{3.13}$$

on the top,

$$\phi = \frac{gH}{\theta_0}\left(\frac{1}{2}\frac{X}{L_R}\left(\Delta\theta_{bot}\frac{Z}{H} + \frac{1}{2}\left(\Delta\theta_{top} - \Delta\theta_{bot}\right)\left(\frac{Z}{H}\right)^2\right)\right) + \frac{1}{2}N^2Z^2 \tag{3.14}$$

for the left boundary, and

$$\phi = \frac{gH}{\theta_0}\left(\frac{1}{2}\frac{X}{L_R}\left(\Delta\theta_{bot}\frac{Z}{H} + \frac{1}{2}\left(\Delta\theta_{top} - \Delta\theta_{bot}\right)\left(\frac{Z}{H}\right)^2\right)\right) + \frac{1}{2}N^2Z^2 \tag{3.15}$$

for the right boundary. Where $X_t = Xe^{\alpha T}/L_R$, $L_R = \frac{NH}{f}$ is the Rossby radius of deformation, $l = 1.1358$ is a horizontal scaling factor, $\Delta\theta_{bot} = 3\,K$ scaled the bottom-boundary potential-temperature gradient, $\Delta\theta_{top} = 6\,K$ scaled the top-boundary potential-temperature gradient, and

$H = 10\ km$. The method of successive over-relaxation was used to solve the Sawyer-Eliassen and geopotential height partial differential equations which were set to converge when the error values reached $\psi = 10^{-2} kg\ m^{-1} s^{-1}$ and $\phi = 10^{-8}\ m^2\ s^{-2}$, respectively. The model was also validated using the same boundary conditions presented in Thorpe and Emanuel (1985) which resulted in figures identical to theirs thereby providing confidence in our numerical routines.

c. Optimal Perturbation Method

A quantitative method was used to determine the optimal initial-condition perturbations of any field (water-vapor mixing ratio in this study) which maximizes a given response function (vertical velocity). The method determines the fastest-growing modes of a linearized version of the idealized model by computing a singular value decomposition. Following Moore and Kleeman (1997) and Peng et al. (2006), the full nonlinear model described in section 3.2b may be written as,

$$\boldsymbol{x_t} = \boldsymbol{M}(\boldsymbol{x_0}) \tag{3.16}$$

where $\boldsymbol{x_t}$ is the evolved state vector at time t, $\boldsymbol{M}$ is the nonlinear model, $\boldsymbol{x_0}$ is the initial-condition state vector, and bold font represents a vector. A perturbation at the initial time takes the form,

$$\boldsymbol{M}(\boldsymbol{x_0} + \boldsymbol{\Delta x_0}) = \boldsymbol{M}(\boldsymbol{x_0}) + \boldsymbol{L} * \boldsymbol{\Delta x_0} + O(\boldsymbol{\Delta x_0})^2 \tag{3.17}$$

where $\boldsymbol{\Delta x_0}$ is the perturbation at the initial time, $\boldsymbol{L}$ is the tangent linear model (TLM; also called the linear forward propagator), and $O(\boldsymbol{\Delta x_0})^2$ represents the higher-order terms of the model at time t. Assuming that the higher-order terms are negligible, the TLM may be written as,

$$\boldsymbol{L} = (\boldsymbol{X_t \Delta X_0^T})\left(\boldsymbol{\Delta X_0 \Delta X_0^T}\right)^{-1} \tag{3.18}$$

where the superscript “T” represents the transpose. The bold capital "$\boldsymbol{X}$" represents the ensemble matrix not to be confused with the coordinate "X" in section 3.2b. This formulation is necessary in

the case where the ensemble perturbation matrix $\mathbf{\Delta X_0}$ is not orthonormal so the inverse is not trivial. If it is not full rank, then its inverse is approximated by a pseudo-inverse. Equation (3.18) allows for the approximation of the linear tangent model with an ensemble set of runs without the requirement of finding it analytically, which can be difficult.

The ensemble was composed of a set of two-dimensional gaussian mixing ratio perturbations each given by,

$$\mathbf{\Delta x_0} = Ae^{-\frac{(X-X_0)^2}{2\sigma_X^2}+\frac{(Z-Z_0)^2}{2\sigma_Z^2}} \qquad (3.19)$$

where $A = 0.5\ g\ kg^{-1}, \sigma_X = 1000\ km,$ and $\sigma_Z = 1\ km$. The ensemble was formed by spacing each member by a two e-folding distance apart which amounts to spacing the perturbation center locations $X_0\ and\ Z_0$ approximately every 800 km and 800 m respectively. This required a 30-member ensemble be run to form the full set of $\mathbf{\Delta X_0}$, and $\mathbf{\Delta X_t}$. The estimated optimal perturbation vectors are restricted to being linear combinations of these perturbations.

Finally, the optimal perturbations were determined by calculating the fastest-growing linear modes of $\boldsymbol{L}$ which was done through a singular value decomposition given by,

$$\boldsymbol{L} = \boldsymbol{S\lambda W^T} \qquad (3.20)$$

where, $\boldsymbol{S}$ is a matrix containing the left singular vectors, $\boldsymbol{\lambda}$ is a diagonal matrix containing the singular values, and $\boldsymbol{W}$ is a matrix containing the right singular vectors. Descriptively, the right singular vector represents the optimal perturbations with the left singular vector being the evolved linear state of those perturbations and the singular values being the amplification factor of the perturbation compared with the (RH=80%) control run (see Diaconescu and Laprise 2012 for a thorough background of singular vectors).

d. COAMPS Model

The NRL Coupled Ocean-Atmospheric Mesoscale Prediction System (COAMPS; Hodur 1997; Doyle et al. 2014) model is used to compare the physical processes contained within the solution of the two-dimensional idealized model with a realistic case. COAMPS is a nonlinear, nonhydrostatic, compressible, terrain-following model run on a grid of 221 x 161 grid with a grid spacing of 40 km on a Lambert conformal grid with 70 vertical levels. For a full description of the parameterizations and physics packages, see Doyle et al. (2012, 2019). For a detailed description of the specific run used in this study see Demirdjian et al. (2020a).

3.3 Results

a. The Moist Control Simulation

The control simulation was initialized with a relative humidity (RH) of 80% everywhere resulting in a mixing ratio maximum of 15.4 g kg^{-1} and a minimum of 1.1 g kg^{-1}. The evolution of the control simulation is shown in Fig. 3.1 from forecast hour 6 and ending at hour 42. The model was initialized with a geostrophically balanced upper-level jet (Fig. 3.1a), a constant potential vorticity field (Fig. 3.1b), a weak transverse circulation (Fig. 3.1c) which is forced entirely by the quasi-geostrophic Q-vector at early times, and a moisture field with greater content weighted towards the warm sector (Fig. 3.1d). All fields were transformed from geostrophic to Cartesian coordinates using $x = X - V/f$.

Twelve hours later at 18 h (Figure 3.1e-h), the baroclinicity has strengthened, the along-front geostrophic wind has intensified, the vertical circulation has strengthened substantially, the moisture begins to converge towards the center, and a weak but visible surface-PV anomaly has developed below the maximum in latent heating. The evolution up until this time is driven

primarily by the “dry” prescribed confluence rate since too little time has passed for moist processes to act strongly.

Another 12 hours later at 30 h (Figures 1i-l), the latent heating has further intensified causing the strengthening of the surface-PV anomaly. A cyclonic circulation has formed centered at x = 400 km in response to the PV anomaly as can be seen by the development of the low-level jet (LLJ) on the south (right) side of the PV and a weakening of the wind of the north (left) side. The sustained latent heating also leads to a weakening of the static stability thereby allowing for the vertical velocity to continue to intensify. By this time, the moist processes have grown to sufficient strength to begin to affect the evolution of the circulation in a noticeable way (described in more detail in section 3.3b).

At the final time 42 h (Figs. 3.1m-p), a continued progression of the same processes is observed leading to a strong LLJ with peak amplitude of ~20 m s^{-1} at the surface, a large surface PV anomaly having amplitude of 1 PVU, a strong latent heating rate ahead of the front having amplitude of 8 K day^{-1}, a convergence of moisture along the frontal zone, and a sharp narrow updraft ahead of the front having amplitude of about 3 cm s^{-1}. The control simulation demonstrates that the idealized model can reproduce the physical processes consistent with the basic meteorological understanding of frontogenesis.

b. Dry vs. Moist Run

An analysis of a dry versus a moist version of the model was performed to isolate the impacts of moisture on the solution. The dry version set RH = 0% while the moist version set RH = 80% everywhere in the model domain (same run as in Fig. 3.1). The impact of moisture is clearly shown in Fig. 3.2 for the along-front geostrophic wind at 42 h. The solution in the moist run (Fig. 3.2b) results in a stronger frontal temperature gradient and the development of a LLJ. The dry case

develops only a weak LLJ consistent with the hypothesis that the LLJ is a direct response of the surface PV anomaly (Lackmann 2002) which has much stronger development in the moist case (Fig. 3.1). Further support of this hypothesis is found in the fact that the dipole in the along-front geostrophic-wind differences (Fig. 3.2a) is centered exactly on the surface-PV anomaly seen in Fig. 3.1n.

Similarly, a comparison of the across-front ageostrophic wind for the dry and moist cases is shown in Fig. 3.3. The moist run exhibits noticeably stronger ageostrophic wind magnitudes as well as a strong x-gradient of the ageostrophic wind ($\partial u_{ag}/\partial x$). Perhaps the greatest difference between the two runs is seen in the vertical velocity field (Fig. 3.4); the moist run exhibits an updraft which is much narrower and about 3x as strong as the dry runs. This is a direct result of the strong latent heating which acts through the moisture term of (3.4). The role of latent heating within the Sawyer-Eliassen transverse circulation is to reduce static stability which reduces the resistance to vertical motion thereby allowing for a more vigorous updraft to develop and a stronger across-front wind component. In turn, the more vigorous transverse circulation leads to stronger latent heating (3.8) and a simple feedback process is established which allows the system to intensify quickly.

c. Comparison with COAMPS

It is important that the physical processes contained within this idealized two-dimensional model have realistic solutions so that concepts learned here may be applied to real cases with greater complexities. A comparison between the two-dimensional idealized run with the full physics COAMPS model was performed for validation purposes. The case selected for the validation is the same one used in Demirdjian et al. (2020a) because it i) has strong frontogenesis,

ii) is a strong AR case, and iii) was readily available at the high temporal output (15 minute) required for the trajectory analysis described below.

The two-dimensional idealized model implicitly assumes a transect that follows the mean flow of the system. To facilitate a fair comparison between the two models, a Lagrangian air-parcel trajectory analysis was performed on the COAMPS model to follow a transect along as it is advected by the mean flow. Backward trajectories were calculated using the same algorithm used in Demirdjian et al. (2020a) starting from a point along the final time (42 h) cold front (Fig. 3.5b). The sensitivity of the backward trajectory to the starting location was investigated by shifting the starting location up and down by 2 degrees along the transect with the resulting changes in trajectory and subsequent figures showing little change. The backward trajectory initialized at the center of the transect in Fig. 3.5b leads to the transect center shown in Fig. 3.5a. Feature tracking between Fig. 3.5a and Fig. 3.5b of the integrated vapor transport (IVT) object from 42 h to 0 h is misleading because it appears as though the transect crosses the IVT object maximum at 42 h but not at 0 h. However, a closer examination of the feature tracking (Supplemental 3.1) demonstrates that the trajectory algorithm does indeed track the IVT maximum and that the reason for this misleading tracking is due to the development of a secondary cyclone and reinvigoration of the AR sometime between 0 h and 42 h.

The COAMPS Lagrangian transects are shown in Fig. 3.6 along with the moist (RH = 80%) control run of the two-dimensional idealized model for comparison. At time 0 h, the COAMPS model has a zone of weak baroclinicity accompanied by a weak upper-level jet (Fig. 3.5a, 3.6a). Similarly, at time 0 h the idealized model has approximately the same magnitude baroclinicity but with a moderately stronger upper-level jet (Fig. 3.6b). By time 42 h, the COAMPS run (Fig. 3.5b, 3.6c) has undergone mid-level frontogenesis (centered on ~6 km elevation) leading to a substantial

increase in the upper-level jet strength. Furthermore, a low-level cyclonic circulation is seen to develop with an LLJ on the southeast (right) side and a reduction in the wind speed on the northwest (left) side centered at about x = 2200 km. Similarly, by 42 h the idealized simulation (Fig. 3.6d) has undergone frontogenesis from top to bottom which has led to the intensification of the upper-level jet, though not as strongly as in the COAMPS jet. A low-level cyclonic circulation is also observed to develop causing the formation of an LLJ of similar magnitude and relative location (relative to the front and upper level jet) as in the COAMPS run. In both simulations, this low-level cyclonic development is a response to the development of the low-level PV anomaly (Supplemental 3.2) as discussed in section 3.3a,b. Finally, the mid-level frontogenesis (centered on ~6 km elevation) is observed to be of similar strength between the two simulations as witnessed in Fig. 3.6c,d. The discrepancy in surface frontogenesis between the two models is explained by the fact that the idealized model does not have a boundary layer while the COAMPS model is equipped with complex boundary-layer physics which are not represented in the idealized model.

The good agreement between the idealized model with the full-physics nonhydrostatic COAMPS model suggests that the simplified physics contained within the idealized model is sufficient for the study of the basic frontogenetical processes within ARs.

d. Optimal Perturbations

The method of objectively determining the optimal perturbations described in section 3.2c was used by solving for the initial-condition mixing-ratio perturbation (optimal perturbation) which maximizes the final-time vertical velocity (i.e. the response function). In terms of the singular-vector terminology (section 3.2c), the mixing ratio is the right singular vector and vertical velocity is the left singular vector as shown in Fig. 3.7 on the full model domain which is larger than that shown in Figs. 3.1-3.4,3.6. Physically speaking, Fig. 3.7 describes a linearized version of

the two-dimensional idealized nonlinear model in which mixing-ratio perturbations at 0 h of the form shown in Fig. 3.7b are mapped onto the evolved vertical velocity perturbations at 42 h shown in Fig. 3.7a. It is important to emphasize that "perturbation" is used here as meaning the difference of the perturbed run from the moist control run used in sections 3.3a-c. In this context, positive values of any of the difference fields shown in the following figures indicate that the perturbed-run field is greater than that in the control. Additionally, the second leading singular vector was used because the primary leading SV mode quickly created strong negative PV, invalidating the model assumptions and creating numerical instabilities. The second SV does not lead to as large of a negative PV signal and thereby allows for longer run times. Despite this, it is justified to use the second leading SV because the goal of the study is to determine *if* the model is sensitive to small amplitude moisture perturbations and not necessarily what form the distributions take.

The optimal perturbation distribution is used to create an ensemble of perturbation runs by scaling the optimal perturbation from 0x to 15x every 1x with the 1x, 8x, and 15x scaling shown in Fig. 3.8. The purpose of this ensemble is to quantify the idealized model's circulation response to the perturbation amplitude. The moisture evolution out to 36 h of the ensemble members is shown in Fig. 3.9. This end time is chosen because it represents the common time at which none of the members have become numerically unstable due to the generation of negative PV and also provides a sufficient amount of time for the perturbations to grow and affect the model. Only final times are shown in Fig. 3.9 because prior to 24 h each of the perturbation runs look identical (not shown) highlighting the fact that the initial-condition perturbations only made small changes to the basic state which later became amplified. Figure 3.9 demonstrates that the optimal moisture perturbation evolves to increase the amplitude of the vertical gradient of mixing ratio $(\partial r/\partial z)$ ahead of the front. Latent heating is directly related to the strength of $\partial r/\partial z$ as seen in (3.8) and

this relationship is clearly observed in Fig. 3.10. Since the Sawyer-Eliassen transverse circulation is forced by the latent heating, increased latent heating drives an increase in ascent rate by reducing the static stability (Fig. 3.11). Additionally, the vertical velocity of the non-linear model (Fig. 3.11) correlates well having $r = 0.6$ with that of the linearized model (Fig. 3.7a; note different domain size) indicating that the linearity assumption made in the optimal perturbation analysis is valid.

Another by-product of the ensemble members' latent-heating increase is the intensification of the surface-PV anomaly (Fig. 3.10). Since the PV anomaly is stronger, the along-front geostrophic-wind response is also stronger (Fig. 3.12) leading to an intensification of the LLJ in the perturbation runs compared with the control. Interestingly, a negative along-front geostrophic wind field is observed in the strongest ensemble member centered on x = 700 km (Fig. 3.12). The latter feature in the wind field forms as a result of the generation of a negative surface-PV anomaly seen to be centered on x = 500 km which has the opposite circulation response (positive V_g on the left and negative on the right) as the positive PV anomaly. Importantly, the optimal moist perturbations maximize the vertical velocity and an intensification of the along-front circulation through a stronger LLJ as a byproduct.

The question arises as to whether the circulation responds linearly or nonlinearly to the increasing amplitude of the optimal moisture perturbations within the ensemble. The maximum in perturbation vertical velocity at 36 h is plotted as a function of the domain-maximum mixing-ratio perturbation at 0 h demonstrating the clear nonlinear relationship (in Fig. 3.13a). Doyle et al. (2014) states that the dropsonde uncertainty range due to measurement error for relatively humidity is 10% which converted to mixing ratio is 1.5 g kg^{-1} at 925 hPa. This indicates that the perturbation sizes used here are within a realistic forecast uncertainty range. This nonlinear response to the moisture perturbations is also seen in Supplemental 3.3 where a linear regression was used to

remove the linear component from the total with the residual being the nonlinear component. Given a change of about 10% to the initial condition mixing ratio, the largest increase in the vertical velocity for the optimally perturbed runs is about 200% relative to the moist (RH=80%) control run and about 600% relative to the dry (RH=0%) control run. Finally, the change in the amount of domain-total latent energy due to the optimal perturbations is investigated in Fig. 3.13b. Overall, the change in the latent energy is actually decreasing by a small amount < 0.1% demonstrating that the rearrangement of initial-condition energy can have a large impact on the final-time forecast.

3.4 Conclusions and Discussion

This study is focused on the understanding of how relatively small moisture perturbations can affect the evolution of a frontogenetic system simulated using an idealized two-dimensional semi-geostrophic model following Hoskins and Bretherton (1972), Hoskins (1975), Hoskins and West (1979), Hoskins (1982), Thorpe and Emanuel (1985), and Snyder et al. (1991). The effects of moisture were first investigated through a comparison between a dry (RH=0%) and moist (RH=80%) run where the moist frontogenesis and resulting circulation was found to be substantially stronger, even producing a low-level jet (LLJ) consistent with other studies (Thorpe and Emanuel 1985; Lackmann 2002). The idealized model was then compared against the full physics three-dimensional Coupled Ocean-Atmospheric Mesoscale Prediction System (COAMPS) model in which good agreement between the two demonstrated that the idealized model retains the essential physics for the purposes of this study. Optimal perturbations of moisture were calculated using the singular value decomposition (SVD) method and a 16-member ensemble was created by scaling the perturbations from an amplitude of 0 g kg^{-1} to about 1.7 g kg^{-1}. The vertical velocity response at 36 h was found to depend nonlinearly on the mixing-ratio-perturbation

amplitude at 0 h demonstrating a pathway by which small moisture perturbations can substantially impact a forecast.

A schematic representation of the important physical processes contained within the moist frontogenetic run is shown in Fig. 3.14. The evolution of the transverse circulation leads to moisture convergence centered at the baroclinic zone. The moisture convergence is followed by ascent and latent heating at a low-to-mid levels and above the surface. The potential temperature adjusts to the latent heating by decreasing $\partial\theta/\partial Z$ and thereby the static stability. The reduced static stability allows for a strengthening of the transverse circulation and the entire cycle just described is repeated with greater intensity. The optimal perturbation method appears to have targeted this feedback process allowing for the moisture perturbations to have maximum impact on the vertical velocity. This was achieved in a twofold manner: i) by creating a distribution which increases the vertical derivative of mixing ratio (and thereby latent heating from eq. 8), and ii) by positioning the distribution on the warm side of the front whereby the background confluence could advect it towards the ascent region and contribute towards the latent heating rate. Another important but incidental circulation response to the optimal moisture perturbations was in the intensification of the LLJ through the strengthening of the surface-PV anomaly.

The physical processes outlined in Fig. 3.14 demonstrates that the frontogenetic circulation can respond to moisture perturbations by increasing both the vertical and horizontal along-front circulation. Following Alpert (1986) and Lu et al. (2018) the precipitation can be decomposed into a dynamic component (synoptic and mesoscale ascent) and an orographic component (water vapor transport interacting with orography). Using this framework, the idealized model's vertical velocity represents the dynamic component and the horizontal along-front geostrophic wind represents the orographic component. The precipitation of a frontal system is thereby highly

sensitive to initial-condition moisture content because it can simultaneously affect both components of precipitation consistent with other studies (Cannon et al. 2018; Demirdjian et al. 2020a). This physical argument of a strong precipitation-forecast dependence on the initial-condition moisture content highlights the importance of proper observing-system operational planning in regions like the Pacific which otherwise would have vast areas without any vertically resolved moisture data. Additionally, the nonlinear relationship between vertical velocity and initial-condition moisture content suggests that even if the orographic precipitation component were to be ignored, the dynamic component of precipitation would alone be sensitive to moisture content.

When interpreting the results of this study, it is important to keep the model's limitations in mind. The first consideration is that the model is statically stable which actually serves to bolster the conclusions formed here since a statically stable model is unable to trigger free convection. In a more sophisticated full-physics model, moisture perturbations can trigger buoyancy instabilities which would drive free convection and potentially a rapid departure from any non-convective cases. This suggests that the circulation response to moisture sensitivities shown in Fig. 3.13 are expected to be an underrepresentation of the circulation response to moisture. The next consideration is that the idealized model neglects both a boundary layer which causes vertical mixing in the lower levels of moisture and sensible heat. The surface front is thereby stronger than expected as seen in observational studies of fronts (Browning and Pardoe 1973; Thorpe and Clough 1991; Wakimoto and Murphey 2008, Demirdjian et al. 2020b). Finally, the last consideration is that the idealized model also neglects frictional drag at the surface which will reduce the horizontal wind components and thereby the strength of the LLJ. The inclusion of the surface drag will also serve to elevate the LLJ maximum above the surface. Despite these

simplifications, the idealized model provides a remarkably high-fidelity representation of the mesoscale processes during frontogenesis.

Acknowledgements

Chapter 3, in part, has been submitted for publication of the material as it may appear in the Journal for Atmospheric Science. Demirdjian, R., R. Rotunno, B. Cornuelle, J.D. Doyle, C.A. Reynolds, 2020: The Circulation Response of a Two-Dimensional Frontogenetic Model to Optimized Moisture Perturbations. The dissertation/thesis author was the primary investigator and author of this paper.

Figures

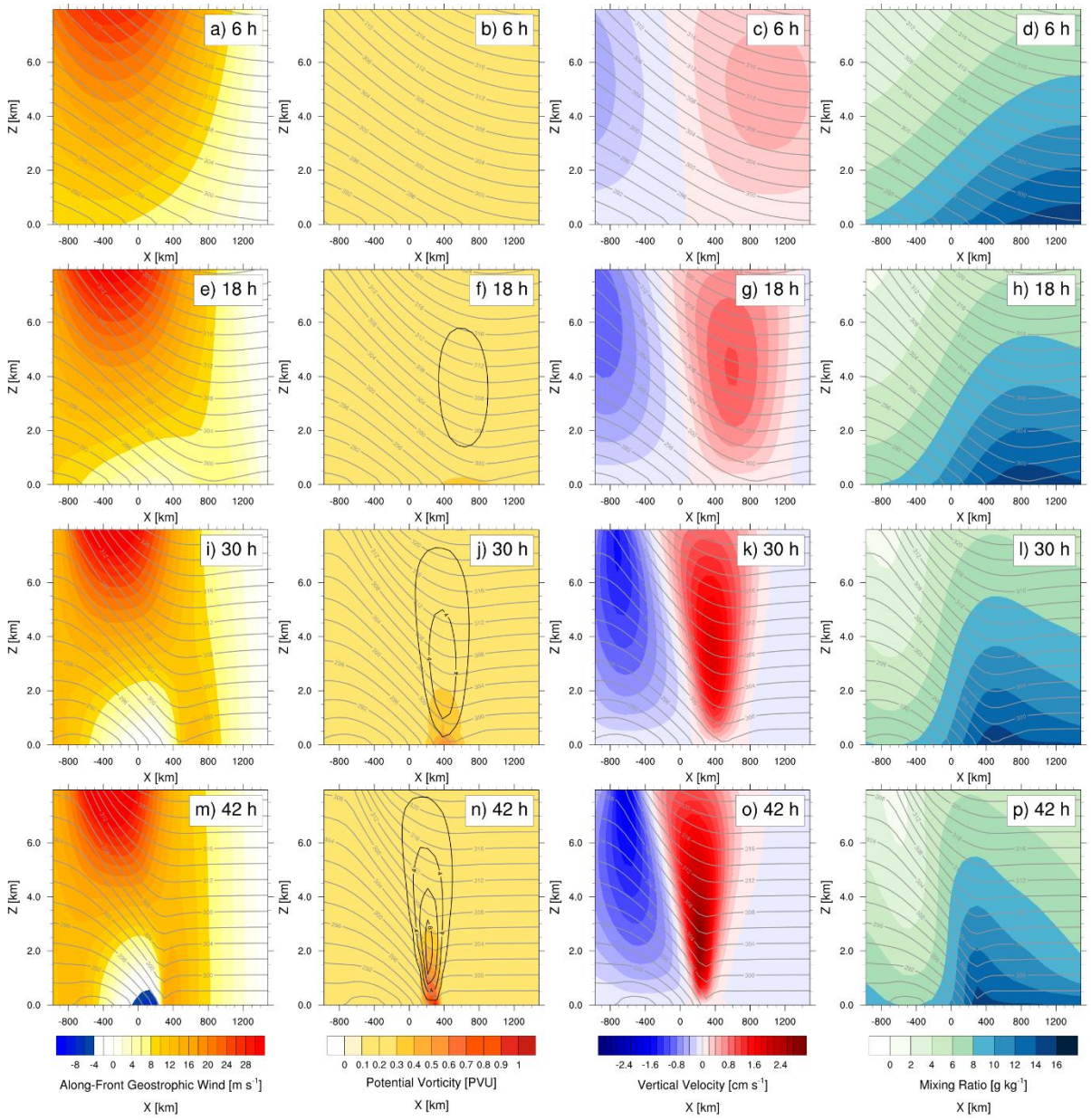

Figure 3.1: The control simulation from forecast hour 6 to 42 hours every 12 hours for a,e,i,m) the along-front geostrophic wind (color fill; m s^{-1}), b,f,j,n) the potential vorticity (color fill; PVU) and latent heating rate (black contours; ci = 2 K day^{-1}), c,g,k,o) vertical velocity (color fill; cm s^{-1}), and d,h,l,p) water vapor mixing ratio (color fill; g kg^{-1}). All plots include the potential temperature (grey contours; ci = 2 K).

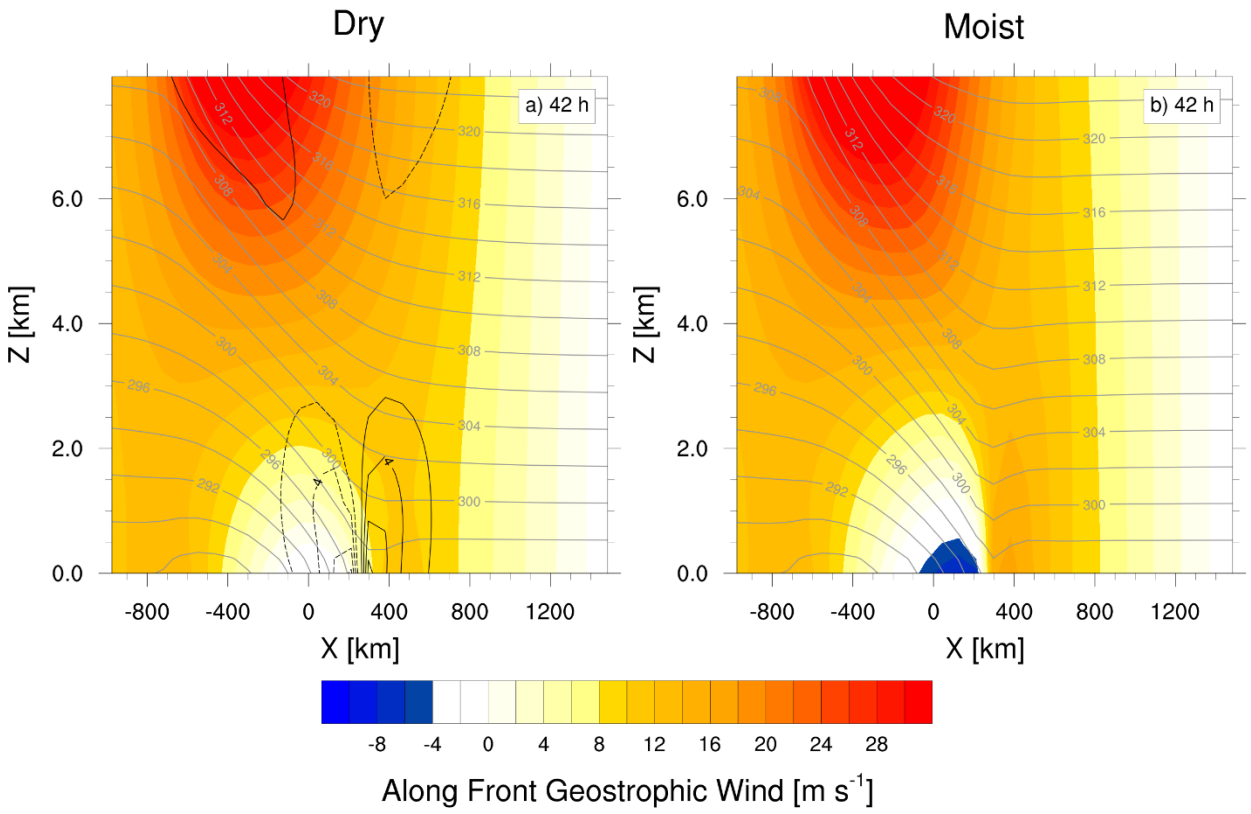

Figure 3.2: A comparison at forecast time 42 h for a) the dry (rh = 0%) and b) moist (rh = 80%) versions the model. Both plots have the along-front geostrophic wind (color fill; m s^{-1}), and potential temperature (grey contour; ci = 2 K). (a) also contains the moist minus dry along-front geostrophic wind (black; ci = 2 m s^{-1}).

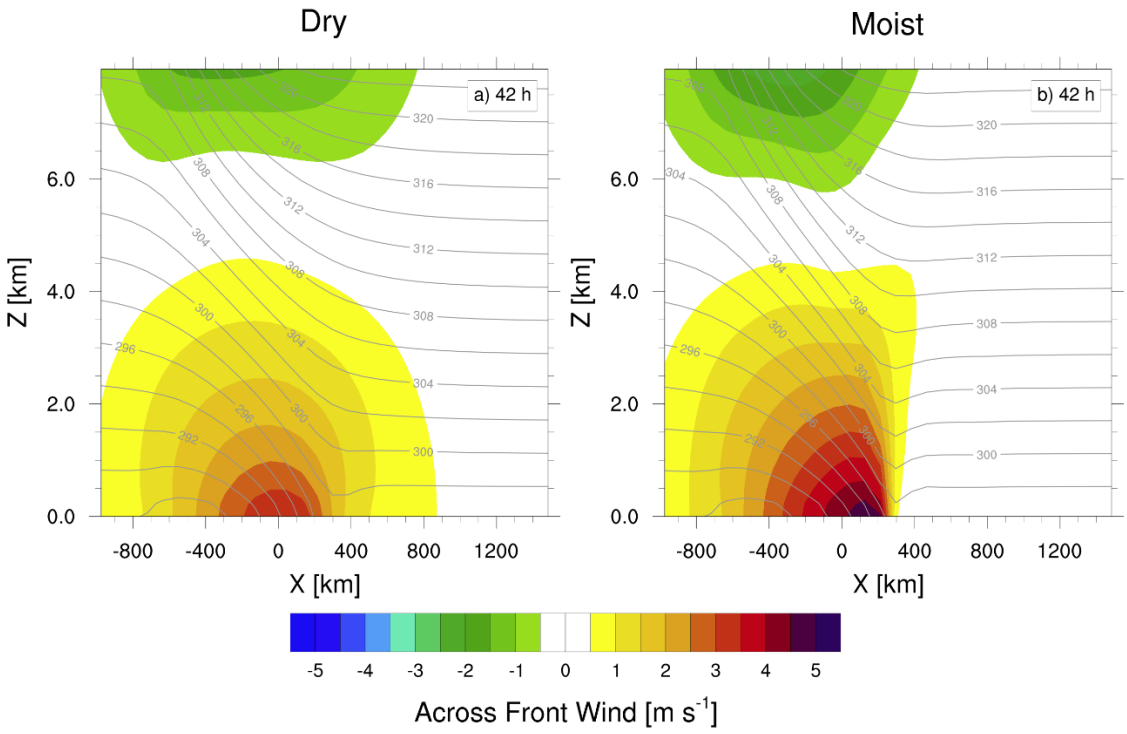

Figure 3.3: Same as Fig. 3.2 except for the across-front ageostrophic wind.

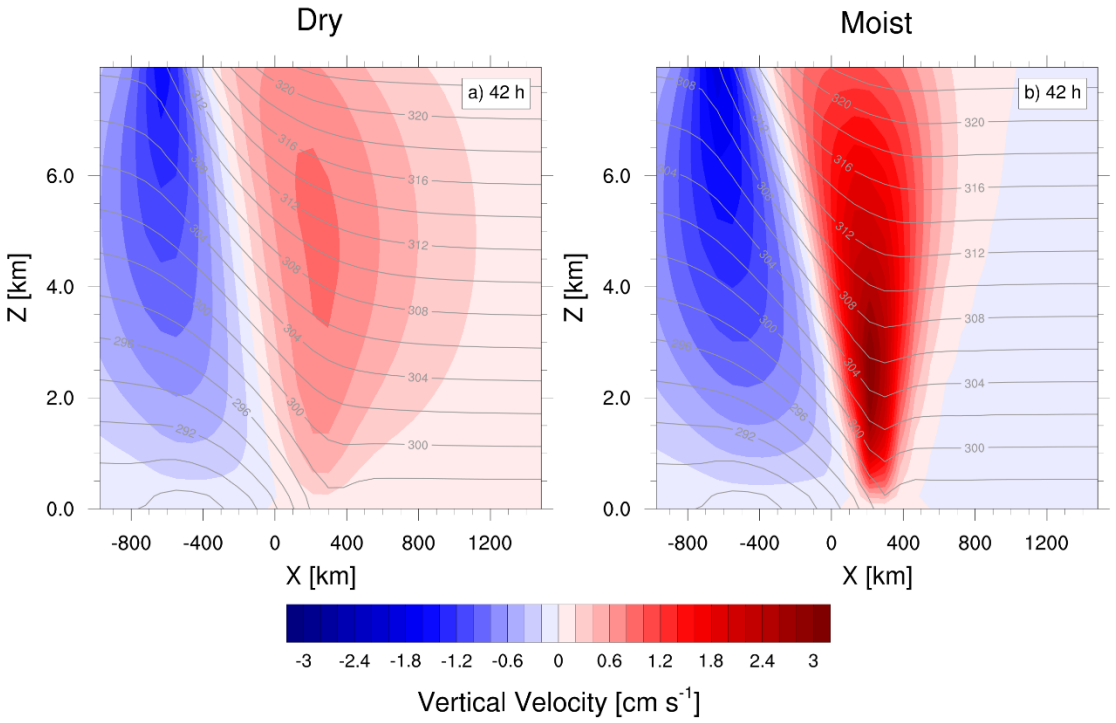

Figure 3.4: Same as Fig. 3.2 except for the vertical velocity.

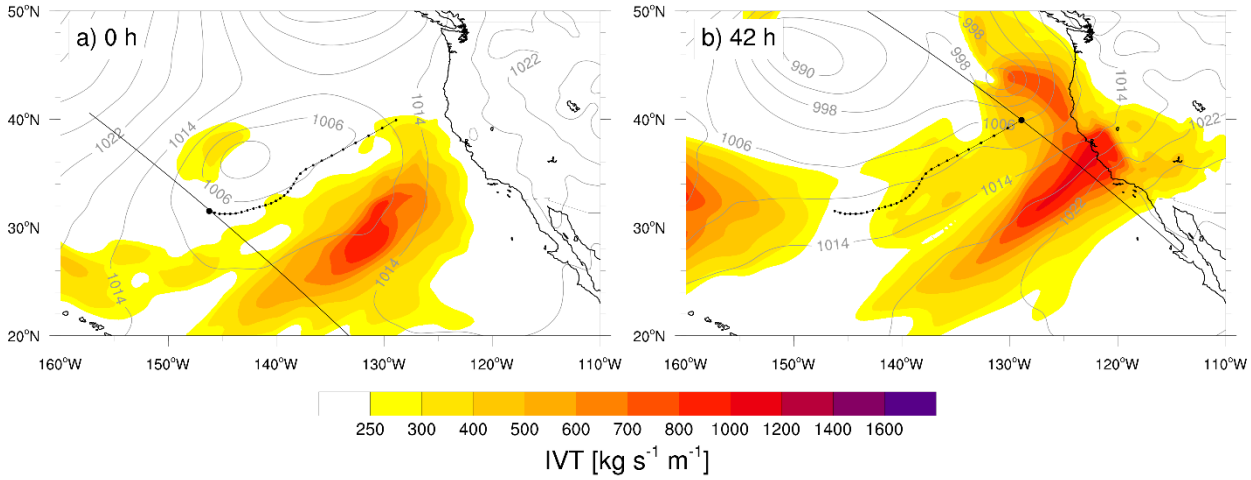

Figure 3.5: A COAMPS plan view of the sea -level pressure (SLP; black contours; ci = 4 hPa) and integrated vapor transport (IVT; color fill; kg m s^{-1}) at time a) 0-h, and b) 42-h. The black dotted lines are the same in each plot and are the backward trajectories with a dot every 3 hours. The straight diagonal black lines are the transects used in Fig. 3.6.

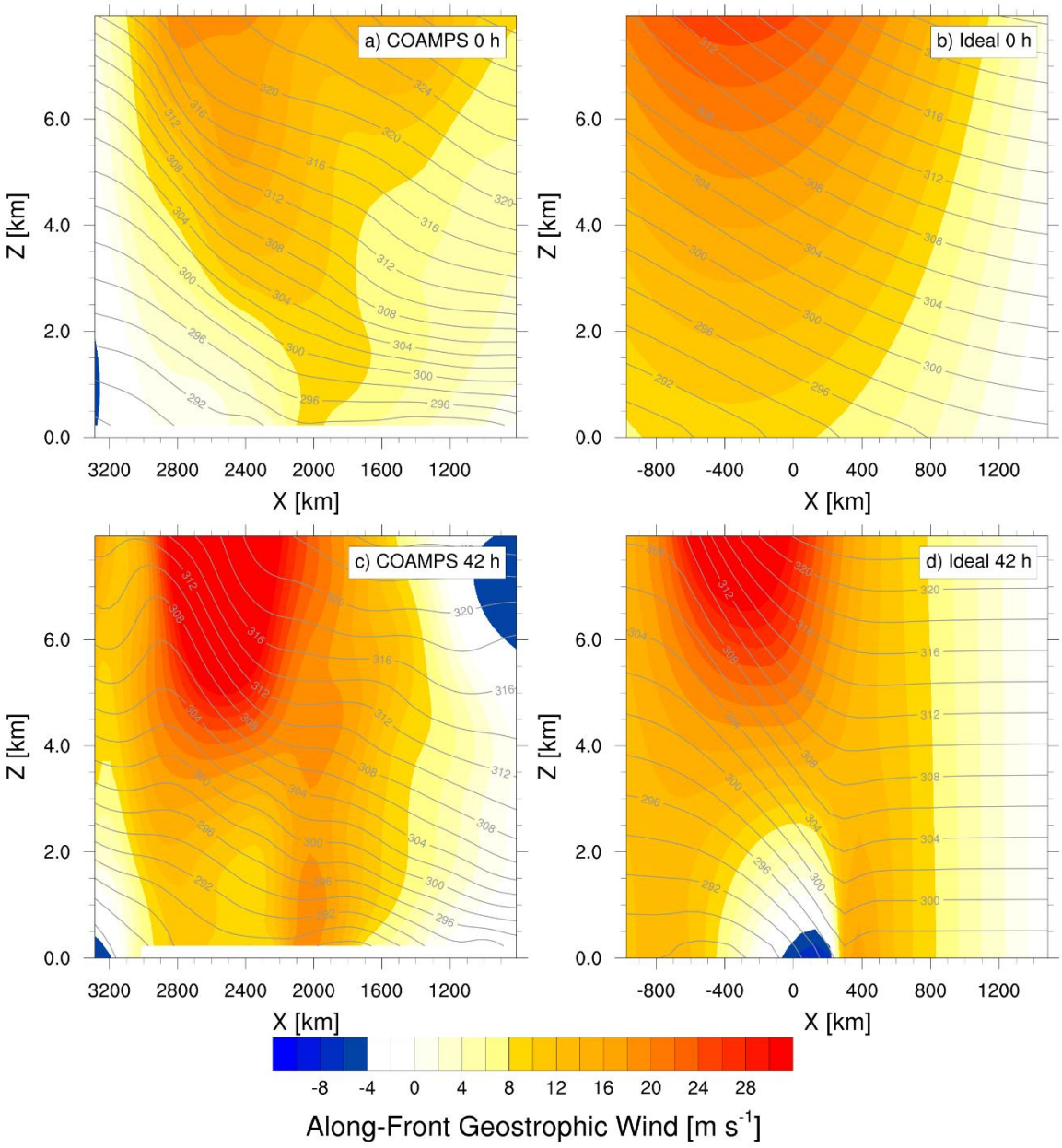

Figure 3.6: Cross sections of the along-front geostrophic wind (color fill; m s^{-1}) and potential temperature (grey contours; ci = 2 K) for a) 0-h COAMPS, b) 0-h idealized model, c) 42-h COAMPS, and d) 42-h idealized model. Fig. 3.6a corresponds to the transect in Fig. 3.5a, and Fig. 3.6c corresponds to the transect in Fig. 3.5b.

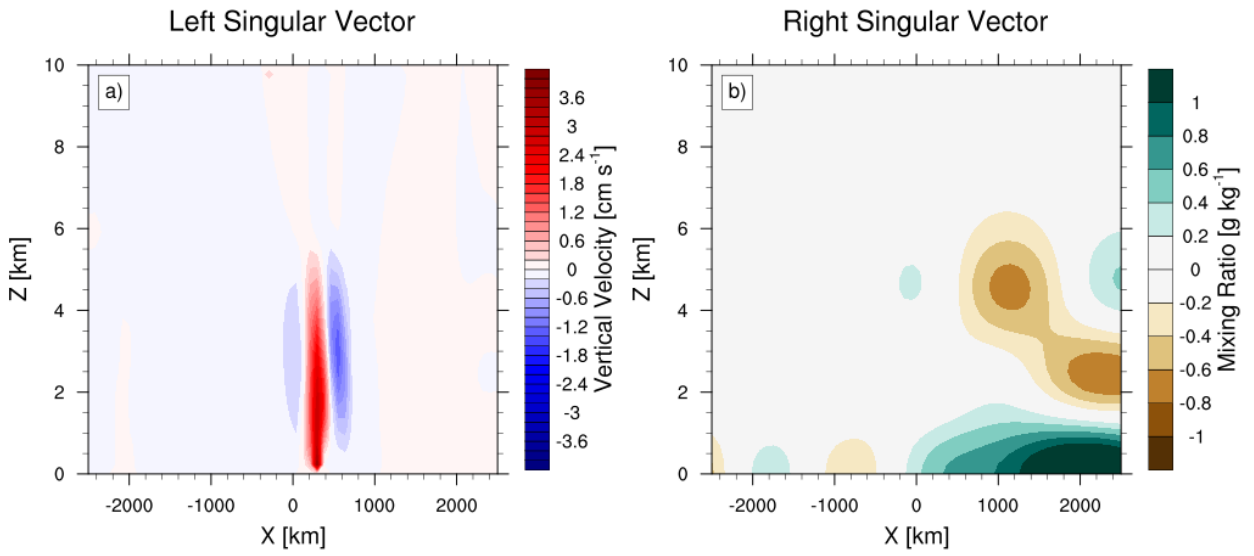

Figure 3.7: The left and right singular vectors scaled by 15x and dimensionalized for a) the left singular vector vertical velocity (color fill; cm s^{-1}), and b) the right singular vector mixing ratio (color fill; g kg^{-1}).

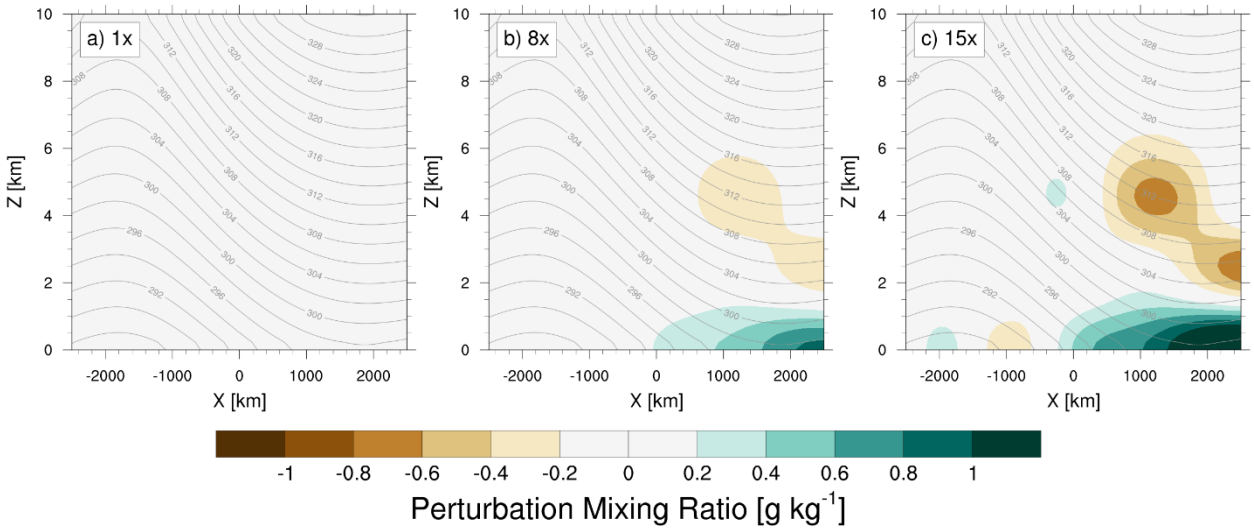

Figure 3.8: The initial-condition mixing-ratio perturbation scaled by a) 1x, b) 8x, and c) 15x. Each plot also has the potential temperature (grey contours; ci = 2 K) and is on the full-model domain.

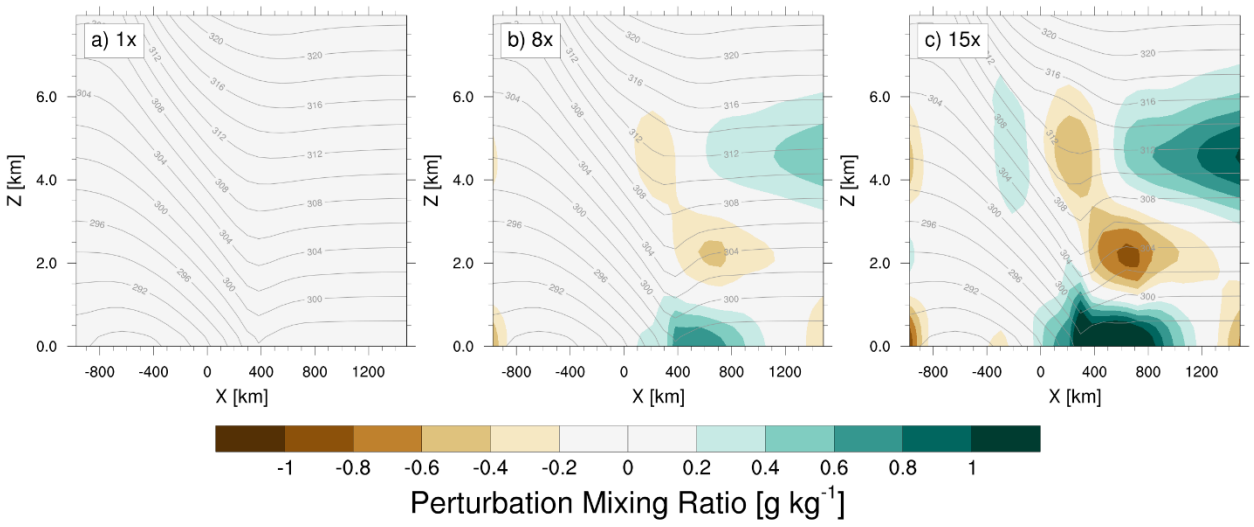

Figure 3.9: The evolved water vapor mixing ratio perturbations at 36 h for each ensemble member following the same scaling as in Fig. 3.7. The domain is zoomed in to focus on relevant features.

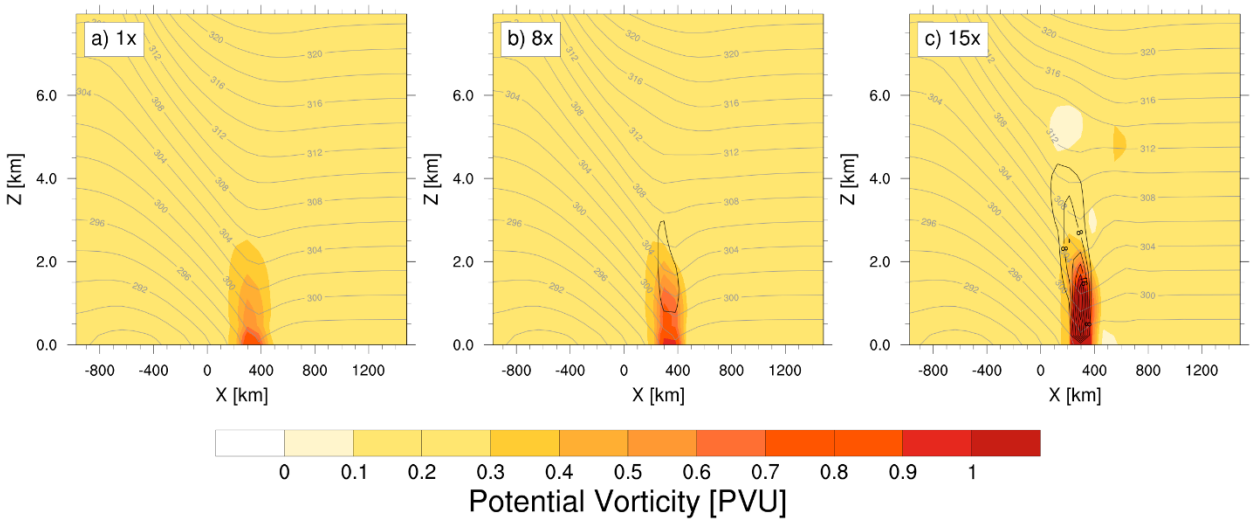

Figure 3.10: Same as Fig. 3.9 except for perturbation latent heating (black contour; ci = 4 K day^{-1}) and full-value potential vorticity (color fill; PVU).

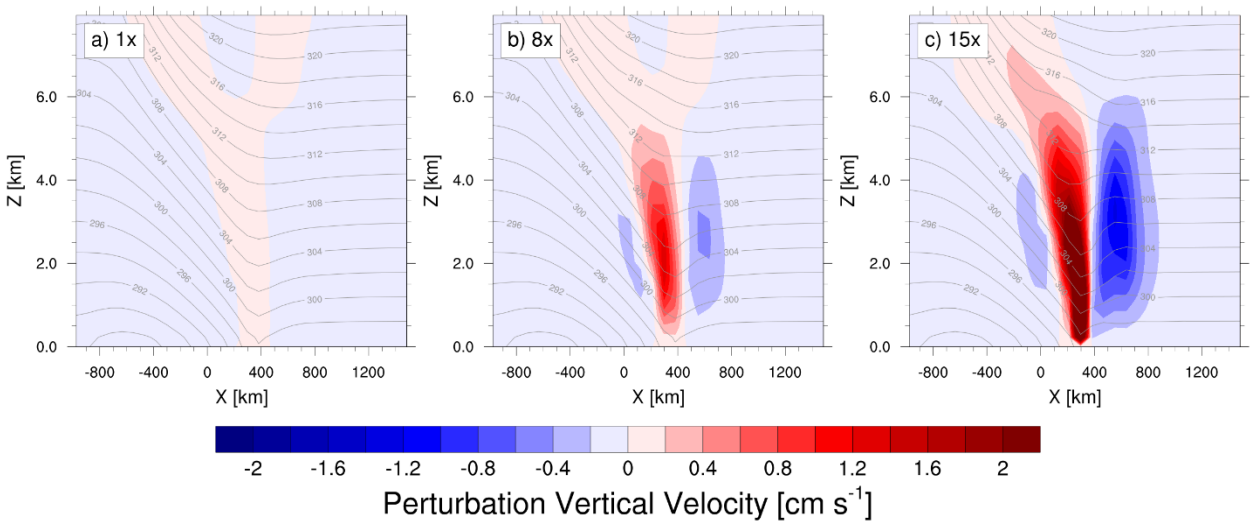

Figure 3.11: Same as Fig. 3.9 except for the perturbation vertical velocity (color fill; cm s^{-1}).

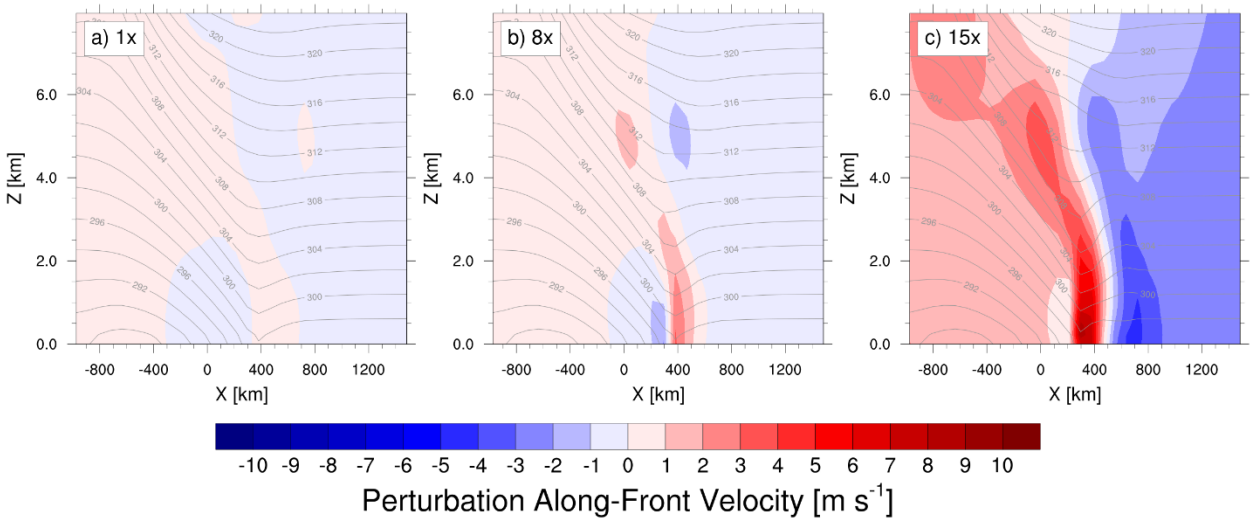

Figure 3.12: Same as Fig. 3.9 except for the perturbation along-front geostrophic wind (color fill; m s^{-1}).

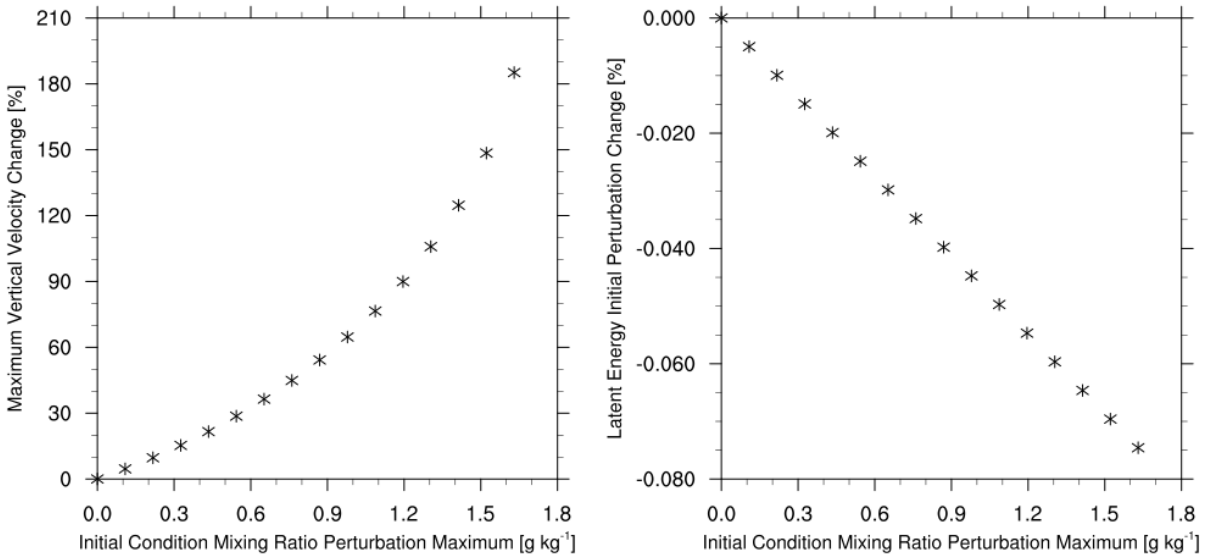

Figure 3.13: Scatter plots of each ensemble member at 36 h for a) the maximum vertical velocity percent change (%) relative to the moist control simulation versus the initial condition mixing ratio perturbation maximum (g kg^{-1}), and b) the domain-integrated latent-energy percent change (%) versus the initial-condition mixing-ratio-perturbation maximum (g kg^{-1}).

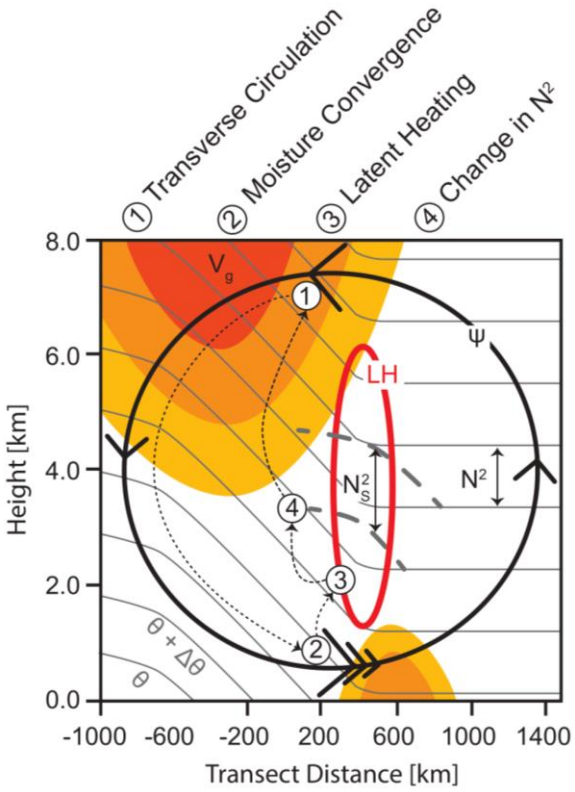

Figure 3.14: A schematic representation of the important physical processes discussed in the present study. The potential temperature (grey contours), latent heating (LH; thick red oval), along-front geostrophic wind (color fill with increasing value from orange to red), and the ageostrophic stream function (transverse circulation; large black circle). The direction of the transverse circulation is denoted by the black arrows with successively smaller arrows indicating regions of convergence. The dashed grey lines denote changes to the potential temperature due to latent-heating effects. The order of processes is labelled numerically with dotted black arrows connecting them for continuity. The Brunt-Vaisala frequency before and after the latent heating is measured by N^2 and N_s^2 respectively.

Supplemental Figures

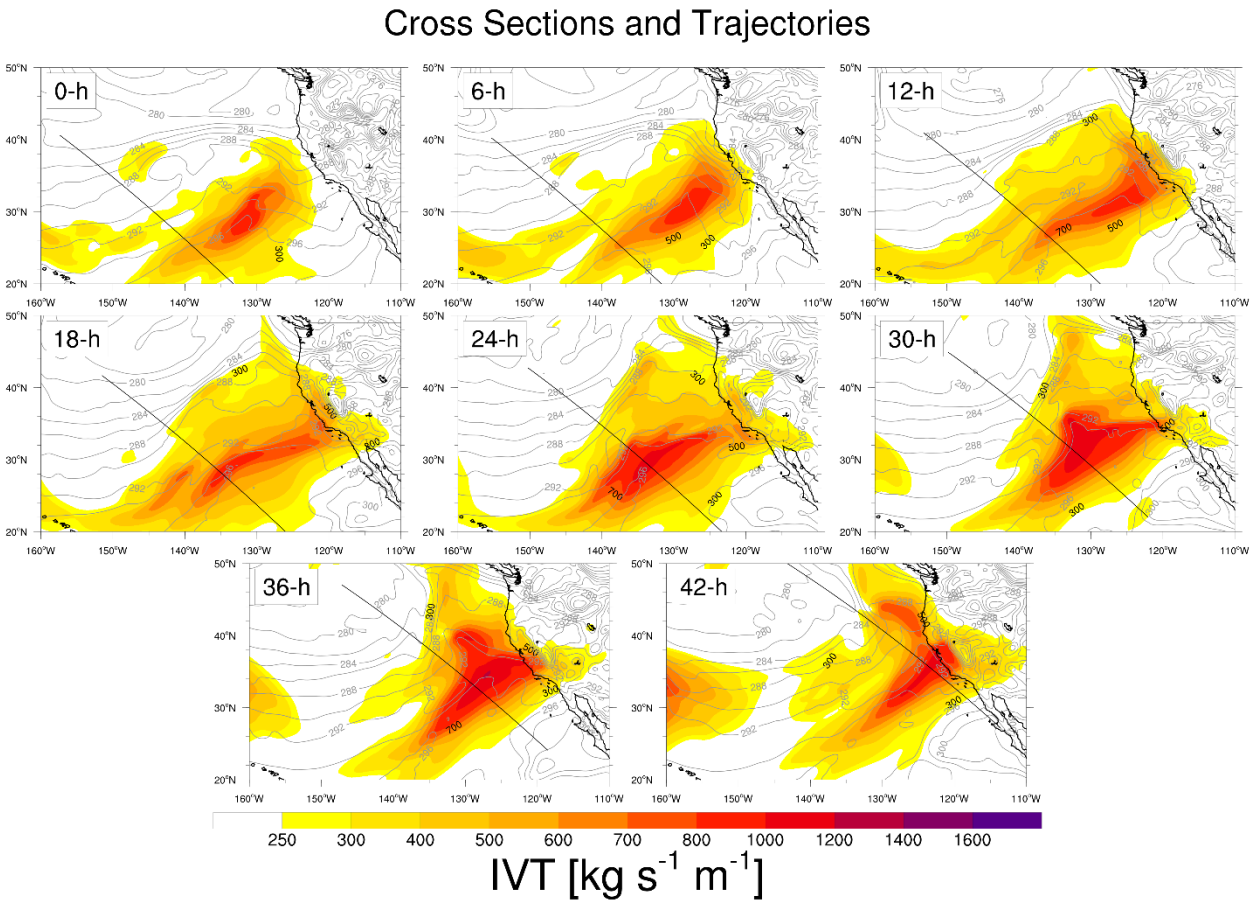

Supplemental 3.1: Same as Fig. 3.5 except plots are every 6 hours and the potential temperature (grey contours; ci = 2 K) is used instead of SLP.

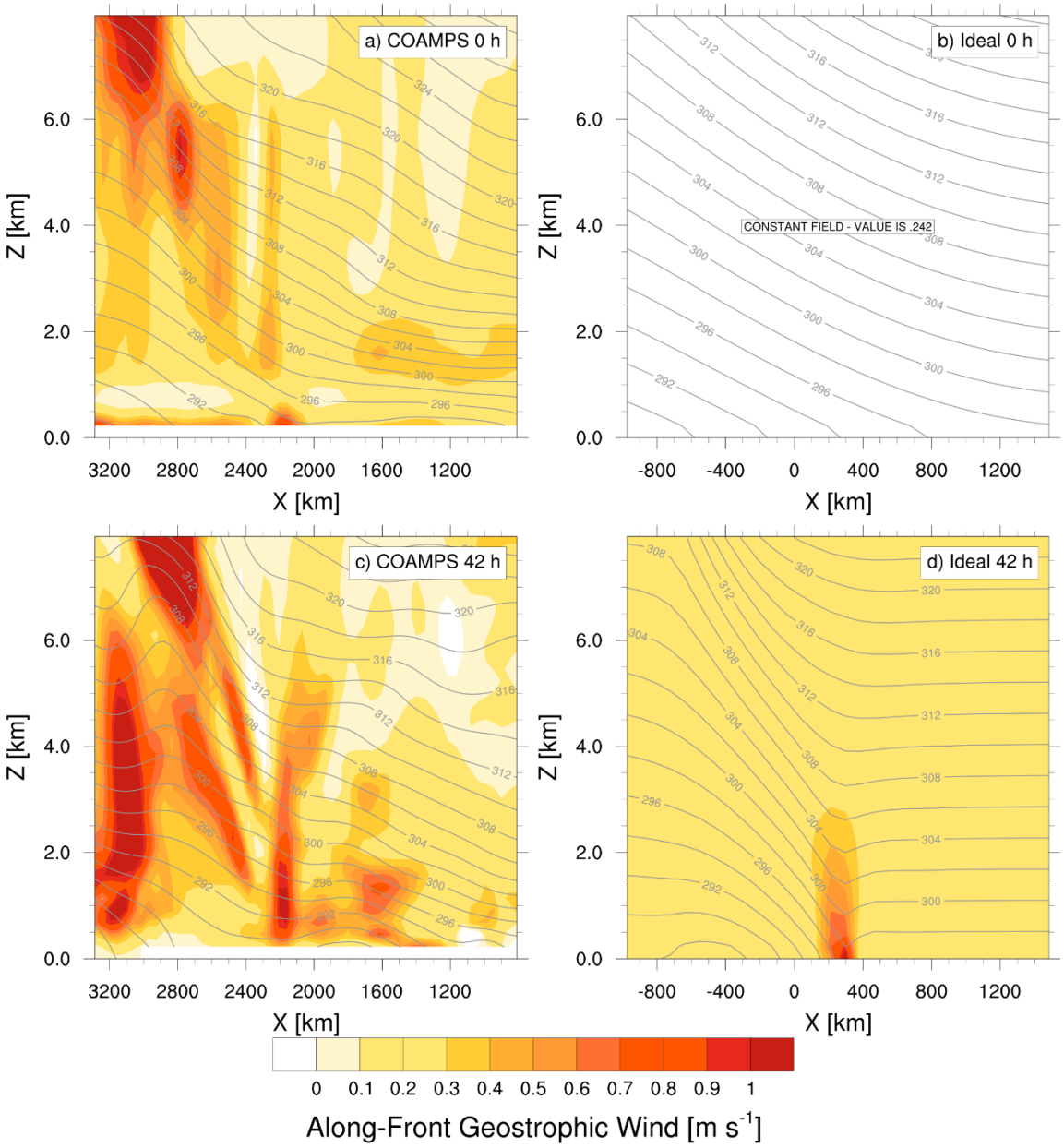

Supplemental 3.2: Same as Fig. 3.6 except for the potential vorticity (color fill; PVU)

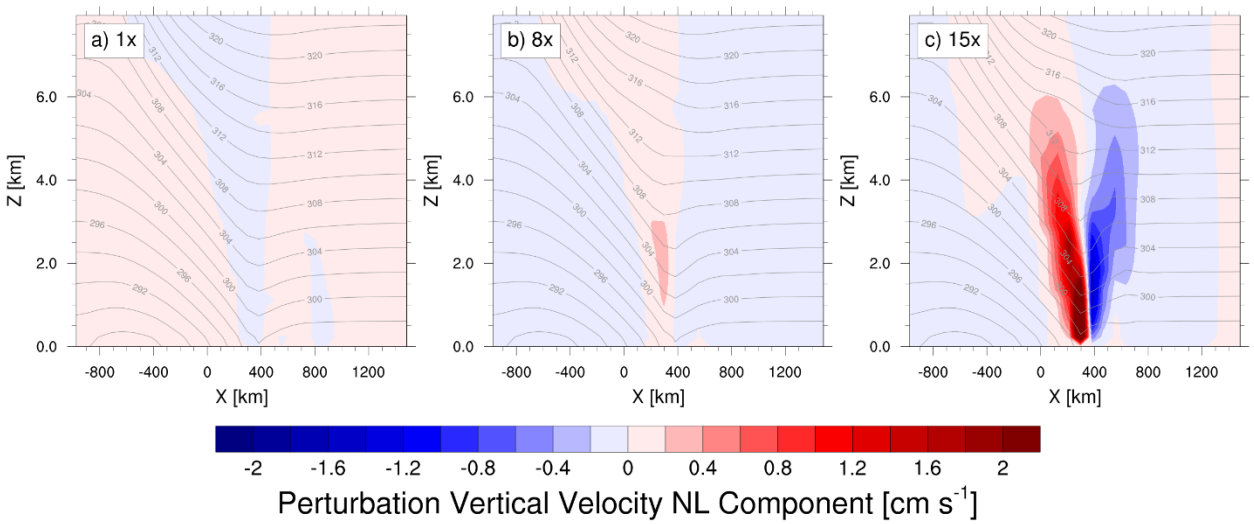

Supplemental 3.3: Same as Fig. 3.11 except for the nonlinear component of the perturbation vertical velocity. The nonlinear component is the residual of the total minus the linear component where the latter is calculated using a linear regression model.

References

Alpert, P., 1986: Mesoscale Indexing of the Distribution of Orographic Precipitation over High Mountains. *J. Climate Appl. Meteor.*, **25**, 532–545,https://doi.org/10.1175/1520-0450(1986)025<0532:MIOTDO>2.0.CO;2

Amerault, C., X. Zou, and J. D. Doyle, 2008: Tests of an adjoint mesoscale model with explicit moist physics on the cloud scale. *Mon. Wea. Rev*., **136**, 2120–2132.

American Meteorological Society, cited 2017: Atmospheric River. Glossary of Meteorology Available online at http://glossary.ametsoc.org/wiki/Atmospheric_River

Asselin, R., 1972: Frequency filter for time integrations. *Mon. Wea. Rev.*, **100,** 487–490.

Badger, J., and B. J. Hoskins, 2001: Simple initial value problems and mechanisms for baroclinic growth. J. Atmos. Sci., 58, 38–49.

Bjerknes, J., and H. Solberg, 1922: Life cycle of cyclones and the polar front theory of atmospheric circulation. Geofys. Publ.,3,1–18

Brill, K.F., L.W. Uccellini, R.P. Burkhart, T.T. Warner, and R.A. Anthes, 1985: Numerical Simulations of a Transverse Indirect Circulation and Low-Level Jet in the Exit Region of an Upper-Level Jet. J. Atmos. Sci., 42, 1306–1320, https://doi.org/10.1175/1520-0469(1985)042<1306:NSOATI>2.0.CO;2

Brill, K.F., 2014: Revisiting an Old Concept: The Gradient Wind. *Mon. Wea. Rev.*, **142**, 1460–1471, https://doi.org/10.1175/MWR-D-13-00088.1

Browning, K. a., and C. W. Pardoe, 1973: Structure of low-level jet streams ahead of mid-latitude cold fronts. *Q. J. R. Meteorol.* Soc., **99**, 619–638, doi:10.1256/smsqj.42203. http://onlinelibrary.wiley.com/doi/10.1002/qj.49709942204/abstract.

Cannon, F., C. Hecht, J. Cordeira, and F.M. Ralph, 2018: Synoptic to Mesoscale Forcing of Extreme Precipitation in Southern California. Journal of Geophysical Research – Atmospheres. DOI: 10.1029/2018JD029045

Cannon, F., J.M. Cordeira, C.W. Hecht, J.R. Norris, A. Michaelis, R. Demirdjian, and F.M. Ralph, 2020: GPM Satellite Radar Observations of Precipitation Mechanisms in Atmospheric Rivers. *Mon. Wea. Rev.*, **148**, 1449–1463, https://doi.org/10.1175/MWR-D-19-0278.1

Cordeira, J.M., F.M. Ralph, and B.J. Moore, 2013: The Development and Evolution of Two Atmospheric Rivers in Proximity to Western North Pacific Tropical Cyclones in October 2010. *Mon. Wea. Rev.*,**141**, 4234–4255, https://doi.org/10.1175/MWR-D-13-00019.1

Cordeira, J.M., F.M. Ralph, A. Martin, N. Gaggini, J.R. Spackman, P.J. Neiman, J.J. Rutz, and R. Pierce, 2017: Forecasting Atmospheric Rivers during CalWater 2015. *Bull. Amer. Meteor. Soc.*, **98**, 449–459, https://doi.org/10.1175/BAMS-D-15-00245.1

DeFlorio, M., D. Waliser, B. Guan, D. Lavers, F.M. Ralph, and F. Vitart, 2018: Global assessment of atmospheric river prediction skill. Journal of Hydrometeorology, 19, 409-426.

Demirdjian, R., J.D. Doyle, C.A. Reynolds, J.R. Norris, A.C. Michaelis, and F.M. Ralph, 2020a: A Case Study of the Physical Processes Associated with the Atmospheric River Initial-Condition Sensitivity from an Adjoint Model. *J. Atmos. Sci.*, **77**, 691–709, https://doi.org/10.1175/JAS-D-19-0155.1

Demirdjian, R., J.R. Norris, A. Martin, and F.M. Ralph, 2020b: Dropsonde Observations of the Ageostrophy within the Pre-Cold-Frontal Low-Level Jet Associated with Atmospheric Rivers. *Mon. Wea. Rev.*, **148**, 1389–1406, https://doi.org/10.1175/MWR-D-19-0248.1

Dettinger, M. D., F. M. Ralph, T. Das, P. J. Neiman, and D. R. Cayan, 2011: Atmospheric Rivers, Floods and the Water Resources of California. *Water*, **3**, 445–478, doi:10.3390/w3020445. http://dx.doi.org/10.3390/w3020445.

Dettinger, M. D., 2013: Atmospheric rivers as drought busters on the U.S. West Coast. *J. Hydrometeor.*, **14**, 1721–1732, doi: Dettinger, M. D., and D. Cayan, 2014: Drought and the California Delta—A matter of extremes. San Francisco Estuary Watershed Sci., 12(2).

Diaconescu, E. P., Laprise, R., 2012: Singular vectors in atmospheric sciences: A review. Earth-Science Reviews, 113, 161 – 175, doi:10.1016/j.earscirev.2012.05.005

Doyle, J.D., C.A. Reynolds, C. Amerault, 2011: Diagnosing tropical cyclone sensitivity. Computing in Science and Engineering, 13, 31-39.

Doyle, J.D., C.A. Reynolds, C. Amerault, J. Moskaitis, 2012: Adjoint sensitivity and predictability of tropical cyclogenesis. J. Atmos. Sci., 69, 3535-3557.

Doyle, J. D., C. Amerault, C. A. Reynolds, and P. A. Reinecke, 2014: Initial condition sensitivity and predictability of a severe extratropical cyclone using a moist adjoint. Mon. Wea. Rev., 142, 320–342. doi:https://doi.org/10.1175/MWR-D-13-00201.1.10.1175/ JHM-D-13-02.1.

Doyle, J.D., C.A. Reynolds, and C. Amerault, 0: Adjoint Sensitivity Analysis of High-Impact Extratropical Cyclones. *Mon. Wea. Rev.*, **0**, https://doi.org/10.1175/MWR-D-19-0055.1

Dudhia, J., 1993: A Nonhydrostatic Version of the Penn State–NCAR Mesoscale Model: Validation Tests and Simulation of an Atlantic Cyclone and Cold Front. *Mon. Wea. Rev.*, **121**, 1493–1513, https://doi.org/10.1175/1520-0493(1993)121<1493:ANVOTP>2.0.CO;2

Errico, R. M., 1997: What is an adjoint model? *Bull. Amer. Meteor. Soc*., **78**, 2577–2591.Fish, M.A., A.M. Wilson, and F.M. Ralph, 0: Atmospheric River Families: Definition and Associated Synoptic Conditions. *J. Hydrometeor.*, **0**, https://doi.org/10.1175/JHM-D-18-0217.1

European Centre for Medium-Range Weather Forecasts, 2017: ERA5 Reanalysis. Research Data Archive at the National Center for Atmospheric Research, Computational and Information Systems Laboratory, Boulder, CO. [Available online at https://doi.org/10.5065/D6X34W69.] Accessed 7 Sept 2019.

Hewson, T.D., 2009: Diminutive Frontal Waves—A Link between Fronts and Cyclones. *J. Atmos. Sci.*, **66**, 116–132, https://doi.org/10.1175/2008JAS2719.1

Hodur, R. M., 1997: The Naval Research Laboratory's Coupled Ocean/Atmospheric 738 Mesoscale Prediction System (COAMPS). *Mon. Wea. Rev*., **125**, 1414–1430.

Holton, J. R., 2004: An Introduction to Dynamic Meteorology. Elsevier Academic, 535 pp.

Hoskins, B.J. and F.P. Bretherton, 1972: Atmospheric Frontogenesis Models: Mathematical Formulation and Solution. *J. Atmos. Sci.*, **29**, 11–37, https://doi.org/10.1175/1520-0469(1972)029<0011:AFMMFA>2.0.CO;2

Hoskins, B.J., 1975: The Geostrophic Momentum Approximation and the Semi-Geostrophic Equations. *J. Atmos. Sci.*, **32**, 233–242, https://doi.org/10.1175/1520-0469(1975)032<0233:TGMAAT>2.0.CO;2

Hoskins, B.J. and N.V. West, 1979: Baroclinic Waves and Frontogenesis. Part II: Uniform Potential Vorticity Jet Flows-Cold and Warm Fronts. *J. Atmos. Sci.*, **36**, 1663–1680, https://doi.org/10.1175/1520-0469(1979)036<1663:BWAFPI>2.0.CO;2

Hoskins, B.J., 1982: The Mathematical Theory of Frontogenesis. *Ann. Rev. Fluid Mech.*, **14**, 131-151

Gray, W.M., C. Neumann, and T.L. Tsui, 1991: Assessment of the Role of Aircraft Reconnaissance on Tropical Cyclone Analysis and Forecasting. *Bull. Amer. Meteor.*

Soc.,**72**, 1867–1884, https://doi.org/10.1175/1520-0477(1991)072<1867:AOTROA>2.0.CO;2

Keyser, D. and M.A. Shapiro, 1986: A Review of the Structure and Dynamics of Upper-Level Frontal Zones. *Mon. Wea. Rev.*, **114**, 452–499, https://doi.org/10.1175/1520-0493(1986)114<0452:AROTSA>2.0.CO;2

Guan, B., and D. E. Waliser, 2015: Detection of atmospheric rivers: Evaluation and application of an algorithm for global studies. *J. Geophys. Res. Atmos.*, **120**, 12 514–12 535, doi:10.1002/2015JD024257.

Kingsmill, D.E., P.J. Neiman, B.J. Moore, M. Hughes, S.E. Yuter, and F.M. Ralph, 2013: Kinematic and Thermodynamic Structures of Sierra Barrier Jets and Overrunning Atmospheric Rivers during a Landfalling Winter Storm in Northern California. *Mon. Wea. Rev.*, **141**, 2015–2036, https://doi.org/10.1175/MWR-D-12-00277.1

Lackmann, G.M., 2002: Cold-Frontal Potential Vorticity Maxima, the Low-Level Jet, and Moisture Transport in Extratropical Cyclones. *Mon. Wea. Rev.*, **130**, 59–74, https://doi.org/10.1175/1520-0493(2002)130<0059:CFPVMT>2.0.CO;2

Lackmann, G., and J. Gyakum, 1999: Heavy Cold-Season Precipitation in the Northwestern United States :Synoptic Climatology and an Analysis of the Flood of 17 – 18 January 1986. *Weather Forecast.*, **14**, 687–700.

Lamjiri, M.A., M.D. Dettinger, F.M. Ralph, and B. Guan, 2017: Hourly Storm Characteristics along the U.S. West Coast: Role of Atmospheric Rivers in Extreme Precipitation. Geophysical Research Letters, 44, doi:10.1002/2017GL074193.

Lamjiri, M. A, Dettinger, M. D, Ralph, F. M, Oakley, N. S, & Rutz, J. J. (2018). Hourly Analyses of the Large Storms and Atmospheric Rivers that Provide Most of California's Precipitation in Only 10 to 100 Hours per Year. San Francisco Estuary and Watershed Science. 16(4).

Lavers, D. A., R. P. Allan, E. F. Wood, G. Villarini, D. J. Brayshaw, and A. J. Wade, 2011: Winter floods in Britain are connected to atmospheric rivers. *Geophys. Res. Lett.*, **38**, L23803, doi:10.1029/2011GL049783.

Lavers, D. A., M. J. Rodwell, D. S. Richardson, F. M. Ralph, J. D. Doyle, C. A. Reynolds, V. Tallapragada, and F. Pappenberger, 2018: The Gauging and Modeling of Rivers in the Sky. *Geophys. Res. Lett.*, **45**, 7828-7834, doi.org/10.1029/2018GL079019.

Lin, Y. 2011. GCIP/EOP Surface: Precipitation NCEP/EMC 4KM Gridded Data (GRIB) Stage IV Data. Version 1.0. UCAR/NCAR - Earth Observing Laboratory. https://doi.org/10.5065/D6PG1QDD. Accessed 12 Mar 2019.

Livezey, R.E. and W.Y. Chen, 1983: Statistical Field Significance and its Determination by Monte Carlo Techniques. *Mon. Wea. Rev.*, **111**, 46–59.

Lorenz, E.N. (1969) The predictability of a flow which possesses many scales of motion. Tellus, 21, 289–307. https://doi.org/10.1111/j.2153-3490.1969.tb00444.x

Lu, P., N. Lin, K. Emanuel, D. Chavas, and J. Smith, 2018: Assessing Hurricane Rainfall Mechanisms Using a Physics-Based Model: Hurricanes Isabel (2003) and Irene (2011). *J. Atmos. Sci.*, **75**, 2337–2358, https://doi.org/10.1175/JAS-D-17-0264.1

Mahoney, K., and G. Lackmann, 2007: The Effect of Upstream Convection on Downstream Precipitation. *Weather Forecast.*, **22**, 255–277, doi:10.1175/WAF986.1.

Majumdar, S., 2016: A review of Targeted Observations. *Bull. Amer. Met. Soc.*, **97**, 2287-2303. doi.org/10.1175/BAMS-D-14-00259.1

Martin, A., F.M. Ralph, R. Demirdjian, L. DeHaan, R. Weihs, J. Helly, D. Reynolds, and S. Iacobellis, 2018: Evaluation of Atmospheric River Predictions by the WRF Model Using Aircraft and Regional Mesonet Observations of Orographic Precipitation and Its Forcing. *J. Hydrometeor.*, **19**, 1097–1113, https://doi.org/10.1175/JHM-D-17-0098.1

Martin, A.C., F.M. Ralph, A. Wilson, L. DeHaan, and B. Kawzenuk, 2019: Rapid Cyclogenesis from a Mesoscale Frontal Wave on an Atmospheric River: Impacts on Forecast Skill and Predictability during Atmospheric River Landfall. *J. Hydrometeor.*, **20**, 1779–1794, https://doi.org/10.1175/JHM-D-18-0239.1

Martin, J.D. and W.M. Gray, 1993: Tropical Cyclone Observation and Forecasting with and without Aircraft Reconnaissance. *Wea. Forecasting*, **8**, 519–532,https://doi.org/10.1175/1520-0434(1993)008<0519:TCOAFW>2.0.CO;2

Moore, A.M. and Kleeman, R. (1997), The singular vectors of a coupled ocean-atmosphere model of Enso. I: Thermodynamics, energetics and error growth. *Q.J.R. Meteorol. Soc.*, **123**: 953-981. doi:10.1002/qj.49712354009

Moore, B. J., P. J. Neiman, F. M. Ralph, and F. Barthold, 2012: Physical processes associated with heavy flooding rainfall in Nashville, Tennessee and vicinity during 1–2 May 2012: The role of an atmospheric river and mesoscale convective systems. *Mon. Wea. Rev.*, **140**, 358–378, doi:10.1175/ MWR-D-11-00126.1.

Neiman, P., F. M. Ralph, A. White, D. Kingsmill, and P. Persson, 2002: The Statistical Relationship between Upslope Flow and Rainfall in California' s Coastal Mountains : Observations during CALJET. *Mon. Weather Rev.*, **130**, 1468–1492.

Neiman, P. J., D. J. Gottas, A. B. White, S. I. Gutman, and F. M. Ralph, 2009: A water vapour flux tool for precipitation forecasting. Proc. ICE - *Water Manag.*, **162**, 83–94, doi:10.1680/wama.2009.162.2.83. http://www.icevirtuallibrary.com/content/article/10.1680/wama.2009.162.2.83.

Neiman, P. J., F. M. Ralph, G. A. Wick, J. Lundquist, and M. D. Dettinger, 2008: Meteorological characteristics and overland precipitation impacts of atmospheric rivers affecting the West Coast of North America based on eight years of SSM/I satellite observations. *J. Hydrometeor.*, **9**, 22– 47, doi:10.1175/ 2007JHM855.1.

Neiman, P.J., G.A. Wick, B.J. Moore, F.M. Ralph, J.R. Spackman, and B. Ward, 2014: An Airborne Study of an Atmospheric River over the Subtropical Pacific during WISPAR: Dropsonde Budget-Box Diagnostics and Precipitation Impacts in Hawaii. *Mon. Wea. Rev.*, **142**, 3199–3223, https://doi.org/10.1175/MWR-D-13-00383.1

Orlanski, I., and B. Ross, 1977: The Circulation Associated with a Cold Front. Part 1: Dry Case. *J. Atmos. Sci.*, **34**, 1619–1633.

Orr, W. McF., 1907: The stability or instability of the steady motions of a perfect liquid and of a viscous liquid. Part I: A perfect liquid. Proc. Roy. Irish Acad., 27, 9–68.

Parker, D. J., 1998: Secondary frontal waves in the North Atlantic region: A dynamical perspective of current ideas. Quart. J. Roy. Meteor. Soc.,124,829–856

Peng, M.S. and C.A. Reynolds, 2006: Sensitivity of Tropical Cyclone Forecasts as Revealed by Singular Vectors. *J. Atmos. Sci.*, **63**, 2508–2528, https://doi.org/10.1175/JAS3777.1

Ralph, F.M., P.J. Neiman, and G.A. Wick, 2004: Satellite and CALJET Aircraft Observations of Atmospheric Rivers over the Eastern North Pacific Ocean during the Winter of 1997/98. *Mon. Wea. Rev.*, **132**, 1721–1745,

Ralph, F. M., P. J. Neiman, and R. Rotunno, 2005: Dropsonde Observations in Low-Level Jets over the Northeastern Pacific Ocean from CALJET-1998 and PACJET-2001 : Mean Vertical-Profile and Atmospheric-River Characteristics. *Mon. Weather Rev.*, **133**, 889–910.

Ralph, F. M., P. J. Neiman, G. A. Wick, S. I. Gutman, M. D. Dettinger, D. R. Cayan, and A. B. White, 2006: Flooding on California's Russian River : Role of atmospheric rivers. *Geophys. Res. Lett.*, **33**, 2–6, doi:10.1029/2006GL026689.

Ralph, F.M., and Coauthors, 2016: CalWater Field Studies Designed to Quantify the Roles of Atmospheric Rivers and Aerosols in Modulating U.S. West Coast Precipitation in a Changing Climate. *Bull. Amer. Meteor. Soc.*, **97**, 1209–1228, https://doi.org/10.1175/BAMS-D-14-00043.1

Ralph, F.M., T. Coleman, P.J. Neiman, R.J. Zamora, and M.D. Dettinger, 2013: Observed Impacts of Duration and Seasonality of Atmospheric-River Landfalls on Soil Moisture and Runoff in Coastal Northern California. *J. Hydrometeor.*, **14**, 443–459, https://doi.org/10.1175/JHM-D-12-076.1

Ralph, F.M., S.F. Iacobellis, P.J. Neiman, J.M. Cordeira, J.R. Spackman, D.E. Waliser, G.A. Wick, A.B. White, and C. Fairall, 2017: Dropsonde Observations of Total Integrated Water Vapor Transport within North Pacific Atmospheric Rivers. *J. Hydrometeor.*, **18**, 2577–2596, https://doi.org/10.1175/JHM-D-17-0036.1

Ralph, F. M. 2017: FIRO Steering Committee Co-Chairs Provide In-depth Briefing to USACE, http://cw3e.ucsd.edu/firo-steering-committee-co-chairs-provide-in-depth-briefing-to-usace/Ralph, F. M. 2018: Atmospheric River Reconnaissance – 2018 is Underway, http://cw3e.ucsd.edu/atmospheric-river-reconnaissance-2018-underway/ .

Ralph, F.M., J.J. Rutz, J.M. Cordeira, M. Dettinger, M. Anderson, D. Reynolds, L.J. Schick, and C. Smallcomb, 2019: A Scale to Characterize the Strength and Impacts of Atmospheric Rivers. Bull. Amer. Meteor. Soc., 0 DOI: https://doi.org/10.1175/BAMS-D-18-0023.1

Ralph, F. M., and Coauthors, 2020: West Coast Forecast Challenges and Development of Atmospheric River Reconnaissance. *Bull. Amer. Meteor. Soc.*, (*In Review).*

Renfrew, I. A., A. J. Thorpe, and C. H. Bishop, 1997: The role of the environmental flow in the development of secondary frontal cyclones. Quart. J. Roy. Meteor. Soc.,123,1653–1675.

Reynolds, C.A., J.D. Doyle, F.M. Ralph, and R. Demirdjian, 2019: Adjoint Sensitivity of North Pacific Atmospheric River Forecasts. *Mon. Wea. Rev.*, DOI: https://doi.org/10.1175/MWR-D-18-0347.1

Reynolds, C. A., J. D. Doyle, X. Hong, 2016: Examining tropical cyclone – Kelvin wave interactions using adjoint diagnostics. Mon. Wea. Rev., 144, 4421-4439.

Reynolds, C.A., R. Gelaro, and J.D. Doyle, 2001: Relationship between singular vectors and transient features in the background flow. Quart. J. Roy. Meteor. Soc., 127, 1731-1760.

Rivals, H., J.-P. Cammas, and I. A. Renfrew, 1998: Secondary cyclogenesis: The initiation phase of a frontal wave observed over the eastern Atlantic. Quart. J. Roy. Meteor. Soc.,124,243–267.

Robert, A. J., 1966: The integration of a low order spectral form of the primitive meteorological equations. *J. Meteor. Soc. Japan*, **44,** 237–245.

Rutz, J. J., W. J. Steenburgh, and F. M. Ralph, 2014: Climatological characteristics of atmospheric rivers and their inland penetration over the Western United States. *Mon. Wea. Rev.*, **142**, 905–921, doi:10.1175/MWR-D-13-00168.1.

Schemm, S., H. Wernli, and L. Papritz, 2013: Warm Conveyor Belts in Idealized Moist Baroclinic Wave Simulations. J. Atmos. Sci., 70, 627–652, https://doi.org/10.1175/JAS-D-12-0147.1

Shoemaker, D.N., W.M. Gray, and J.D. Sheaffer, 1990: Influence of Synoptic Track Aircraft Reconnaissance on JTWC Tropical Cyclone Track Forecast Errors. *Wea. Forecasting*, **5**, 503–507, https://doi.org/10.1175/1520-0434(1990)005<0503:IOSTAR>2.0.CO;2

Snyder, C., W.C. Skamarock, and R. Rotunno, 1991: A Comparison of Primitive-Equation and Semigeostrophic Simulations of Baroclinic Waves. *J. Atmos. Sci.*, **48**, 2179–2194, https://doi.org/10.1175/1520-0469(1991)048<2179:ACOPEA>2.0.CO;2

Stone, R.E., C.A. Reynolds, J.D. Doyle, R.H. Langland, N.L. Baker, D.A. Lavers, and F.M. Ralph, 2020: Atmospheric River Reconnaissance Observation Impact in the Navy Global Forecast System. *Mon. Wea. Rev.*, **148**, 763–782, https://doi.org/10.1175/MWR-D-19-0101.1

Thorpe, A.J. and K.A. Emanuel, 1985: Frontogenesis in the Presence of Small Stability to Slantwise Convection. *J. Atmos. Sci.*, **42**, 1809–1824, https://doi.org/10.1175/1520-0469(1985)042<1809:FITPOS>2.0.CO;2

Thorpe, A., and S. Clough, 1991: Mesoscale dynamics of cold fronts : Structures described by dropsoundings in FRONTS. *Q. J. R. Meteorol. Soc.*, **1**, 903–941.

Valenzuela, R.A. and D.E. Kingsmill, 2015: Orographic Precipitation Forcing along the Coast of Northern California during a Landfalling Winter Storm. *Mon. Wea. Rev.*, **143**, 3570–3590, https://doi.org/10.1175/MWR-D-14-00365.1

Wakimoto, R., and H. Murphey, 2008: Airborne Doppler Radar and Sounding Analysis of an Oceanic Cold Front. *Mon. Weather Rev.*, **136**, 1475–1491,doi:10.1175/2007MWR2241.1.

Wernli, H., and H. C. Davies, 1997: A Lagrangian-based analysis of extratropical cyclones. I: The method and some applications. Quart. J. Roy. Meteor. Soc., 123, 467–489.

Wernli, H., 1997: A Lagrangian-based analysis of extratropical cyclones. II: A detailed case study. Quart. J. Roy. Meteor. Soc., 123, 1677–1706.

Winters, A.C. and J.E. Martin, 2014: The Role of a Polar/Subtropical Jet Superposition in the May 2010 Nashville Flood. *Wea. Forecasting*, **29**, 954–974, https://doi.org/10.1175/WAF-D-13-00124.1

Zhang, Z., Ralph, F. Martin, & Zheng, M., 2018: The Relationship between Extratropical Cyclone Strength and Atmospheric River Intensity and Position. Geophysical Research Letters, 45. https://doi.org/10.1029/2018GL079071

Zheng, M., Chang, E.K. and Colle, B.A., 2013. Ensemble sensitivity tools for assessing extratropical cyclone intensity and track predictability. *Weather and Forecasting*, *28*(5), pp.1133-1156. https://doi.org/10.1175/WAF-D-12-00132.1

Zheng, M., and Coauthors, 2020: Data Gaps within Atmospheric Rivers over the Northeastern Pacific. *Bull. Amer. Meteor. Soc.*, *(In Review)*